The modulation of galactic cosmic rays over a solar cycle

ST Mohlolo

21271518

Dissertation submitted in partial fulfilment of the requirements for the degree *Magister Scientiae* in Space Physics at the Potchefstroom Campus of the North-West University

Supervisor:	Prof SES Ferreira
Co-supervisor:	Dr R Manuel
Co-supervisor:	Prof MS Potgieter

November 2016

"Physics is, hopefully, simple. Physicists are not."

Edward Teller

Abstract

This work studied the modulation of galactic cosmic rays in the heliosphere by using a well-established, time dependent numerical modulation model to calculate cosmic ray transport inside the heliosphere over a solar cycle. Results were compared to observations from the Voyager 1 and 2 spacecraft. It was shown that, when using the modified compound approach of Manuel et al. [2014] to scale the transport coefficients over a solar cycle, the model resulted in compatibility with spacecraft observations on a global scale. However, for certain periods, e.g. 1985 - 1990 and 1992 - 2001, the model did not agree with observations. For instance, for the period 1985 - 1990, the Voyager 1 spacecraft observed a plateau-like intensity profile while the model computed a peak-like intensity profile along the Voyager 1 trajectory. Voyager 2 on the other hand measured a peak-like intensity profile as expected from a traditional drift description of cosmic ray intensities around solar minimum. It was shown that, for this period, the Voyager 1 spacecraft was above the heliospheric current sheet region while Voyager 2 was inside the heliospheric current sheet region close to the equatorial region. It was shown that the time-dependent function that scales drifts up or down depending on the level of solar activity over a solar cycle, resulted in the peak-like intensity profile compatible with Voyager 2 observations but not Voyager 1 observations. It was proposed that this time-dependent function has a latitude dependence with different values inside and outside of the heliospheric current sheet, i.e. a different dependence above compared to in the heliospheric current sheet region. This improved compatibility between the model and Voyager 1 observations. However, the full implementation of such an additional spatial dependence in the 2D model is beyond the scope of this study. For the period 1992 - 2001, it was shown that the tilt angle increases much faster towards solar maximum than the corresponding decrease in observed cosmic ray intensities. This resulted in the model computing intensities decreasing faster than the observed intensities as a function of increasing solar activity and therefore causing incompatibility between the model and the observations. It was shown for this period that modifying the tilt angle by using an averaged tilt angle resulted in improved compatibility with observations.

Keywords: Heliosphere, cosmic rays, solar cycle, modulation, solar activity, particle drifts

Opsomming

Hierdie werk bestudeer die modulasie van galaktiese kosmiese strale in die heliosfeer deur gebruik te maak van 'n numeriese tydsafhanklike modulasie model om die transport van kosmiese strale binne die heliosfeer en oor 'n sonsiklus te bereken. Resultate word vergelyk met Voyager 1 en 2 ruimtetuig waarnemings. Daar word gewys dat wanneer die gewysigde saamgestelde benadering van Manuel et al. [2014] gebruik word om die transport koëffisiënte te skaal oor 'n sonsiklus, dit lei tot vergelykbaarheid tussen die model en waarnemings op 'n globale skaal. Vir sekere tydperke, egter soos 1985 - 1990 en 1992 - 2001, stem die model nie saam met die waarnemings nie. Vir die tydperk 1985 - 1990, het die Voyager 1 ruimtetuig 'n platerige intensiteits profiel gemeet terwyl die model langs Voyager 1 se trajek 'n meer puntagtige intensiteits profiel bereken het. Aan die ander kant meet Voyager 2 wel 'n puntagtige intensiteits profiel soos wat verwag word van 'n tradisionele dryf beskrywing van intensiteite rondom 'n son-minimum. Die Voyager 1 ruimtetuig was vir hierdie tydperk van belang bo die heliosferiese neutrale vlak gebied, terwyl Voyager 2 in die heliosferiese neutrale vlak gebied was. Daar word verder aangetoon dat die tydsafhanklike funksie, wat die dryf koëffisiënt oor 'n sonsiklus skaal, lei tot die puntagtige intensiteits profiel wat met Voyager 2 waarnemings vergelyk maar nie met Voyager 1 s'n nie. Daar word voorgestel dat die tydsafhanklike funksie 'n breëtegraadse afhanklikheid $h\hat{e}$, bv. verkillende afhanklikhede bo en in die heliosferiese neutrale vlak gebied. Hierdie lei tot beter vergelykbaarheid tussen die model en Voyager 1 waarnemings. Die volle implementering egter van so 'n ruimtelike afhanklike dryf koëffisiënt in 'n ruimtelike 2D model is egter buite die doel van hierdie studie. Daar word ook aangetoon dat die kantelhoek vergroot vinniger as funksie van tyd as die waargeneemde kosmiese straal intensiteite vir die tydperk 1992 - 2001. Die gevolg is dat die model intensiteite bereken wat vinniger as die waarnemings afneem as 'n funksie van toenemende sonaktiwiteit. Daar word vir hierdie tydperk dan gewys deur gebruik te maak van die gemiddelde kantelhoek, dat die kan lei tot beter vergelykbaarheid met waarnemings.

Keywords: Heliosfeer, kosmiese strale, sonsiklus, modulasie, sonaktiwiteit, deeltjie dryf

Acknowledgements

It is my pleasure to express gratitude to the following persons and institutions for their support:

- Prof. S.E.S. Ferreira, my supervisor, for his guidance, patience and great leadership role he played throughout this study.
- Dr. R. Manuel and Prof. M.S. Potgieter, as co-supervisors, for their helpful discussions, insights and technical advices on many occasions.
- Mrs. M.P. Sieberhagen, Mrs. E. van Rooyen, and Mrs. L. van Wyk for handling of all my administrative issues.
- Mr. M. Holleran and Mr. C. Ackerman for their assistance with computer-related problems and unfailing technical support.
- Mrs. C. Vorster, for her help with the language editing of this document.
- The National Research Foundation, the South African National Space Agency and the Center for Space Research at the North-West University, for financial support throughout my studies.

A special thanks goes to:

- My friends and family in the Lord, PSCF.
- My parents (Ben and Lizzy) and brother (Daniel), for their love, support, sacrifices and prayers throughout.
- Ms. G. Olifant, for her perpetual love, encouragement, unmeasurable patience and understanding throughout this long journey.
- Above all, I would like to thank my God, my Maker and personal Saviour, for an opportunity granted to study and appreciate but a small portion of the volume of space He created.

Timothy Selwana Mohlolo
Center for Space Research
North-West University
November 2016

Soli Deo Gloria!!!

Contents

Acronyms and Abbreviations

1D	One-Dimensional
2D	Two-Dimensional
3D	Three-Dimensional
AU	Astronomical Unit (1 AU = 1.49×10^{11} m)
CIR	Corotating Interaction Region
CME	Coronal Mass Ejection
CMIR	Corotating Merged Interaction Region
CR	Carrington Rotation
FLS	Fast Latitude Scan
GMIR	Global Merged Interaction Region
HCS	Heliospheric Current Sheet
HMF	Heliospheric Magnetic Field
HPS	Heliopause Spectrum
IMP	Interplanetary Monitoring Platform
LIS	Local Interstellar Spectrum
LISM	Local Interstellar Medium
LMIR	Local Merged Interaction Region
MIR	Merged Interaction Region
QLT	Quasilinear Theory
TPE	Transport Equation
WCS	Wavy Current Sheet

Dedicated to my parents (Ben and Lizzy Mohlolo) - For all their love, support and sacrifices.

Chapter 1

Introduction

This work focused on the solar modulation of galactic cosmic rays in the heliosphere, which is the region of space influenced by the Sun. In particular, the modelling of the transport of these energetic particles in the heliosphere was concentrated on. Inside the heliosphere (modulation volume), the modulation of cosmic rays is described by the Parker [1965] transport equation (see Chapter 3), which contains all the relevant physical processes. Over the years, numerical modulation models of different complexities have been used as tools for studying cosmic ray modulation in the heliosphere [e.g. Kóta and Jokipii, 1983, Potgieter and Moraal, 1985, Burger and Hattingh, 1995, Ferreira and Potgieter, 2004, Burger et al., 2008, Strauss et al., 2012, Engelbrecht and Burger, 2013, Potgieter, 2013*b*, Manuel et al., 2014, Dunzlaff et al., 2015, Vos, 2016]. All these models are dependent on a sound transport theory, appropriate boundary conditions like the local interstellar spectra and a solid numerical scheme taking into account the necessary heliospheric structure and solar cycle related changes within.

In this work, the transport equation was solved numerically using a well-established, 2D time dependent numerical modulation model originally developed by Potgieter and le Roux [1992] and applied by Potgieter and Haasbroek [1993]. This numerical model was further improved by Ferreira [2002] and Ferreira and Potgieter [2004] by constructing and incorporating a time-dependence in the transport coefficients to describe changes in the cosmic ray transport coefficients over a solar cycle and was named the compound approach (see Chapter 4). This approach was afterwards applied and refined by Ndiitwani et al. [2005] to study charge-sign dependent modulation of cosmic rays in the heliosphere, Magidimisha [2011] to study cosmic ray proton and electron modulation in the heliosphere along the Ulysses trajectory and Manuel [2012] to calculate cosmic ray intensities in the heliosphere along both Voyager 1 and 2 trajectories and also at Earth.

Recently the compound approach has been improved by Manuel [2012] and Manuel et al. [2014] by incorporating in the model theoretical advances on the transport coefficients based on the work of Teufel and Schlickeiser [2002], Teufel and Schlickeiser [2003], Shalchi et al.

[2004], and Minnie et al. [2007]. The difference between the traditional compound approach and the recently modified compound approach is that the traditional compound approach is based on an empirical approach because it was then not well-known how the diffusion and drift coefficients change over a solar cycle.

It is shown in Chapter 4, that, even though the modified compound approach of Manuel [2012] and Manuel et al. [2014] is compatible with spacecraft observations on a global scale, for certain periods the model does not agree with observations. E.g. for the period 1985 - 1990, the modified compound approach resulted in a computed peak-like intensity profile around the solar minimum of $\sim$ 1987, while Voyager 1 observations showed a plateau-like intensity profile for this period. This is not consistent with modelling results or with Voyager 2 observations which also showed a peak-like intensity profile. This period of interest is investigated in Chapters 5 and 6, to determine if any of the parameters used as input in the model and/or some of the heliospheric interfaces are responsible for the incompatibility between the model and Voyager 1 spacecraft observations.

Chapter 5 looks at different modulation parameters that are used in the model as input to establish if they could lead to different modulation conditions between Voyager 1 and 2. Examples of these parameters include the solar wind plasma speed, heliospheric current sheet tilt angle and the heliospheric magnetic field strength. It is shown that even though some small scale differences between these different parameters in different hemispheres exist, these differences were not enough to account for the asymmetry between Voyager 1 and 2 measurements for the period 1985 - 1992.

In Chapter 6 it is shown that the time-dependence in the drift coefficient as implemented in the modified compound approach of Manuel et al. [2014], resulted in incompatibility between Voyager 1 observations and the model for the period 1985 - 1990. As a result, a modification to this time-dependence is proposed. This is done by comparing the effects on computed intensities of the different time-dependent functions that scale the transport coefficients over a solar cycle. This is done for both the traditional compound approach and the modified compound approach. It is also shown for this period (1985 - 1990) that Voyager 1 was at higher latitudes than Voyager 2 and more importantly above the HCS region for this period, while Voyager 2 was in the equatorial region and inside the HCS region. Because of the different latitude positions of Voyager 1 and 2, a modification to the time-dependence of the drift coefficient is proposed. Inside the HCS region and above the region swept by the HCS, the drift coefficient is scaled differently over a solar cycle. This however, will lead to additional terms for the drift coefficient at the interface between these two regions. The full implementation of such an additional spatial dependence to assure that the drift velocities remain divergence free is beyond the scope of this study. However, it is shown to first-order that this modification results in improved compatibility with Voyager 1 observations when compared to the modified compound approach.

The model is also applied in Chapter 7 to another period where there is incompatibility between the modified compound approach and Voyager observations. This period is 1992 - 2001. The chapter first shows that from $\sim$ 1992 - 1998, Voyager 1 was above the HCS region in the northern hemisphere, while Voyager 2 was below the HCS region from $\sim$ 1995 - 1997 in the southern hemisphere. The model from $\sim$ 1998 calculates intensities decreasing faster than observations for increasing solar activity. This is similar to what Ferreira [2002] found. By comparing the tilt angle and the magnetic field for this period of increasing solar activity, it is shown that the model is highly sensitive to changes in the tilt angle. Note that changes in the tilt angle are also used as input in the time-dependent function, which scales the drift coefficient over a solar cycle. It is shown that the tilt angle increases much faster for increasing solar activity than what is observed in cosmic ray intensities. As a result, the averaged tilt angle is introduced in the model, which is calculated by computing a simple moving average of the tilt angle values measured at Earth, which has a time forward shift effect. It is shown that implementing an averaged tilt angle in the model results in improved compatibility between the model and Voyager 1 observations.

Aspects of this study were presented at the following meetings:

- South African National Space Agency workshop, Hermanus, July 2014
- International workshop on cosmic rays: "From the Galaxy to the Heliosphere; A Numerical Modeling Approach", Potchefstroom, March 2014
- 28th International Conference on Computational Physics, St. Georges Hotel and Conference Center, July 2016

Chapter 2

Cosmic Rays and the Heliosphere

2.1 Introduction

In order to study long-term cosmic ray modulation in the heliosphere, an understanding of the Sun, the solar wind, the heliospheric magnetic field, solar activity, cosmic rays and the heliospheric structure is needed. This chapter briefly discusses the necessary background needed for the rest of this work.

2.2 The Sun

The Sun is our nearest star in the Milky Way, situated ~ 1 AU away from the Earth. Understanding the Sun is important for cosmic ray studies because the Sun drives the modulation of cosmic rays via magnetic fields, solar wind variations and the heliospheric structure [e.g. Stix, 2004]. All these are dependent on the solar cycle which is driven by the Sun. The solar mass consists primarily of $\sim 90\%$ hydrogen and $\sim 10\%$ helium, with traces of heavier elements such as carbon, nitrogen and oxygen [e.g. Kivelson and Russel, 1995]. The Sun has a radius of $r_{\odot} \simeq 7 \times 10^5$ km (~ 0.005 AU) and mass $M_{\odot} \simeq 2 \times 10^{30}$ kg, with a solar surface temperature of ~ 5778 K [e.g. Stix, 2004].

The internal structure of the Sun and its atmosphere are divided into different layers and zones, as shown in Figure 2.1. The solar interior is made up of the core, radiative zone and convective zone, while the solar atmosphere consists of the photosphere, chromosphere and the corona. The energy of the Sun is generated in the central core and is carried outwards by the photons through the radiative zone [e.g. Weiss and Tobias, 2000]. In the convection zone the energy is transported by turbulent convection motions which are visible on the photosphere. Temperatures at the base of the convection zone ranges from 1.5×10^7 K to 6×10^3 K at the photosphere. In the corona, which is the outer surface of the Sun, the temperature drops slightly and then rises to $\sim 3 \times 10^6$ K.

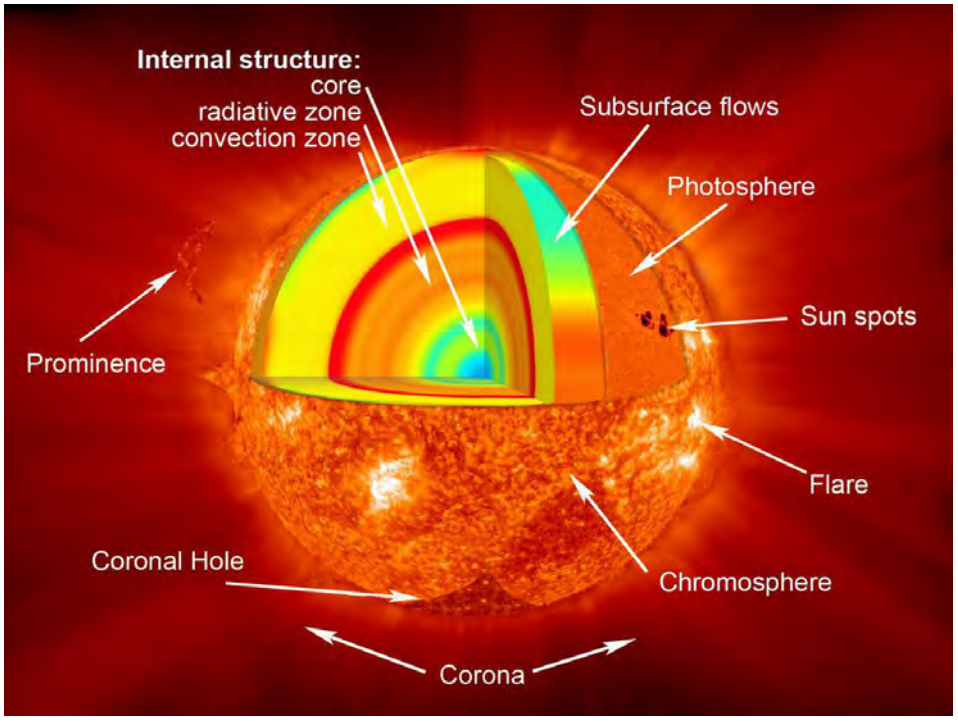

FIGURE 2.1: A graphical representation of the different layers of the Sun and some features on the surface of the Sun. From url: *http* : *//www.nasa.gov/mission_pages/sunearth/science/Sunlayers.html* doa: 29 April 2016.

2.3 Solar Activity Indices and the Solar Cycle

A variety of indices have been proposed as a way of measuring and representing solar activity. Most of these indices are correlated to each other through the 11-year solar cycle. These indices can be divided into different categories according to the way they are obtained or calculated [e.g. Shibata and Magara, 2011]. They can also be either direct (relating to the Sun) or indirect (relating to indirect effects caused by solar activity). Examples of observed solar varying features include sunspots, prominences, coronal streamers, solar flares, magnetic fields, coronal holes, energetic particles, cosmic ray modulation, X-ray emission and solar wind. Some of these are discussed next.

On the photosphere sunspots are clearly visible as irregular dark areas of intense magnetic fields on the surface of the Sun. Their magnetic fields are strong enough to inhibit energy convection in the regions below the photosphere [e.g. Bray and Loughhead, 1965, Stix, 2004], therefore resulting in dark appearance due to low temperatures. Sunspot number is used as a solar activity index and is useful for quantifying the level of solar activity.

Figure 2.2 shows the monthly-averaged sunspot numbers (according to *https* : *//www.merriam − webster.com/dictionary* (Accessed: 13 December 2016) " an arbitrary numerical value that is used to describe the Sun's spottedness, is the number of individual spots plus 10 times the number of disturbed regions, and depends upon the instrumental equipment and personal equation of the observer") as a function of time. From this figure a

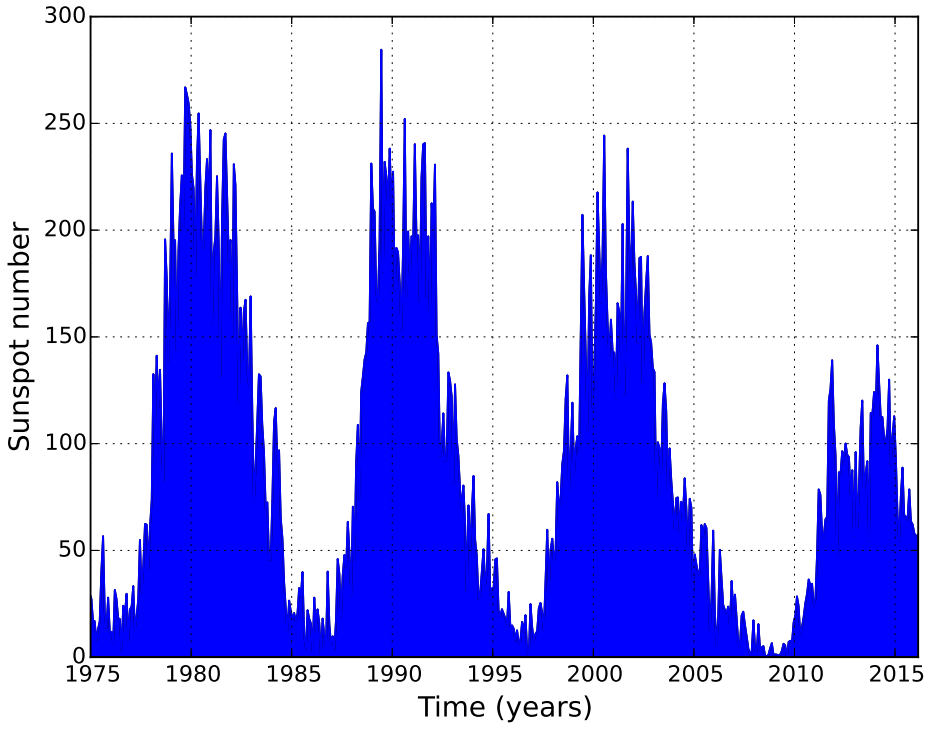

FIGURE 2.2: Monthly-averaged sunspot number from 1975 to 2016. The graph illustrates the 11-year solar cycle. Data from: the Solar Influences Data Analysis Center (*http* : *//sidc.be/index.php*3).

clear 11-year solar cycle is evident, corresponding to changes in solar activity. The successive maxima and minima in the sunspot number correspond to solar maximum and solar minimum respectively.

Solar flares are explosive events observed in the solar atmosphere filled with magnetized plasma. They produce high-energy particles travelling through the interplanetary space, which may possibly influence the environment on Earth [e.g. Shibata and Magara, 2011]. The flare index is also a solar activity index and estimates the total energy emitted by a flaring event. Other explosive events of almost similar nature are the coronal mass ejections (CMEs). These are eruptive occurrences of a magnetically charged plasma from the corona of the Sun into the heliosphere. This removes some of the built-up magnetic energy and plasma from the solar corona as the CME is carried along in an expanding magnetic field [Jokipii et al., 1997].

The left panel of Figure 2.3 shows an image of a flaring event from the Extreme ultraviolet Imaging Telescope (EIT). Emission in the spectral line 304 Å shows the upper chromosphere to be at a temperature of $\sim$ 60 000 K. The hottest areas appear almost white, while the darker red areas are an indicative of cooler temperatures. From the upper left in the clockwise direction, the images are shown from: 15 May 2001, 28 March 2000, 18 January 2000, and 2 February 2001. The right panel of the figure shows LASCO C2 image of a coronal mass ejection taken on

the 8th of January 2002 (url: *http : //sohowww.nascom.nasa.gov/gallery/bestofsoho.html* doa: 26 April 2016).

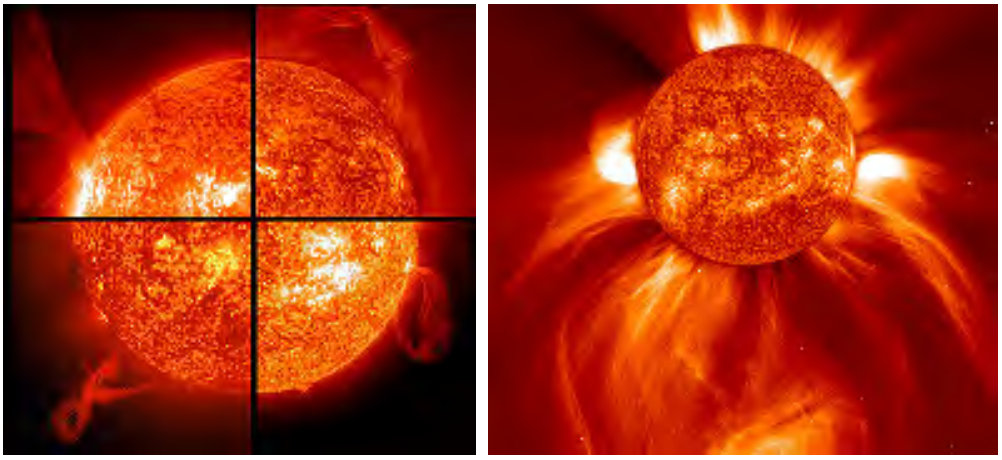

FIGURE 2.3: Left panel: Extreme ultraviolet Imaging Telescope (EIT) 304 Å image of a flaring event. Right panel: LASCO C2 image of a coronal mass ejection. From url: *https : //sohowww.nascom.nasa.gov/gallery/bestofsoho.html* doa: 26 April 2016.

The coronal index is a physical index measuring irradiance of the Sun in the coronal green line. Note that coronal green line is the strongest emission line in the visible spectrum of the solar corona, with a wavelength of 530.3 nm [Rybansky et al., 2001]. The coronal index is, however, related to the solar magnetic flux emerging from the photosphere and characterizes the coronal activity of the Sun. This index gives the reflection of the physical processes that take place in the interior of the Sun and shows many other periodicities other than the dominant 11-year cycle [e.g. Mavromichalaki et al., 2005], thus making possible the study of long-term, intermediate and short-term variations of the Sun as a star.

2.4 The Solar Wind

Observations by Carrington in 1859 of a solar flare that was followed by a large geomagnetic storm, suggested that solar activity has a connection with the magnetic disturbances observed on Earth [e.g. Hundhausen, 1972]. In 1929 Chapman suggested that large geomagnetic storms are a result of the interaction between the Earth's magnetic field and plasma clouds that are ejected during solar flares. Observations of periodic geomagnetic storms confirmed the existence of regions on the Sun that produce long-lived streams of charged particles in the interplanetary space. In the 1930s and 1940s Forbush observed the modulation of cosmic rays relative to geomagnetic storms and the 11-year solar activity cycle and it was suggested that the modulation was caused by the magnetic field embedded in plasma clouds from the Sun [e.g. Hundhausen, 1972].

Early in the 1950s, Biermann also suggested that a continuous outflow of particles from the Sun, which was not related to any flaring event, was responsible for the ionic comet tail pointing

away from the Sun [Biermann, 1951, 1957]. It was later pointed out by Alfvèn that the flow must be a magnetized plasma, which was later confirmed by direct observations outside of the Earth's magnetosphere. From the observations, Parker later developed a hydrodynamic model [Parker, 1960] describing the continuous expansion of the solar corona driven by large pressure difference between the solar corona and the interstellar plasma. This continuous supersonic coronal expansion is called the solar wind and its theoretical existence was verified experimentally in 1962 [Parker, 1965, Krieger et al., 1973].

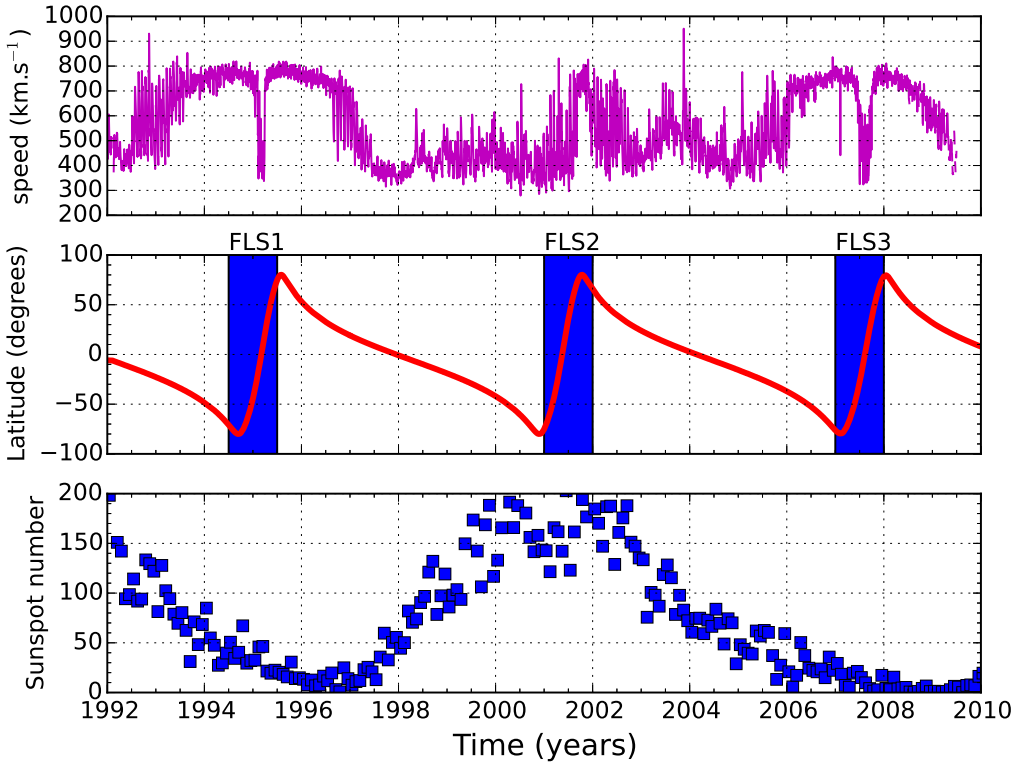

FIGURE 2.4: The solar wind speed (top panel) as a function of time as measured by the Ulysses spacecraft. Shown also in the middle panel is the Ulysses spacecraft latitude including the three fast latitude scan (i.e. FLS1, FLS2 and FLS3) periods highlighted in blue. The sunspot number is shown in the bottom panel. Ulysses data from *http* : *//cohoweb.gsfc.nasa.gov/* and the sunspot number data from: *http* : *//sidc.be/index.php*3.

An observed feature of the solar wind is that it is radially directed away from the Sun up to the termination shock. Observations also show that the solar wind speed is not uniform over all latitudes, especially during solar minimum. For solar minimum, the solar wind speed is divided into streams of fast and slow solar wind [Balogh et al., 2008]. Streamer belts are regarded as plausible sources of slow solar wind streams and the polar coronal holes as sources for the fast solar wind streams [Krieger et al., 1973, Gibson, 2001]. The solar wind speed is nearly constant out to $\sim$ 30 AU, from where it starts to decrease slowly due to the pickup of interstellar neutrals [Richardson and Stone, 2009].

The latitude dependence of the solar wind was observed by the Ulysses spacecraft when it completed its three fast latitude scans which covered both solar maximum and minimum conditions. This is shown in Figure 2.4. Note that the Ulysses spacecraft was launched on October 6, 1990 [Heber et al., 2003] and on the 13th September 1994 it reached the highest southern latitude of 80.2° S. Then it moved towards the north reaching a highest northern latitude of 80.2° N on 31 July 1995. This quick scan from southern to northern latitude is termed a fast latitude scan (FLS) period [e.g. Smith et al., 1995]. Figure 2.4 shows two other fast latitude scan periods completed by the Ulysses spacecraft. Shown for comparison is the sunspot number, which shows that the first (FLS1) and third (FLS3) fast latitude scans were during periods of decreased solar activity while the second (FLS2) fast latitude scan during increased solar activity period.

The solar wind speed also varies over solar cycles [Richardson and Stone, 2009]. As shown in Figure 2.4 during periods of solar maximum, the solar wind stream is slow and highly variable, resulting in no clear latitude dependence. However, for solar minimum the solar wind is slow near the equatorial region and fast near the poles, thus resulting in a clear latitude dependence.

In order to implement the solar wind speed profile in a modulation model, the solar wind velocity $\mathbf{V}(r,\theta)$ can be written as

$$\mathbf{V}(r,\theta) = V(r,\theta)\mathbf{e}_r = V_r(r)V_\theta(\theta)\mathbf{e}_r, \tag{2.1}$$

by assuming that the radial and latitudinal dependences are independent of each other [e.g. Hattingh, 1998, Ferreira, 2002, Langner, 2004, Ndiitwani et al., 2005, Manuel, 2012, Ngobeni, 2015, Prinsloo, 2016]. Here r denotes the radial distance, θ the polar angle and $\mathbf{e}_r$ the unit vector component in the radial direction. During solar minimum conditions the latitude dependence $V_\theta(\theta)$ of the solar wind velocity can be represented as:

$$V_\theta(\theta) = 1.5 \mp 0.5 \tanh\left(\frac{2\pi}{45}(\theta - 90^\circ \pm \varphi)\right), \tag{2.2}$$

with φ, a function that controls the transition from the slow to the fast solar wind speed, taken as 45° in the northern and southern hemisphere [e.g. Hattingh, 1998, Langner, 2004, Moeketsi et al., 2005], the top and bottom signs corresponds to the heliospheric quadrants described by $0^\circ \leq \theta \leq 90^\circ$ in the north and $90^\circ \leq \theta \leq 180^\circ$ in the south respectively. For solar maximum conditions no latitude dependence is assumed, therefore

$$V_\theta(\theta) = 1.0. \tag{2.3}$$

The radial dependence $V_r(r)$ of the solar wind can be assumed as:

$$V_r(r) = 400\{1 - \exp\left[\frac{40}{3}\left(\frac{r_\odot - r}{r_0}\right)\right]\}\text{km.s}^{-1} \tag{2.4}$$

with $r_0 = 1$ AU and $r_\odot \sim 0.005$ AU [e.g. Hattingh, 1998, Ferreira, 2002, Langner, 2004].

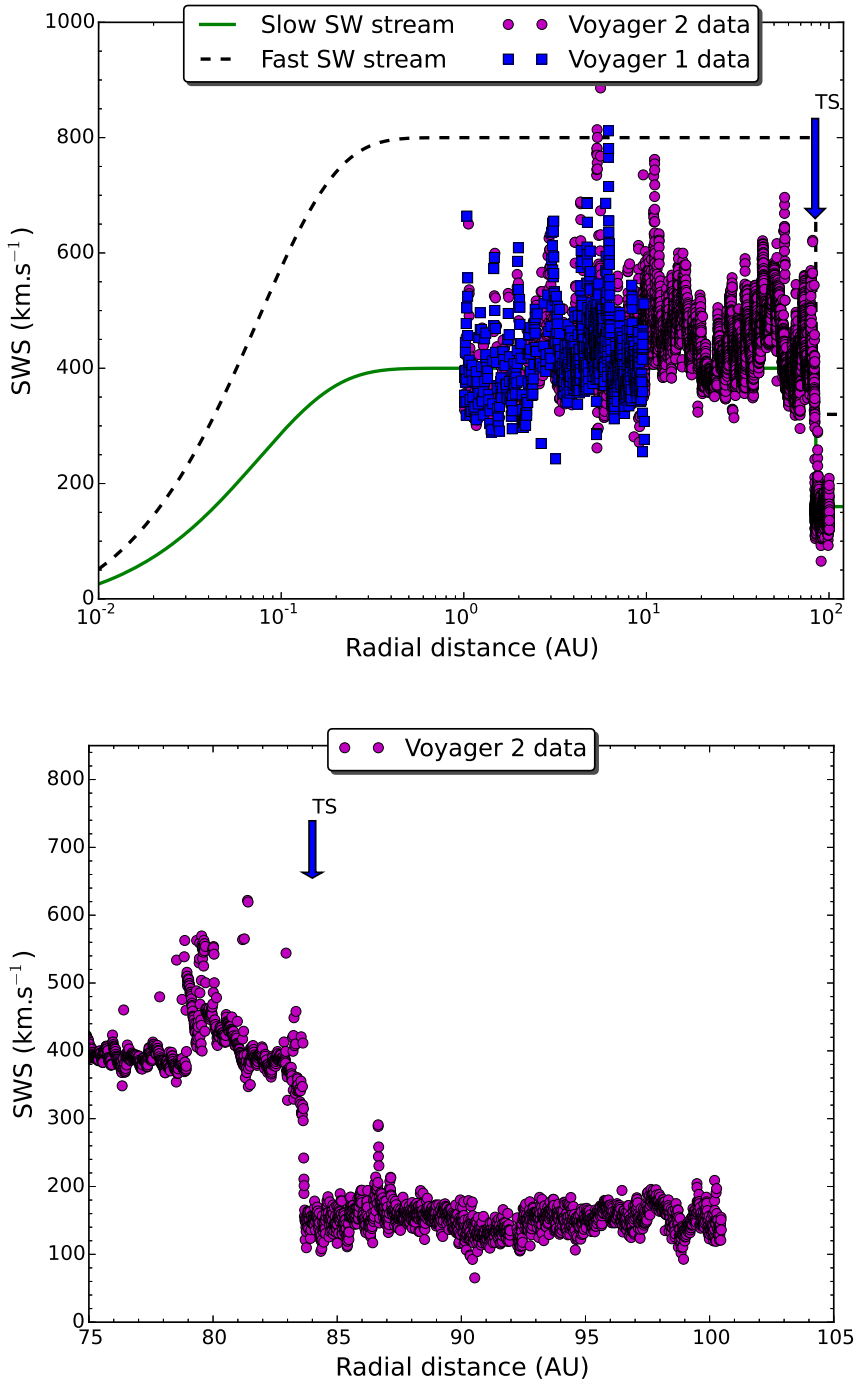

FIGURE 2.5: Top panel shows the modelled solar wind speed (SWS) as a function of radial distance for both fast and slow solar wind streams on a logarithmic scale and the bottom panel on a linear scale from the radial distance of 75 AU. Shown also for comparison is the Voyager 1 and 2 solar wind speed data. Data from *http* : *//cohoweb.gsfc.nasa.gov/*.

The supersonic solar wind across the heliospheric termination shock becomes subsonic due to the interaction with the interstellar medium, and deflects down the heliospheric tail [e.g. Weymann, 1960, le Roux et al., 1996, Langner, 2004]. This supersonic to subsonic transition was confirmed by the Voyager spacecraft (see Figure 2.5) when it crossed the termination shock, with Voyager 1 crossing it at $\sim$ 93.7 AU and Voyager 2 at $\sim$ 83.7 AU [Stone et al., 2008]. The top panel of Figure 2.5 shows the solar wind speed as a function of radial distance as modelled in Equation 2.4 and shown on a logarithmic scale for comparison. Shown also for comparison is Voyager 1 and 2 data. The bottom panel is a zoom in of the top panel from 75 AU - 105 AU, but on a linear scale. Shown here is the Voyager 2 solar wind speed data. In the bottom panel Voyager 2 solar wind speed measurements show that at the termination shock position the solar wind speed reduces from a supersonic speed of $\sim$ 400 km.s^{-1} to a subsonic speed of $\sim$ 150 km.s^{-1}. Note that the radial dependence of the solar wind speed in Equation 2.4 is assumed up to the termination shock.

2.5 The Heliospheric Magnetic Field

Electric currents in the Sun create complex magnetic field structures which extend out into the heliosphere [Aschwanden, 2005]. The concept of the frozen-in magnetic field in the out-blowing solar wind is due to the wind having extremely high electrical conductivity [e.g. Bellan, 2006, Fitzpatrick, 2014]. The important parameter to take note is the plasma β, which is defined as the ratio of the thermal energy density to the magnetic energy density.

Inside the Alfvèn radius ($\sim$ 0.1 AU), the magnetic energy density is larger than the thermal energy density ($\beta < 1$) and as a result the solar magnetic field is not modified by the solar wind [Fitzpatrick, 2014]. Beyond the Alfvèn radius, $\beta > 1$ and the continuous out-flow of the solar wind result in the transport of the solar magnetic field into the heliosphere, thus becoming the heliospheric magnetic field (HMF) [see also Chiuderi and Velli, 2014]. This magnetic field determines the transport of energetic particles in the heliosphere since they tend to follow the magnetic field lines. Discussed next is a model for the heliospheric magnetic field as used in this work and also a modification that is implemented.

2.5.1 The Parker Heliospheric Magnetic Field

At the solar source surface, located at heliocentric distance of $\sim 2.5 r_\odot$, the open magnetic field lines become radial [e.g. Wang and Sheeley, 1995]. The rotation of the Sun curves the HMF into a spiral form called the Parker spiral [Parker, 1958], which is given as

$$\mathbf{B} = B_0 \left(\frac{r_0}{r}\right)^2 (\mathbf{e}_r - \tan\varphi \mathbf{e}_\phi)[1 - 2H(\theta - \acute{\theta})], \tag{2.5}$$

with $\mathbf{e}_r$ and $\mathbf{e}_\phi$ unit vector components in the radial and azimuthal directions respectively, B_0 takes on the value of the average HMF magnitude at Earth, and $r_0 = 1$ AU. The Heaviside step function H determines the polarity of the magnetic field which causes changes in the HMF direction across the HCS, and this is given by:

$$H(\theta - \acute{\theta}) = \begin{cases} 0 & \text{for } \theta < \acute{\theta} \\ 1 & \text{for } \theta > \acute{\theta}, \end{cases} \tag{2.6}$$

with $\acute{\theta}$ the polar position of the heliospheric current sheet (HCS).

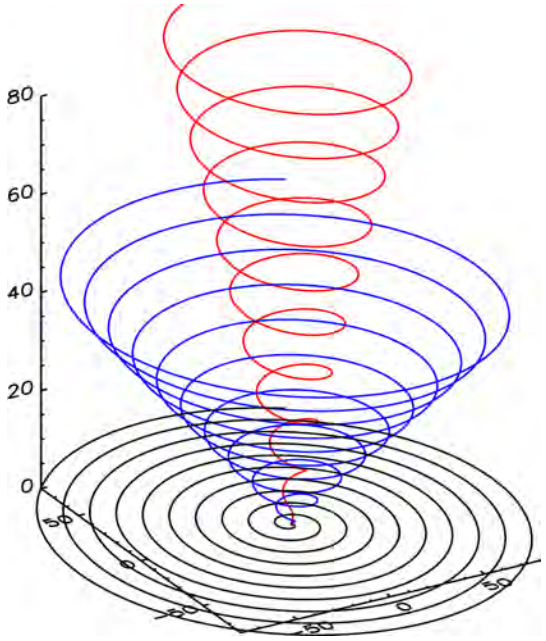

FIGURE 2.6: Illustration of the HMF lines of the Parker spiral as a function of radial distance in AU for three polar angles. From Sternal et al. [2009].

The Parker spiral angle is given as

$$\tan\varphi = \Omega \frac{(r - r_\odot)\sin\theta}{V}, \tag{2.7}$$

with the spiral angle φ defined as the angle between the radial direction and the average HMF at a certain position. In this equation $r_\odot \sim 0.005$ AU, $\Omega = 2.67 \times 10^{-6}$ rad.s^{-1}, the average angular rotation speed of the Sun and V the solar wind speed. This spiral angle gives an indication of how tightly wounded up the HMF spiral is. The magnitude of the Parker HMF throughout the heliosphere is given as

$$B = B_0 \left(\frac{r_0}{r}\right)^2 \sqrt{1 + (\tan\varphi)^2}, \tag{2.8}$$

for distances up to the termination shock. Figure 2.6 shows a basic structure of the Parker spiral, with the three lines (i.e. black, blue and red lines) corresponding to the Parker field lines at different polar angles.

2.5.2 Jokipii-Kòta Modification

It has become a practice by authors using modulation models to incorporate some sort of HMF modification, especially over the heliospheric poles, as deviations from the Parker spiral may occur away from the ecliptic plane [see e.g. Jokipii and Kóta, 1989, Moraal, 1990, Smith and Bieber, 1991, Fisk, 1996, Burger and Hattingh, 2001, Fisk, 2001, Burger and Hitge, 2004, Burger et al., 2008, Vos, 2012, Raath, 2015]. In this work the Jokipii-Kòta modification is implemented and discussed next.

Jokipii and Kóta [1989] argued that the solar surface, where the "feet" of the magnetic field lines occur, is a granular turbulent surface, especially in the polar regions. This turbulence may cause temporal deviations from the smooth Parker geometry should the "footprints" of the polar field lines wander randomly. The net effect of this will be a highly irregular and compressed field lines.

These authors suggested a modification given by $\delta(\theta)$ and with this modification, Equation 2.8 becomes

$$B_m = B_0 \left(\frac{r_0}{r}\right)^2 \sqrt{1 + \left(\frac{\Omega\,(r - r_\odot)}{V} \sin\theta\right)^2 + \left(\frac{r\delta(\theta)}{r_\odot}\right)^2}. \tag{2.9}$$

The above modification alters B so that in the polar regions it decreases as r^{-1} instead of r^{-2} for large r. The modification is given as:

$$\delta(\theta) = \frac{\delta_m}{\sin\theta}, \tag{2.10}$$

with $\delta_m = 8.7 \times 10^{-5}$ and $\delta(\theta) = 0$ giving the Parker geometry in the ecliptic plane. The θ dependence is to keep magnetic field divergence free [e.g. Balogh et al., 2001, Langner et al., 2006]. For $\delta(\theta) = 0.001$ [see e.g. Hattingh, 1998, Ferreira, 2002, Langner, 2004, Manuel, 2012] the magnitude of the HMF changes significantly in the polar regions but not in the equatorial plane. The purpose of this modification is then to reduce drift effects experienced by cosmic rays at the polar regions [Potgieter and Haasbroek, 1993]. This modification is supported qualitatively by the HMF measurements made by the Ulysses over the polar regions [Balogh et al., 2001].

2.6 The Heliospheric Current Sheet

The heliospheric current sheet is a co-rotating structure in the heliosphere that divides the HMF into two hemispheres of opposite polarity [see e.g. Smith, 2001, Riley et al., 2002, Balogh and Erdos, 2013], with the HMF pointing towards the Sun in one hemisphere and away from the Sun in another hemisphere, as illustrated in Figure 2.7. Due to the Sun's rotation, the current sheet oscillates, forming series of peaks and valleys. The shape of the current sheet depends on the tilt angle, solar rotation and solar wind speed. The wavy structure of the current sheet is due to the magnetic axis being tilted relative to the rotational axis of the Sun, by the tilt angle α [Hoeksema, 1992].

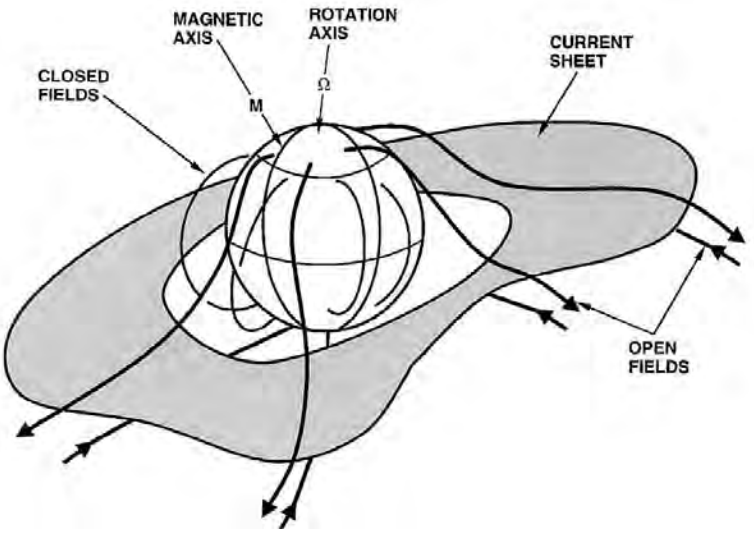

FIGURE 2.7: Schematic illustration of the heliospheric current sheet, separating the open fields (which are at opposite polarities) from the north and south solar magnetic poles. From Smith [2001].

The waviness of the current sheet is correlated to the solar activity of the Sun, meaning, during times of low solar activity, the tilt angle can go as low as $\sim 5°$, see Figure 2.8, thus in turn resulting in decreased waviness of the current sheet. But during periods of high levels of solar activity the tilt angle can increase to $\sim 75°$ and resulting in increased waviness of the current sheet. Figure 2.8 shows a graph of the HCS tilt angle as a function of time computed by two models [Hoeksema, 1992], i.e. the classic model which uses line-of-sight boundary conditions at the source surface located at $2.5r_\odot$ and the new model which uses the radial boundary conditions at the photosphere and a source surface located at $3.5r_\odot$ (see $http://wso.stanford.edu/$ for detailed discussion of these models). It also follows from the figure that the tilt angle is correlated to solar activity, which is related by the sunspot number counts showing a clear 11-year cycle.

The existence of the HCS is clearly evident in the contour plots of the coronal magnetic field shown in Figure 2.9. These were computed using the Potential Field Source Surface (PFSS) model [Schatten et al., 1969]. The contour plots shown in this figure are for February 1987

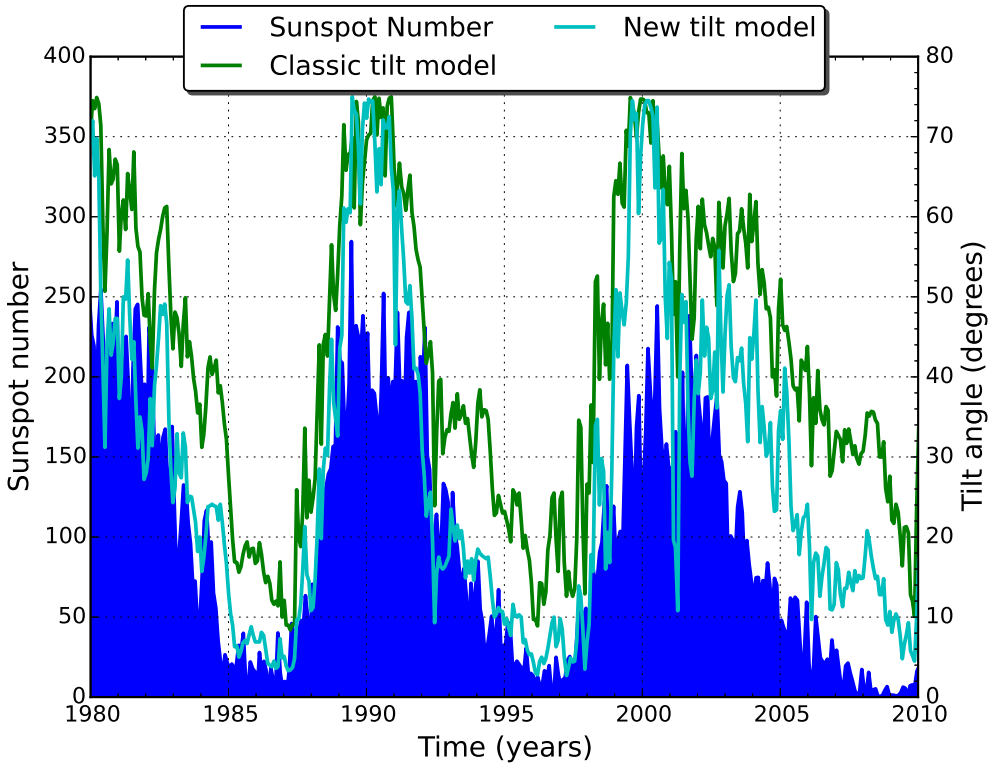

FIGURE 2.8: Computed tilt angle α for two models (i.e. classical and new model) as a function of time from 1980 - 2010. Shown also is the monthly averaged sunspot number for comparison. Tilt angle data from: $http://wso.stanford.edu/$ and the sunspot number data from: $http://sidc.be/index.php3$.

(top panel) and July 2000 (bottom panel), corresponding to low solar activity and increased solar activity periods, respectively. On each panel the HCS (or neutral line) is shown by a black line separating regions of opposite polarity, which are shown as grey shades. This neutral line represents a magnetic equator. For decreased solar activity periods this line is seen staying close to the solar equator, but reaching higher heliolatitudes for increased solar activity periods.

As discussed and shown in the next chapters, the HCS has a significant effect on the cosmic ray transport and modulation in the heliosphere as first outlined by Jokipii et al. [1977] and Potgieter and Moraal [1985]. A theoretical expression for HCS for a constant and radial solar wind speed was derived by Jokipii and Thomas [1981] and is given as,

$$\acute{\theta} = \frac{\pi}{2} + \sin^{-1}\left(\sin\ \alpha\ \sin\left[\phi + \frac{\Omega(r - r_0)}{V}\right]\right), \tag{2.11}$$

where $\acute{\theta}$ is the polar angle of the HCS. For smaller tilt angle Equation 2.11 reduces to

$$\acute{\theta} = \frac{\pi}{2} + \alpha \sin\left[\phi + \frac{\Omega(r - r_0)}{V}\right]. \tag{2.12}$$

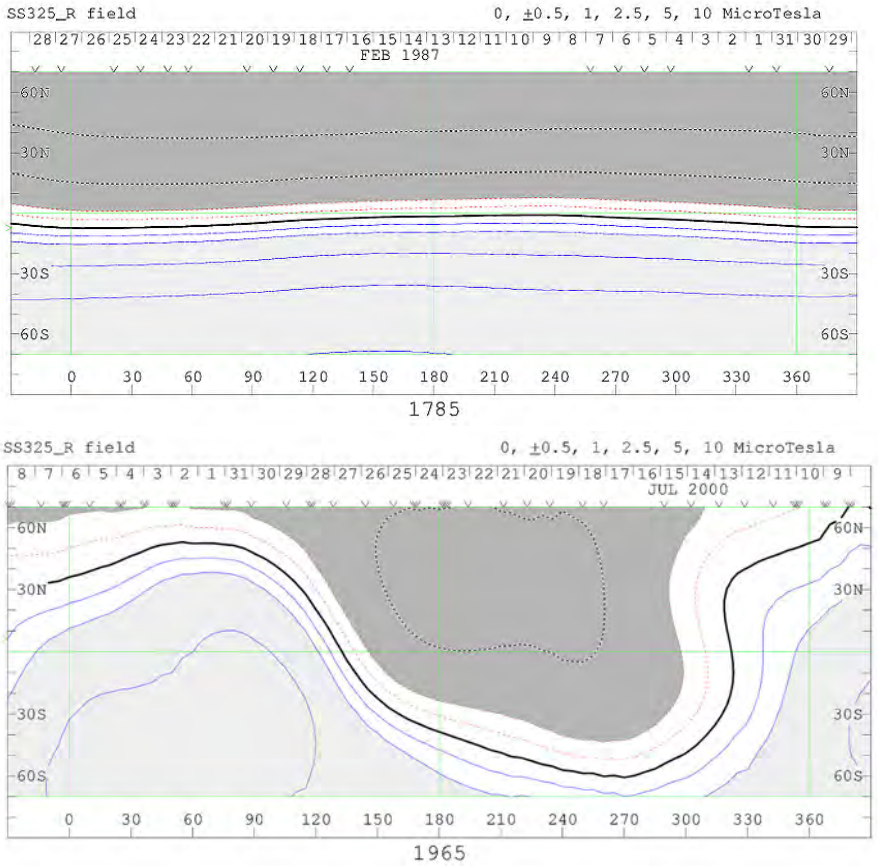

FIGURE 2.9: Contour plots of the coronal magnetic field computed using the Potential Field Source Surface model with a source surface at $3.25r_{\odot}$. These contour plots are shown for Carrington rotation 1785 (February 1987) on the top panel as an example of solar minimum and Carrington rotation 1965 (July 2000) as an example of solar maximum on the bottom panel. The thick solid black line corresponds to the neutral line. From Wilcox Solar Observatory (url: $http://wso.stanford.edu/$ doa: 21 October 2013).

To include the polarity of the HMF, Equation 2.12 is used in Equation 2.5, which can be re-written as

$$\mathbf{B} = AB_0 \left(\frac{r_0}{r}\right)^2 (\mathbf{e}_r - \tan\psi \mathbf{e}_\phi)[1 - 2H(\theta - \acute{\theta})]. \tag{2.13}$$

Here $A = \pm 1$ is a constant determining the polarity of the HMF which alternates every 11 years. Periods when the HMF in the northern solar hemisphere is directed outward and inward in the southern solar hemisphere are called $A > 0$ periods with $A = +1$. For $A < 0$ periods, the direction of the HMF reverses and $A = -1$. The Heaviside step function as given by Equation 2.6, changes the HMF polarity across the HCS. But because of the numerical instabilities when it is used directly in the numerical model, Hattingh [1998] approximated this function as

$$\acute{H}(\theta) \approx \tanh[2.75(\theta - \acute{\theta})]. \tag{2.14}$$

Several authors have simulated the global effects of HCS on cosmic ray transport using 2D numerical modulation models [e.g. Potgieter and Moraal, 1985, Hattingh and Burger, 1995b, Hattingh, 1998, Ferreira, 2002, Langner, 2004]. The 2D simulation of the HCS used in this study is discussed in the chapter to follow.

2.7 Global Features of the Heliosphere

The Sun and the solar system move in a partially ionized local interstellar medium (LISM) which comprises of many clouds of different densities, temperatures, magnetic field strengths and flow speeds [e.g. Richardson et al., 2008, Muller et al., 2009, Pogorelov et al., 2009, Frisch and McComas, 2013]. The solar wind interacts with the local interstellar medium, and this interaction results in the formation of a bubble referred to as the heliosphere [Opher et al., 2006, Pogorelov et al., 2008, Borovikov et al., 2011]. The hydrodynamic and magneto-hydrodynamic models describing the interaction between these two mediums imply that the solar wind-LISM interaction can be described as a steady state between two distinct fluids, whereby their pressures balance [e.g. Richardson and Stone, 2009].

The boundary between the solar and interstellar winds where steady state is established is called the heliopause. Because the two winds are supersonic, this results in a shock forming upstream in each flow [e.g. Zank et al., 1996, Opher et al., 2006, Ferreira et al., 2007, Lee et al., 2009, Jokipii, 2013, Richardson and Burlaga, 2013]. At the shock, both plasmas will experience compression, heating and deceleration to subsonic speeds. The flow direction also changes so that the interstellar wind plasma moves around the heliopause and the solar wind plasma down the heliotail. Apart from the solar wind-LISM interaction, neutrals can cross freely between these two plasma regions because they are not bound by magnetic fields [e.g. Fahr and Scherer, 2004, Lee et al., 2009, Richardson and Stone, 2009, Stone et al., 2013].

The shock in the solar wind is called the solar wind termination shock and in the local interstellar medium, the bow shock [Scherer and Fahr, 2003*a*]. However, if the interstellar wind is not supersonic, a bow shock does not exist. But for a supersonic interstellar wind with an interstellar magnetic field strength less than 3 μG the bow shock may exist [e.g. Zank et al., 1996, Pogorelov et al., 2008, Heerikhuisen and Pogorelov, 2011]. Recent observations however from the Interstellar Boundary Explorer (IBEX) suggest a less dynamic pressure due to slower relative motion of the Sun relative to the interstellar medium. This may therefore result in rather a bow wave forming [see e.g. McComas et al., 2012, Zank et al., 2013, for reviews] than a bow shock.

As shown in Figure 2.10, due to the motion of the LISM relative to the Sun, the heliosphere has an elongated structure, compressed in the upwind direction and elongated in the downwind direction, resulting in the so-called heliospheric tail [e.g. Marsch et al., 2001]. The inner

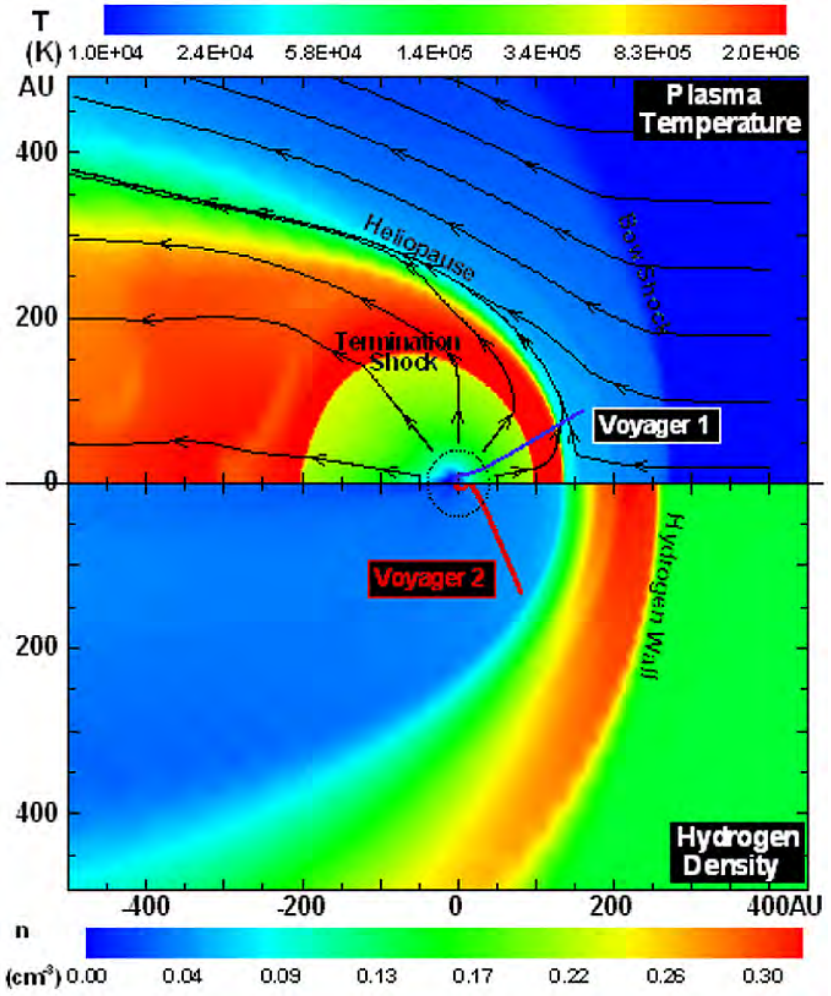

FIGURE 2.10: The equatorial plot of the heliosphere from a plasma (top panel) and neutral hydrogen (bottom panel) perspective. The color bar on the top panel shows the plasma temperature and the color bar on the bottom panel shows the neutral hydrogen density. Shown also are the main heliospheric boundaries, the plasma flow by flow lines and the hydrogen wall. From Richardson and Stone [2009].

heliospheric measurements made by Ulysses spacecraft revealed a significant latitudinal dependence in the solar wind speed. During solar minimum conditions the heliospheric structure is more elongated in the solar poleward direction, but during solar maximum conditions, the elongation is much more reduced [e.g. Scherer and Fahr, 2003*b*, Ferreira and Scherer, 2004].

Because the solar wind pressure changes with the solar cycle, the distance to the heliopause and also the termination shock position vary with the solar cycle, which results in the maximum distance predicted occurring near solar minimum [e.g. Pauls and Zank, 1996, Ferreira et al., 2004, Pogorelov et al., 2013]. However, Pauls and Zank [1996] also showed that, when including the effects of charge exchange between the solar wind and interstellar neutral hydrogen self-consistently in a model, the elongation is reduced.

The magnetic field and plasma flow on both sides of the heliopause is significantly compressed by the interaction of the solar wind with the LISM [Richardson and Stone, 2009, Richardson,

2011, McComas et al., 2012, Richardson and Burlaga, 2013, Pogorelov et al., 2014]. The magnetic field compresses and increases closer to the heliopause [e.g. Florinski et al., 2003, Izmodenov and Baranov, 2006, Muller et al., 2009].

Voyager 1 crossed the termination shock at ~ 94 AU, 34.1° North heliolatitude [e.g. Stone et al., 2005, Ness, 2006] and Voyager 2 crossed the shock at ~ 84 AU, 31.6° South heliolatitude [e.g. Richardson et al., 2008, Stone et al., 2008]. Upon crossing the shock, the spacecraft observed an increase in the strength of the magnetic field, plasma density and temperature and a decrease in the solar wind speed. This is shown in Figure 2.11, which shows the daily averaged values of the solar wind speed, plasma density and plasma temperature observed by the Voyager 2 spacecraft across the termination shock.

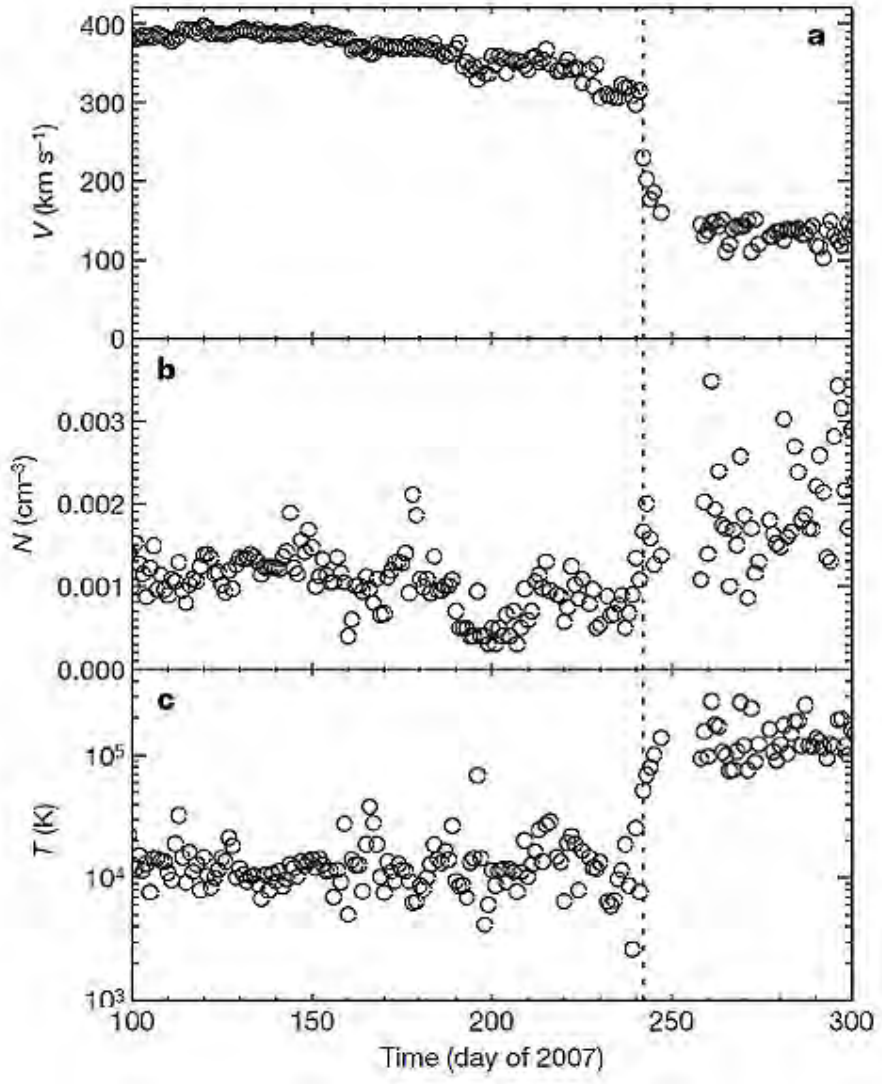

FIGURE 2.11: Daily averaged (a) radial solar wind speed V, (b) density N and (c) temperature T measured by plasma (solar wind) experiment on-board Voyager 2 spacecraft. The termination shock position is indicated by the vertical dashed line. From Richardson et al. [2008].

The heliosheath can be subdivided into the inner and outer heliosheath, with the inner heliosheath being the volume between the termination shock and the heliopause and the outer heliosheath the volume between the heliopause and the bow shock (or bow wave) [Scherer et al., 2011]. However, Voyager 1 is believed to have crossed the heliopause at 122 AU [see e.g. Gurnett et al., 2013, Stone et al., 2013, Webber and McDonald, 2013] after measuring a sudden decrease in the intensity of low-energy particles. But the crossing of the heliopause is still considered controversial by Fisk and Gloekler [2014] and Gloekler and Fisk [2015].

2.8 Cosmic Rays

Different types of cosmic rays, which are energetic charged particles either entering or being produced in the heliosphere, reach Earth and cover a wide range of energies. The extraterrestrial origin of cosmic rays was discovered by Victor Hess in 1912 when he measured an increase of ionizing radiation with increasing height during his balloon experiments [e.g. as discussed in reviews by Heber and Potgieter, 2008, Schroder, 2012]. Cosmic rays consist mainly of protons, but also heavier atomic nuclei, electrons, positrons and anti-protons. Cosmic rays can be classified as follows:

1. Galactic cosmic rays (GCRs) are energetic ions (protons and heavy ions, such as helium, carbon and oxygen) and electrons which enter the heliosphere. GCRs are accelerated by shock waves in the galaxy from supernova remnants, pulsars, or active galactic nuclei [e.g. Büsching et al., 2008*a*,*b*, Potgieter, 2013*a*]. Their outstanding feature is their energy spectra which shows a power-law distribution from $\sim 10^6$ eV to $\sim 10^{20}$ eV and also includes at least two "breaks" in the power-law [Heber and Potgieter, 2008]. Their elemental composition comprises primarily of fully ionised hydrogen nuclei ($\sim 98\%$), and $\sim 2\%$ electrons, positrons and anti-protons. Below ~ 30 GeV GCRs become vulnerable to solar and heliospheric modulation effects [Strauss and Potgieter, 2014]

2. Anomalous cosmic rays (ACRs) enter the heliosphere as neutral interstellar atoms and are observed as ACRs. They were first discovered as anomaly in the energy spectrum of GCR helium and got their name from the unusual shape of their energy spectrum below ~ 100 MeV per nucleon [Fisk et al., 1974, Heber and Marsden, 2001, Potgieter, 2013*a*]. After they were discovered, it was proposed that they originated as interstellar neutral gas that could enter the heliosphere, become ionized and then accelerated in the outer heliosphere. [see e.g. Gloeckler et al., 2009, Strauss et al., 2010, for more review on ACRs and their modulation in the heliosphere]. ACRs are not considered in this work.

3. Solar energetic particles (SEPs) which are energetic particles (reaching energies as high as ~ 1 GeV for protons and ~ 100 MeV for electrons) originating near the Sun and which

are associated with the solar flares and/or large coronal mass ejections [e.g. Balogh et al., 2008, Usoskin, 2008, Dressing et al., 2014]. SEPs are not considered in this work.

4. Jovian electrons are energetic particles with energies up to 100 MeV and originate from the magnetosphere of Jupiter [see Ferreira et al., 2001, Ferreira, 2002]. They were first discovered by the Pioneer 10 spacecraft during the Jupiter fly-by [e.g. Simpson et al., 1974, Chenette et al., 1974]. They dominate cosmic ray intensities in the inner heliosphere [see also Potgieter and Nndanganeni, 2013, Strauss et al., 2013]. Jovian electrons are not considered in this work.

2.9 Galactic Cosmic Ray Spectra

Galactic cosmic rays are accelerated during supernova explosions and are mainly distributed in a power law $j \propto E^{-\gamma}$, with the spectral index of $\gamma \approx 2.6$, kinetic energy E in units MeV/nucleon and differential intensity j in units particles m^{-2} s^{-1} sr^{-1} MeV^{-1} [e.g. Wibig and Wolfendale, 2009]. At energies $E > 10^{15}$ GeV the galactic cosmic rays experience a spectral break known as the "knee" of the spectrum and the spectrum becomes steeper with $\gamma \approx 3.1$. But for $E < 20$ GeV, cosmic rays measured at Earth have a different spectral index, i.e. $\gamma \neq 2.6$, due to solar modulation effects in the heliosphere [e.g. Ferreira, 2002, Potgieter, 2013*a*].

2.9.1 Heliopause Spectra for Cosmic Ray Protons

The galactic cosmic ray energy spectra serves as an important boundary condition in modulation models which calculate cosmic ray intensities. Therefore a proper knowledge of the exact shape of the proton energy spectra in the LISM is crucial for modulation study of this work. However, this work only focuses on calculating time-dependent modulation at one energy and for this purpose Voyager 1 observations close to the heliopause are used as input values at what is called the modulation boundary.

This is similar to Manuel [2012] who assumed input spectra of 133 - 242 MeV and > 70 MeV Voyager 1 proton measurements at $\sim$ 119 AU, whose intensity values are specified at the heliospheric modulation boundary. Figure 2.12 shows the assumed proton spectra with two intensity values as indicated and as used by Manuel [2012] and in the rest of this work. However, there are recently more reliable constructed heliopause spectrum (HPS) [e.g. Vos, 2012, Potgieter et al., 2014, Potgieter, 2014, Vos, 2016], but for the purpose outlined in this work, a different choice of HPS will have an effect on the energy-dependence of modulation and not on the time-dependence of modulation which is the topic of this study.

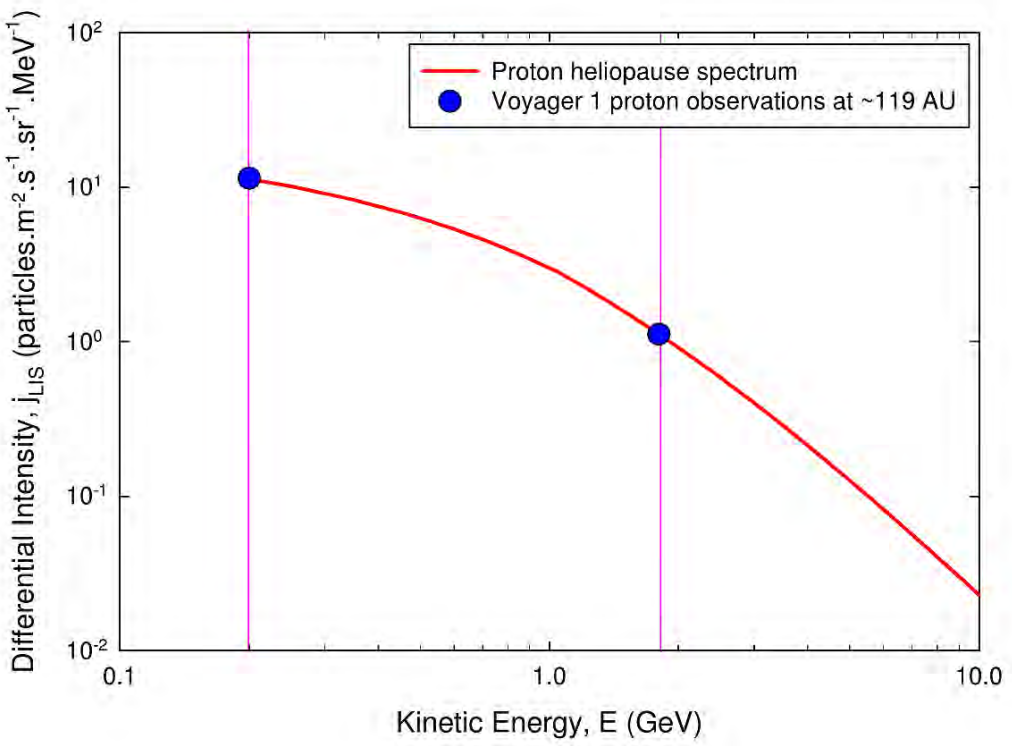

FIGURE 2.12: The assumed proton HPS from the Voyager 1 measurements of 133 - 242 MeV and $E > 70$ MeV protons at $\sim$ 119 AU. The two vertical lines correspond to kinetic energy 200 MeV and 1.8 GeV ($\sim$ 2.5 GV). From Manuel [2012].

2.10 Cosmic Rays Over a Solar Cycle

In the heliosphere cosmic rays experience changes in their intensities as a function of energy, position and time due to radially out-blowing solar wind and the embedded HMF. Upon entering the heliosphere, cosmic rays experience four major modulation processes [Parker, 1965]. A detailed discussion of these processes is given in the next chapter. The transport of cosmic rays in the heliosphere is also influenced by the levels of solar activity and short-scale variability in the solar wind [e.g. Perko and Fisk, 1983, le Roux and Potgieter, 1990, 1992, 1995, Florinski et al., 2013, Potgieter, 2013*a*]. This process is called time-dependent cosmic ray modulation.

This time-dependent cosmic ray modulation gives rise to an 11-year cycle in cosmic ray intensities in relation to solar cycle. Also visible is a 22-year cycle which is related to the HMF polarity reversal [e.g. Babock, 1961, Leighton, 1969] and particle drifts. This long-term modulation of cosmic rays is recorded by different neutron monitors. Figure 2.13 shows the recorded cosmic ray relative count rates by the Hermanus neutron monitor with a cut-off rigidity of $\sim$ 4.6 GV. Shown also is the sunspot number which is in anti-correlation with the cosmic ray counts.

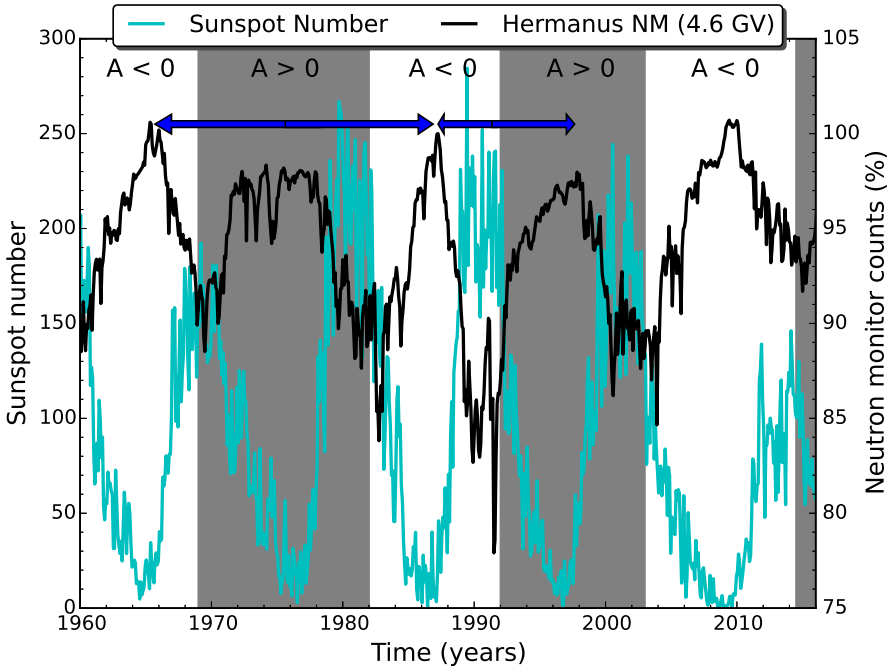

FIGURE 2.13: The Hermanus cosmic ray neutron monitor count rate normalised to 100% in March 1987. Shown also for comparison is the sunspot number. The shaded area represent the A > 0 HMF polarity cycle and the unshaded area represent the A < 0 polarity cycle. Neutron monitor counts data obtained from url: *http* : *//www.nwu.ac.za/neutron − monitor − data* doa: 24 August 2016) and the sunspot number data from: *http* : *//sidc.be/index.php*3.

To understand long-term cosmic ray modulation, which is the topic of this work, a 2D well-established time-dependent modulation model including the modified compound approach of Manuel [2012] and Manuel et al. [2014] to compute cosmic ray intensities over a solar cycle was used and results compared to different spacecraft observations. These spacecraft are discussed briefly in the next section.

2.11 Voyager Spacecraft Mission

Data provided by spacecraft missions plays a vital role in the understanding and modelling of the structure of the heliosphere and cosmic rays. For example, Luna 1 which was launched in 1959, was the first to detect the solar wind as predicted by Parker [1958]. Later in 1962, Marina 2 confirmed the existence of the solar wind and provided the measurements of its properties [Balogh et al., 2008]. Since then, other numerous space missions have been providing us with in-situ observations. This work uses cosmic ray observations mainly from Voyager 1 and Voyager 2 spacecraft to compare with numerical model results for compatibility. These are briefly discussed next.

The Voyager interstellar mission is a National Aeronautics and Space Administration (NASA) space mission managed by the Jet Propulsion Laboratory to explore the solar system and even

beyond the region of the outer planets [Kohlhase and Penzo, 1977]. The mission consists of Voyager 1 and Voyager 2 spacecraft, probing the northern and southern hemispheres of the heliosphere, respectively. Voyager 2 was launched on the 20th August 1977, while Voyager 1 on the 5th September 1977 [Burlaga and Behannon, 1982]. Voyager 1 is currently the farthest man-made object from Earth (at a distance of $\sim$ 135.7 AU from Earth) and both spacecraft are still functional and sending scientific information back to NASA's Deep Space Network at Earth. See also *http* : *//voyager.jpl.nasa.gov/* for more resources on the Voyager spacecraft.

Experiments on-board both Voyager 1 and 2 are Imaging Science, Infrared Radiation, Photopolarimetry, Ultraviolet Spectroscopy, Radio Science, Cosmic Ray Particles, Low Energy Charged Particles, Magnetic Fields, Planetary Radio Astronomy, Plasma Particles and Plasma Waves [Behannon et al., 1977, Bridge et al., 1977, Kohlhase and Penzo, 1977, Krimigis et al., 1977, Scarf and Gurnett, 1977, Stone et al., 1977]. Not all of these instruments are still functional.

The Cosmic Ray System (CRS) instrumentation on both Voyager 1 and 2 is still active. This is used to investigate the energy spectra and composition of cosmic ray particles. The CRS investigation consists of 3 telescopes, i.e., High Energy Telescope System (HETS), Low Energy Telescope System (LETS), and the Electron Telescope (TET) [Stone et al., 1977]. Of specific interest to this study is the modulation of cosmic ray proton intensities through a time-dependent modulation model, therefore the numerical model results are compared with Voyager 1 and 2 observations from the CRS instrument.

2.12 Summary

In this chapter, some background regarding modulation of cosmic rays in the heliosphere was given. Features and structure of the heliosphere, which is the modulation volume for cosmic rays, were discussed. Also discussed was the Sun, which is a rotating magnetic star from which plasmatic atmosphere blows radially away from its surface, thus forming the solar wind. This solar wind and embedded magnetic field change the intensities of cosmic rays entering the heliosphere as a function of time, energy and position.

The solar wind carries off in it the magnetic field of the Sun into the interplanetary space and the embedded magnetic field is called the HMF. The basic structure of the HMF used in this study is the Parker spiral and modified at the poles following Jokipii-Kòta modification. In one solar hemisphere HMF lines are directed towards the Sun and away from the Sun in the other hemisphere. These oppositely directed open magnetic field lines that originate from the solar surface are separated by the structure encircling the Sun called the HCS.

Since the rotation axis and the magnetic axis of the Sun is tilted by α, the tilt angle, as the Sun rotates it forms a current sheet which oscillates about the solar equator, therefore, forming a series of peaks and valleys spiralling outward and forming HCS. The waviness of the HCS is

dependent on the solar activity. The HCS has a significant effect on the transport of cosmic rays in the heliosphere.

Evident in observed cosmic ray intensities is a prominent $\sim$ 11 year solar cycle and a $\sim$ 22 year magnetic cycle, which is due to the polarity reversal of the Sun's magnetic field. The aim of this work was to study time-dependent cosmic ray modulation using numerical models. Model results are compared to different spacecraft observations for interpretation.

Chapter 3

Cosmic Ray Transport

3.1 Introduction

Upon entering the heliosphere (modulation volume), cosmic rays encounter the solar wind plasma with the Sun's magnetic field embedded in this plasma. This encounter alters cosmic ray intensities as a function of time, position and energy relative to their interstellar values. Their transport is seen as the change of their pitch-angle averaged distribution function $f(\mathbf{r}, p, t)$ that depends on position and energy. These charged particles are modulated through frequent pitch-angle scattering by turbulent magnetic fluctuations. They are also convected with the plasma at the plasma speed and as a parcel of plasma contracts or expands the particles will experience adiabatic heating or cooling. Cosmic rays also experience large-scale drift motion across the mean magnetic field. These processes and their implementation in a numerical model are discussed in this chapter.

3.2 Parker's Transport Equation

Within the heliosphere, there are four major cosmic ray modulation processes, i.e.

1. Convection due to the solar wind propagating outwards from the Sun [e.g. Parker, 1958, 1960].

2. Energy changes due to the solar wind velocity expanding or compressing, therefore cosmic rays undergo adiabatic cooling (decelerate) [e.g. Parker, 1965] or heating (accelerate) [e.g. Ferreira et al., 2007]. Acceleration may also be due to diffusive shock acceleration at the solar wind termination shock [e.g. Potgieter and Moraal, 1988, le Roux et al., 1996, Langner, 2004] or continuous stochastic acceleration in the inner heliosheath [e.g. Ferreira et al., 2007, Strauss et al., 2010].

3. Diffusion along HMF (parallel) and across HMF lines (perpendicular) [e.g. Bieber et al., 1994, Potgieter, 1996, Shalchi et al., 2004, Teufel and Schlickeiser, 2003, Engelbrecht, 2008].

4. Drifts due to the gradient and curvature of the HMF or any changes in the magnetic field direction in the current sheet [e.g. Jokipii et al., 1977, Potgieter and Moraal, 1985, Hattingh and Burger, 1995b, Burger et al., 2000].

Parker [1965] combined all these modulation processes into a transport equation (TPE) given as

$$\frac{\partial f}{\partial t} = -\left(\mathbf{V} + < \mathbf{v}_d >\right) \cdot \bigtriangledown f + \nabla \cdot \left(\mathbf{K_S} \cdot \bigtriangledown f\right) + \frac{1}{3}\left(\nabla \cdot \mathbf{V}\right) \frac{\partial f}{\partial \ln P} + Q, \tag{3.1}$$

where t is the time, P the rigidity, $\mathbf{V}$ solar wind velocity, $\mathbf{K_S}$ the symmetric diffusion tensor, Q is any particle source inside the heliosphere and $< \mathbf{v}_d >= \nabla \times K_A \mathbf{e}_B$ the pitch angle averaged guiding center drift velocity for a near isotropic distribution function f. This function is related to the differential intensity j by $j = P^2 f$. The rigidity P in GV is defined as the momentum per charge of the particles i.e. $P = \frac{pc}{q}$ with p the particle momentum, q the charge and c the speed of light in vacuum.

Rewriting Equation 3.1 in a three-dimensional (3D) spherical coordinate system rotating with the Sun, gives

$$\begin{aligned}
\frac{\partial f}{\partial t} = & \left[\frac{1}{r^2}\frac{\partial}{\partial r}(r^2 K_{rr}) + \frac{1}{r\sin\theta}\frac{\partial}{\partial\theta}(K_{\theta r}\sin\theta) + \frac{1}{r\sin\theta}\frac{\partial K_{\phi r}}{\partial\phi} - V\right]\frac{\partial f}{\partial r} \\
& + \left[\frac{1}{r^2}\frac{\partial}{\partial r}(rK_{r\theta}) + \frac{1}{r^2\sin\theta}\frac{\partial}{\partial\theta}(K_{\theta\theta}\sin\theta) + \frac{1}{r^2\sin\theta}\frac{\partial K_{\phi\theta}}{\partial\phi}\right]\frac{\partial f}{\partial\theta} \\
& + \left[\frac{1}{r^2\sin\theta}\frac{\partial}{\partial r}(rK_{r\phi}) + \frac{1}{r^2\sin\theta}\frac{\partial K_{\theta\phi}}{\partial\theta} + \frac{1}{r^2\sin^2\theta}\frac{\partial K_{\phi\phi}}{\partial\phi} + \Omega\right]\frac{\partial f}{\partial\phi} \\
& + K_{rr}\frac{\partial^2 f}{\partial r^2} + \frac{K_{\theta\theta}}{r^2}\frac{\partial^2 f}{\partial\theta^2} + \frac{K_{\phi\phi}}{r^2\sin^2\theta}\frac{\partial^2 f}{\partial\phi^2} + \frac{2K_{r\phi}}{r\sin\theta}\frac{\partial^2 f}{\partial r\partial\phi} \\
& + \frac{1}{3r^2}\frac{\partial}{\partial r}(r^2 V)\frac{\partial f}{\partial\ln P} + Q,
\end{aligned} \tag{3.2}$$

with K_{rr}, $K_{r\theta}$, $K_{r\phi}$, $K_{\theta r}$, $K_{\theta\theta}$, $K_{\theta\phi}$, $K_{\phi r}$, $K_{\phi\theta}$, and $K_{\phi\phi}$ different elements of the diffusion tensor $\mathbf{K}$, Ω the angular speed of the Sun and V the solar wind speed. However, in this work a two-dimensional (2D) approach is assumed by assuming an azimuthal symmetry (i.e. $\frac{\partial}{\partial\phi} = 0$) in Equation 3.2. It is also assumed that there are no particle sources inside the heliosphere (i.e. $Q = 0$), and this 2D version of Equation 3.2 is solved numerically to calculate cosmic ray intensities inside the heliosphere [see e.g. le Roux, 1990, Ferreira, 2002, Manuel, 2012, for numerical aspects].

3.3 Diffusion Tensor

The symmetric diffusion tensor $\mathbf{K_S}$ in Equation 3.1 in an averaged background HMF aligned coordinate system is given as

$$\mathbf{K_S} = \begin{bmatrix} K_{||} & 0 & 0 \\ 0 & K_{\perp\theta} & 0 \\ 0 & 0 & K_{\perp r} \end{bmatrix}, \tag{3.3}$$

where $K_{||}$ is the diffusion coefficient parallel to the averaged HMF, $K_{\perp\theta}$ the diffusion coefficient perpendicular to the averaged HMF in the polar direction, and $K_{\perp r}$ the diffusion coefficient perpendicular to the averaged HMF in the radial direction.

The asymmetric drift tensor $\mathbf{K_A}$ can be written as

$$\mathbf{K_A} = \begin{bmatrix} 0 & 0 & 0 \\ 0 & 0 & K_A \\ 0 & -K_A & 0 \end{bmatrix}, \tag{3.4}$$

where K_A is the drift coefficient.

The full tensor $\mathbf{K}$ contains the diffusion and drift coefficients that determines the extent to which cosmic ray particles are transported and modulated, and this is given by

$$\begin{aligned} \mathbf{K} &= \mathbf{K_S} + \mathbf{K_A} \\ &= \begin{bmatrix} K_{||} & 0 & 0 \\ 0 & K_{\perp\theta} & K_A \\ 0 & -K_A & K_{\perp r} \end{bmatrix}. \end{aligned} \tag{3.5}$$

Using the full tensor as given by Equation 3.5 allows rewriting Equation 3.1 in a compact form as,

$$\frac{\partial f}{\partial t} = -\mathbf{V} \cdot \bigtriangledown f + \nabla \cdot (\mathbf{K} \cdot \bigtriangledown f) + \frac{1}{3} (\nabla \cdot \mathbf{V}) \frac{\partial f}{\partial \ln P} + Q, \tag{3.6}$$

where the averaged guiding center drift velocity is now contained in the asymmetrical part of the tensor. To transform to spherical coordinates, the HMF aligned coordinate system is related to the spherical coordinate system by the base vectors for the field aligned coordinates given as

$$\begin{aligned}\mathbf{e}_{||} &= \cos\psi\mathbf{e}_r - \sin\psi\mathbf{e}_\phi \\ \mathbf{e}_1 &= \mathbf{e}_\theta \\ \mathbf{e}_2 &= \sin\psi\mathbf{e}_r + \cos\psi\mathbf{e}_\phi,\end{aligned} \tag{3.7}$$

where $\mathbf{e}_{||}$ is the unit vector parallel to the averaged HMF, $\mathbf{e}_1$ the unit vector perpendicular to $\mathbf{e}_{||}$ in the polar direction and $\mathbf{e}_2$ the unit vector perpendicular to $\mathbf{e}_{||}$ in the radial direction. Also $\mathbf{e}_r$, $\mathbf{e}_\theta$ and $\mathbf{e}_\phi$ are the unit vectors in the spherical polar coordinate system and ψ is the spiral angle between $\mathbf{e}_r$ and $\mathbf{e}_{||}$. By specifying the appropriate transformation matrix $\mathbf{T}$, so that $\det(\mathbf{T}) = 1$, makes representation of diffusion tensor in spherical coordinates possible. This transformation matrix is given by

$$\mathbf{T} = \begin{bmatrix} \cos\psi & 0 & \sin\psi \\ 0 & 1 & 0 \\ -\sin\psi & 0 & \cos\psi \end{bmatrix}, \tag{3.8}$$

from which the diffusion tensor in Equation 3.5 in spherical coordinates is

$$\begin{aligned}\begin{bmatrix} K_{rr} & K_{r\theta} & K_{r\phi} \\ K_{\theta r} & K_{\theta\theta} & K_{\theta\phi} \\ K_{\phi r} & K_{\phi\theta} & K_{\phi\phi} \end{bmatrix} &= \mathbf{T}\mathbf{K}\mathbf{T}^T \\ &= \begin{bmatrix} \cos\psi & 0 & \sin\psi \\ 0 & 1 & 0 \\ -\sin\psi & 0 & \cos\psi \end{bmatrix} \begin{bmatrix} K_{||} & 0 & 0 \\ 0 & K_{\perp\theta} & K_A \\ 0 & -K_A & K_{\perp r} \end{bmatrix} \begin{bmatrix} \cos\psi & 0 & -\sin\psi \\ 0 & 1 & 0 \\ \sin\psi & 0 & \cos\psi \end{bmatrix} \\ &= \begin{bmatrix} K_{||}\cos^2\psi + K_{\perp r}\sin^2\psi & -K_A\sin\psi & (K_{\perp r} - K_{||})\cos\psi\sin\psi \\ K_A\sin\psi & K_{\perp\theta} & K_A\cos\psi \\ (K_{\perp r} - K_{||})\cos\psi\sin\psi & -K_A\cos\psi & K_{||}\sin^2\psi + K_{\perp r}\cos^2\psi \end{bmatrix}.\end{aligned} \tag{3.9}$$

In this work the diffusion coefficients of particular concern are diffusion coefficients in the radial (r) and polar (θ) direction, which can be written as

$$K_{rr} = K_{||} \cos^2 \psi + K_{\perp r} \sin^2 \psi$$
$$K_{\theta\theta} = K_{\perp\theta} \tag{3.10}$$
$$K_{\theta r} = K_A \sin \psi. \tag{3.11}$$

Equation 3.10 shows that K_{rr} has both the elements $K_{||}$ and $K_{\perp r}$. To determine which one of the two elements dominates K_{rr} in the inner heliosphere and which in the outer heliosphere, Figure 3.1 shows the values of $\sin^2 \psi$ and $\cos^2 \psi$ as a function of radial distance. Figure 3.1 shows for both polar and equatorial regions that the magnitude of $\cos^2 \psi$ decreases with increasing radial distance, while the magnitude of $\sin^2 \psi$ increases with radial distance before reaching a maximum value of 1 and then stays constant throughout the outer heliosphere. Note that Equations 3.7, 3.8, 3.9 and 3.10 are only valid for a Parker HMF.

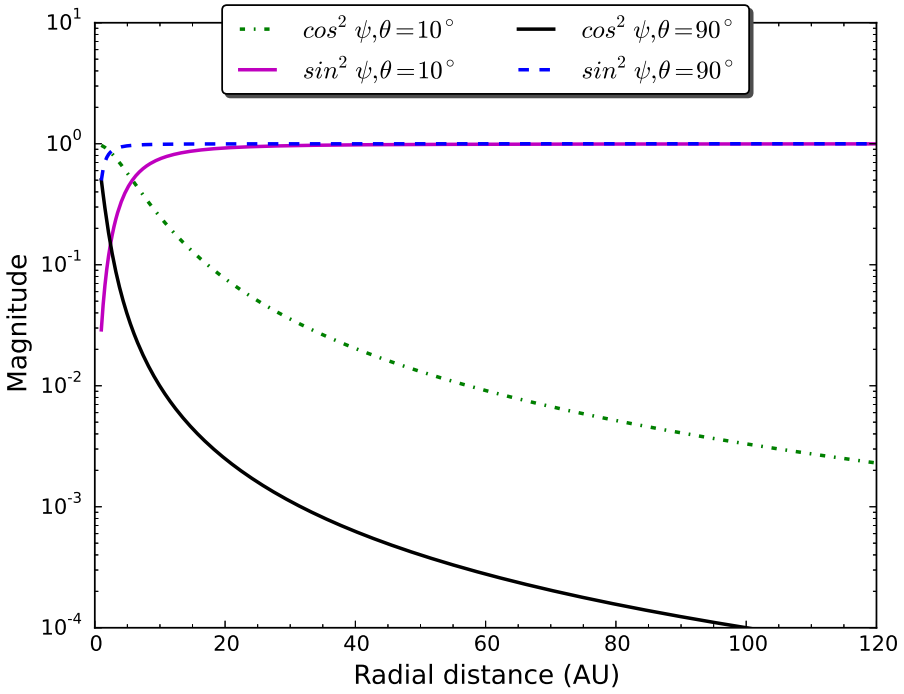

FIGURE 3.1: Magnitude of $\sin^2 \psi$ and $\cos^2 \psi$ in Equation 3.10 as a function of radial distance for polar angles $\theta = 10°$ and $\theta = 90°$.

In the inner heliosphere at the polar regions (e.g. $\theta = 10°$), the value of $\cos^2 \psi$ is larger than $\sin^2 \psi$, which results in $K_{||}$ dominating K_{rr} in the inner heliosphere and in the outer heliosphere the magnitude of $\sin^2 \psi$ is larger than $\cos^2 \psi$, which results in $K_{\perp r}$ dominating K_{rr} in the outer heliosphere. Also shown in the figure is the latitude dependence of $\sin^2 \psi$ and $\cos^2 \psi$, where at the equatorial region ($\theta = 90°$) $\cos^2 \psi$ decreases more rapidly than it does

near the polar regions ($\theta = 10°$), while $\sin^2\psi$ increases more rapidly in the equatorial region than near the polar region. See also Moeketsi [2004].

3.4 Parallel Diffusion

Fluctuations in the HMF result in cosmic ray particles undergoing diffusive propagation through pitch angle scattering. The pitch angle is the angle between the cosmic ray particle's velocity vector and the magnetic field direction. This process can be described by the weak turbulence quasi-linear theory (QLT) [e.g. Bieber and Matthaeus, 1991]. The parallel diffusion coefficient $K_{||}$ describes diffusion along the averaged HMF. Expression for $K_{||}$ can be given as

$$K_{||} = \frac{v\lambda_{||}}{3}, \tag{3.12}$$

with $\lambda_{||}$ the parallel mean free path and v the particle speed. According to QLT [e.g. Teufel and Schlickeiser, 2002], the pitch angle averaged parallel mean free path relates to the pitch angle Fokker-Plank coefficient $D_{\mu\mu}$ as

$$\lambda_{||} = \frac{3v}{8}\int_{-1}^{1}\frac{(1-\mu^2)^2}{D_{\mu\mu}(\mu)}d\mu, \tag{3.13}$$

with μ the cosine of the particle's pitch angle, which can be represented as $\mu = \frac{v_{||}}{v}$, where $v_{||}$ is a component of v parallel to the magnetic field direction.

The pitch angle Fokker-Plank coefficient $D_{\mu\mu}$ can be calculated from the power spectrum of the magnetic field fluctuations, an example of which is shown in Figure 3.2. From the figure it follows that the power spectrum can be divided into three distinct ranges: (1) the energy range - where the power spectrum variation is independent of the wavenumber k, (2) inertial range - where the power spectrum variation is proportional to $k^{-5/3}$ and (3) the dissipation range - where the power spectrum variation is proportional to k^{-3}. Shown also in the figure is the spectral break between the energy range and the inertial range represented by k_{min} and the spectral break between the inertial and dissipation range represented by k_d.

3.4.1 Rigidity Dependence

The parallel mean free path $\lambda_{||}$ following from Quasilinear theory (QLT) (given by Equation 3.13) was compared with the solar particle observations by Palmer [1982] and later by Bieber et al. [1994] who noticed it was much smaller than the observations for smaller rigidity values. Figure 3.3 shows this problem of a too small $\lambda_{||}$ predicted by QLT. The filled and

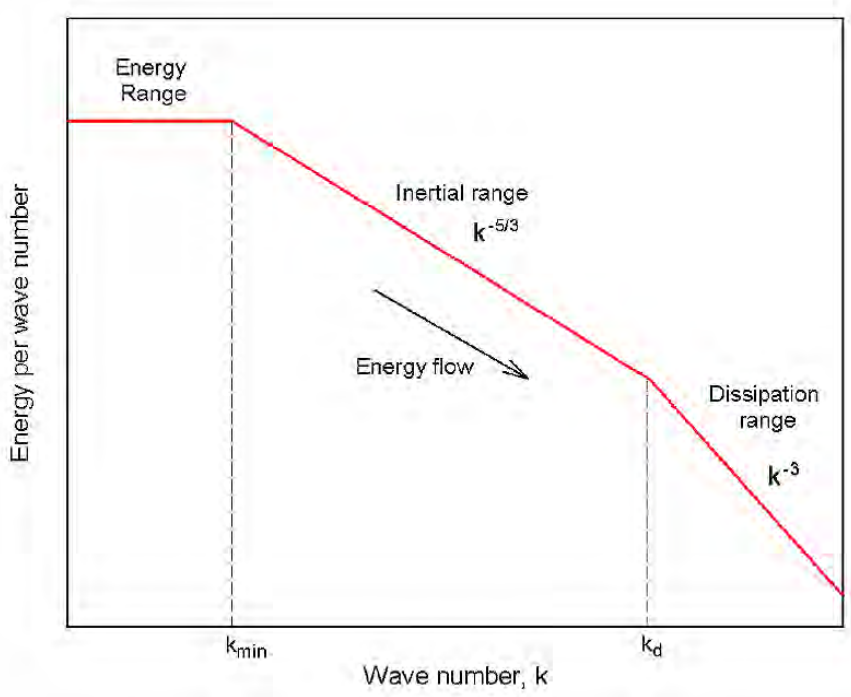

FIGURE 3.2: Graphical representation of a turbulence power spectrum [e.g. Teufel and Schlickeiser, 2003] divided into 3 regions, namely energy range, inertial range and dissipation range. From Manuel [2012].

open symbols represent results derived for electron and proton observations and the dotted line represent $\lambda_{||}$ predicted by QLT. Shown also is the shaded area representing the Palmer consensus values [Palmer, 1982].

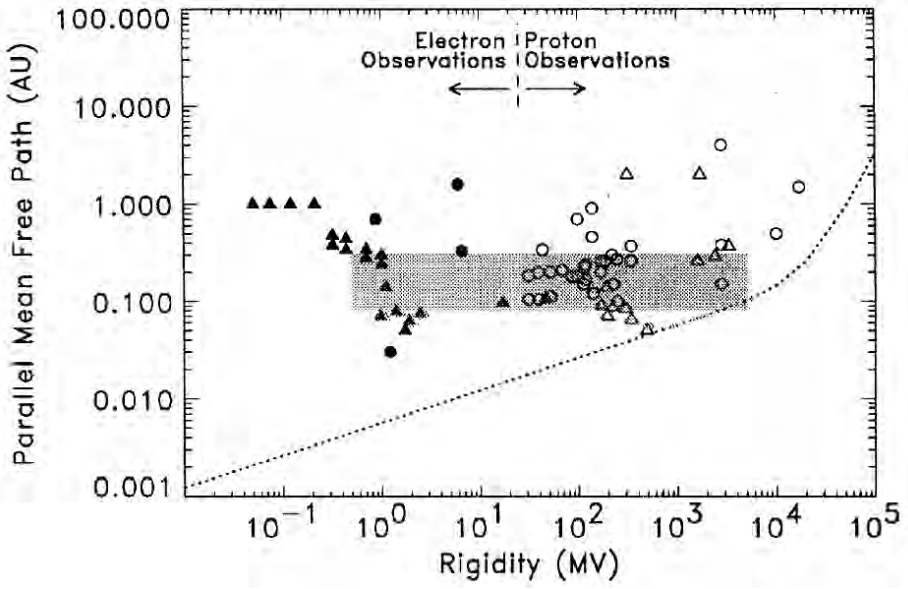

FIGURE 3.3: Parallel mean free path $\lambda_{||}$ as a function of rigidity. Shown also are results derived from electron and proton observations denoted by filled and open symbols respectively. The shaded area represents the observational consensus of Palmer [1982] and the dotted line represents $\lambda_{||}$ of the QLT. From Bieber et al. [1994].

Figure 3.3 shows that the theoretical $\lambda_{||}$ decrease with decreasing rigidities, even in the range 0.5 MV - 5000 MV, where the electron observations stayed constant, therefore implying no rigidity dependence for low-energy electrons. This problem was the result of neglecting the dissipation range of the power spectrum when calculating $\lambda_{||}$ [e.g. Bieber et al., 1994].

However, cosmic ray protons undergo significant adiabatic energy changes below $\sim$ 300 MeV and proton modulation at these low energies appears unaffected by $\lambda_{||}$ variations [see e.g. Potgieter, 1996, Potgieter and Ferreira, 1999, Ferreira, 2002]. Therefore, for low energy proton modulation in the heliosphere $\lambda_{||}$ derived without dissipation is applicable. However, this does not apply to cosmic ray electrons.

This work concentrated on high energy cosmic ray protons and made use of the $\lambda_{||} \propto P^{1/3}$ expression valid for 10^{-1} MV $\leq$ P $\leq 10^4$ MV proposed by Teufel and Schlickeiser [2002, 2003] at Earth. As assumed by Manuel [2012] the rigidity dependence is,

$$\lambda_{||} = C_1 \left(\frac{P}{P_0}\right)^{\frac{1}{3}}, \tag{3.14}$$

where C_1 is a constant in units of AU which determines the absolute value of the mean free path at Earth and $P_0 = 1$ MV.

3.4.2 Radial Dependence

This work used a $\lambda_{||}$ similar to that used by Burger et al. [2008], Engelbrecht [2008], Strauss et al. [2010] and Manuel [2012] for protons based on the work of Teufel and Schlickeiser [2003], given as

$$\lambda_{||} = \frac{3s}{\pi(s-1)} k_{min} R_L^2 \left(\frac{B}{\delta B_{slab,x}}\right)^2 \left(\frac{1}{4} + \frac{2(k_{min}R_L)^{-s}}{(2-s)(4-s)}\right), \tag{3.15}$$

where $s = 5/3$ is the spectral index of the inertial range derived by Kolmogorov, $R_L = \frac{P}{Bc}$ the Larmor radius and c the speed of light. The k_{min} is given by Engelbrecht [2008] as

$$k_{min} \propto \left(\frac{r}{r_0}\right)^{-0.4} \quad \text{m}^{-1}, \quad \text{for } r \leq r_{ts} \tag{3.16}$$

where r_0 =1AU and r_{ts} is the termination shock position, because it is not yet known how k_{min} scales in the heliosheath. See also Strauss et al. [2010].

The slab component of the magnetic field variance was assumed as [e.g. Burger et al., 2008, Strauss et al., 2010]

$$\delta B^2_{slab,x} = 13.2 \left(\frac{r_0}{r}\right)^{2.5} \quad \text{nT}^2, \quad \text{for } r < r_{ts}. \tag{3.17}$$

The slab component of variance is unclear in the heliosheath. It was therefore assumed to be given as $\delta B^2_{slab,x} \sim B^2$ in the heliosheath.

As shown by Strauss et al. [2010], Manuel et al. [2011*b*] and Manuel [2012], the radial dependence of Equation 3.15 can be approximated by a simple radial dependence given as

$$\lambda_{||} = \begin{cases} C_1 \left(\frac{P}{P_0}\right)^{\frac{1}{3}} \left(\frac{r}{r_0}\right)^{C_2}, & \text{for } r < r_{ts}, \\ \frac{C_1}{s_k} \left(\frac{P}{P_0}\right)^{\frac{1}{3}} \left(\frac{r}{r_0}\right)^{C_2} \left(\frac{r_{ts}}{r}\right), & \text{for } r \geq r_{ts} \end{cases} \tag{3.18}$$

where C_2 is a dimensionless constant that determines the radial dependence, C_1 a constant in units of AU that determines magnitude of $\lambda_{||}$ and s_k is the compression ratio.

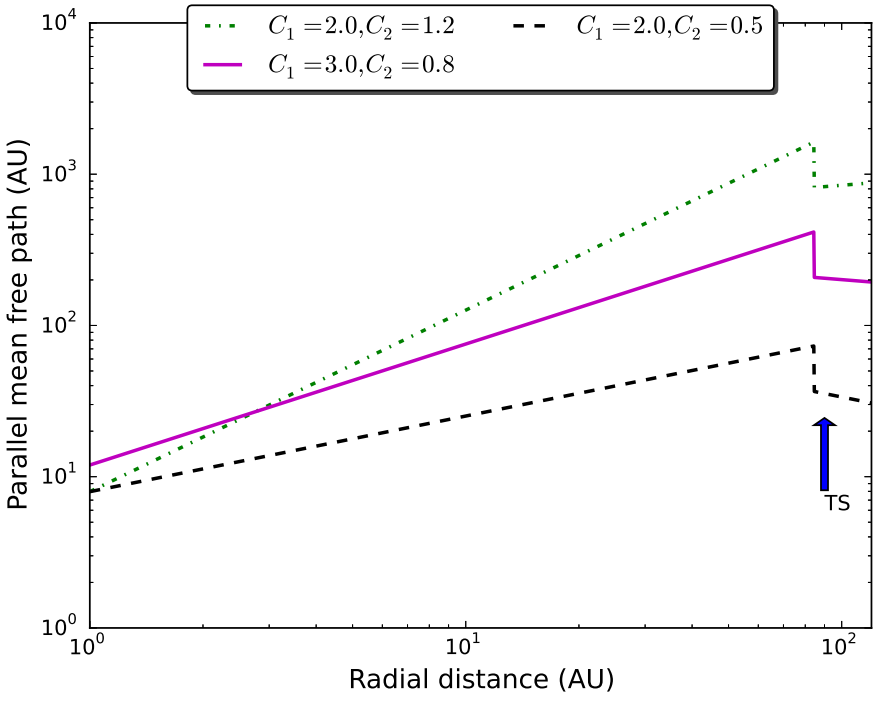

FIGURE 3.4: The parallel mean free path $\lambda_{||}$ as a function of radial distance for 2 GV protons in the equatorial plane. Three cases of $\lambda_{||}$ in Equation 3.18 are shown and the termination shock position is indicated by the blue arrow at 90 AU.

Figure 3.4 shows $\lambda_{||}$ as a function of radial distance for 2 GV protons in the equatorial plane. Three different scenarios are shown to illustrate the effects of different C_1 and C_2 values. Also shown is the position of the termination shock represented by a blue arrow and in this case at 90 AU. Beyond the termination shock $\lambda_{||}$ is decreased by a factor $s_k = 2$ [e.g. Richardson et al., 2008] and then decreases as r^{-1} [e.g. Manuel et al., 2011*b*] up to the heliopause.

3.5 Perpendicular Diffusion

The perpendicular diffusion coefficient $K_\perp$ describes diffusion of particles perpendicular to the averaged HMF. Displacement of particles' gyrocentres across the mean magnetic field due to fluctuations or random walk of the magnetic field lines results in the perpendicular scattering of particles [e.g. Jokipii, 1966, Minnie et al., 2009]. QLT by Jokipii [1966] assumes a slab turbulence geometry. Following this theory which describes perpendicular transport of particles via the Field Line Random Walk (FLRW) limit, it has been shown by simulations [e.g. Qin et al., 2002, Minnie et al., 2009] that QLT is not adequate for the description of perpendicular transport of particles, especially for lower energies.

However, Matthaeus et al. [2003] developed a NonLinear Guiding Centre (NLGC) theory, which describes diffusion in non-slab models. Even so, for slab turbulence, the NLGC results disagree with the numerical solutions [See e.g. Shalchi, 2009, for a review]. For this study, a more simpler approach on perpendicular diffusion was followed and that was a first order approach which assumed $K_\perp \propto K_{||}$ [see e.g. Potgieter and Haasbroek, 1993, le Roux et al., 1996, Giacalone and Jokipii, 1999, Burger et al., 2000, Qin et al., 2002]. Also, observations from the Ulysses spacecraft revealed that the latitude dependence of cosmic ray protons is less than predicted by drift dominated models [e.g. Potgieter and Haasbroek, 1993]. Kóta and Jokipii [1995] subsequently proposed the concept of an anisotropic $K_\perp$. This was studied in detail by Potgieter et al. [1997] and Ferreira et al. [2000]. They showed that assuming $K_{\perp\theta} > K_{\perp r}$, leads to a significant decrease in drifts and compute more realistic intensities compatible with observations.

In this work it was assumed that

$$K_{\perp r} = aK_{||}, \tag{3.19}$$

and

$$K_{\perp\theta} = bK_{||}, \tag{3.20}$$

where a and b are either dimensionless constants or functions of rigidity [e.g. Burger et al., 2000, Ferreira, 2002, Ndiitwani et al., 2005, Manuel et al., 2011*a*]. Enhanced latitudinal transport suggested by Burger et al. [2000] was used in this work in order to reproduce the observed Ulysses cosmic ray intensity gradients. This was done whereby

$$K_{\perp\theta} = bF(\theta)K_{||}, \tag{3.21}$$

the function $F(\theta)$ enhances $K_{\perp\theta}$ by some value d towards the pole. This function was suggested by Burger et al. [2000], and is given by

$$F(\theta) = A^{+} \mp A^{-} \tanh\left[\frac{1}{\Delta\theta}(\tilde{\theta} - 90^{\circ} \pm \theta_F)\right], \tag{3.22}$$

where $A^{\pm} = \frac{d\pm1}{2}$, $\Delta\theta = 1/8$, $\tilde{\theta} = \theta$ and $\theta_F = 35^{\circ}$ for $\theta \leq 90^{\circ}$ while for $\theta > 90^{\circ}$, $\tilde{\theta} = 180^{\circ} - \theta$ and $\theta_F = -35^{\circ}$.

3.6 Implementation of Drift Effects in the Model

As already mentioned, cosmic ray particles undergo drifts due to physical phenomena such as gradients in the magnetic field, curvature of the field line, or any sudden changes in the field direction like when HMF changes polarity across the HCS. However, the significance of drifts were initially neglected in early modulation model studies until Jokipii et al. [1977] and Potgieter and Moraal [1985] pointed out its significance to modulation.

$$\begin{aligned}
\frac{\partial f}{\partial t} = &\left[\frac{1}{r^2}\frac{\partial}{\partial r}(r^2 K_{rr}) + \frac{1}{r\sin\theta}\frac{\partial K_{\phi r}}{\partial \phi}\right]\frac{\partial f}{\partial r} + \left[\frac{1}{r^2\sin\theta}\frac{\partial}{\partial\theta}(K_{\theta\theta}\sin\theta)\right]\frac{\partial f}{\partial\theta} \\
&+ \left[\frac{1}{r^2\sin\theta}\frac{\partial}{\partial r}(rK_{r\phi}) + \frac{1}{r^2\sin^2\theta}\frac{\partial K_{\phi\phi}}{\partial\phi} + \Omega\right]\frac{\partial f}{\partial\phi} \\
&+ K_{rr}\frac{\partial^2 f}{\partial r^2} + \frac{K_{\theta\theta}}{r^2}\frac{\partial^2 f}{\partial\theta^2} + \frac{K_{\phi\phi}}{r^2\sin^2\theta}\frac{\partial^2 f}{\partial\phi^2} + \frac{2K_{r\phi}}{r\sin\theta}\frac{\partial^2 f}{\partial r\partial\phi} \\
&+ [- < \mathbf{v}_d >_r]\frac{\partial f}{\partial r} + \left[-\frac{1}{r} < \mathbf{v}_d >_\theta\right]\frac{\partial f}{\partial\theta} + \left[-\frac{1}{r\sin\theta} < \mathbf{v}_d >_\phi\right]\frac{\partial f}{\partial\phi} \\
&+ -V\frac{\partial f}{\partial r} \\
&+ \frac{1}{3r^2}\frac{\partial}{\partial r}(r^2 V)\frac{\partial f}{\partial \ln P} \\
&+ Q
\end{aligned} \tag{3.23}$$

Equation 3.2 which is the TPE in a 3D heliocentric, spherical coordinate system can be rewritten as Equation 3.23 to highlight the different drift velocities and different modulation processes, i.e. the coloured part defines: magenta - describes particle diffusion, blue - particle drift effects, green - convection, cyan - adiabatic energy changes and red - is the source term. The components of the gradient, curvature and current sheet drifts can be written as

$$
\begin{aligned}
< \mathbf{v}_d >_r &= -\frac{\tilde{A}}{r\sin\theta}\frac{\partial}{\partial\theta}(K_{\theta r}\sin\theta)\mathbf{e}_r \\
< \mathbf{v}_d >_\theta &= -\frac{\tilde{A}}{r}\left(\frac{\partial}{\partial r}(rK_{r\theta}) + \frac{1}{\sin\theta}\frac{\partial}{\partial\phi}(K_{\phi\theta})\right)\mathbf{e}_\theta, \\
< \mathbf{v}_d >_\phi &= -\frac{\tilde{A}}{r}\frac{\partial}{\partial\theta}(K_{\theta\phi})\mathbf{e}_\phi
\end{aligned}
$$

where

$$
\tilde{A} = \begin{cases} +1, & \text{for } qA > 0, \\ -1, & \text{for } qA < 0. \end{cases} \tag{3.24}
$$

Here q is the charge of the particle and $A = \pm 1$ is a constant denoting HMF polarity which is positive when HMF is directed away from the Sun and negative when HMF is pointing towards the Sun in the northern hemisphere of the Sun.

The average drift velocity of a nearly isotropic particle distribution is given as

$$
< \mathbf{v}_d >= \nabla \times K_A \mathbf{e}_B, \tag{3.25}
$$

where $\mathbf{e}_B = \mathbf{B}/B$ is a unit vector in the direction of the magnetic field $\mathbf{B}$ and K_A is a drift coefficient. In the Parker HMF it follows that the average drift velocity [e.g. see Hattingh, 1998, Ferreira, 2002] in Equation 3.25 can be written as

$$
< \mathbf{v}_d >= \nabla \times K_A \mathbf{e}_B(1 - 2H(\theta - \acute{\theta})) + 2\delta_d(\theta - \acute{\theta})K_A\mathbf{e}_B \times \nabla(\theta - \acute{\theta}), \tag{3.26}
$$

where H is the Heaviside step function already defined by Equation 2.6, θ is the polar angle, $\acute{\theta}$ is the polar angle that describes the position of the current sheet HCS [e.g. Jokipii and Thomas, 1981] and the Dirac function δ_d is defined as

$$
\delta_d(\theta - \acute{\theta}) = \begin{cases} 0 & \text{for } \theta \neq \acute{\theta} \\ \infty & \text{for } \theta = \acute{\theta}. \end{cases} \tag{3.27}
$$

The first term of Equation 3.26 represents curvature and gradient drifts due to the Parker HMF and the second term represents the drifts due to HCS.

However, this work used the Wavy Current Sheet (WCS) model [see e.g Hattingh and Burger, 1995b, Burger and Hattingh, 1995, Hattingh, 1998] to simulate HCS in a 2D time-dependent

modulation model. A two-dimensional drift velocity from the WCS model is obtainable by averaging Equation 3.26 over one solar rotation, i.e. for azimuthal angle ranging from $\phi = 0$ to 2π, which results in

$$< \mathbf{v}_d >= g(\theta)\nabla \times K_A \frac{\mathbf{B}}{B} + \frac{2Prv\Gamma}{3cA\pi(1+\Gamma^2)\left((\alpha+\Delta\theta_{ns})^2 + \left(\frac{\pi}{2}-\theta\right)^2\right)^{1/2}}\mathbf{e}_r. \tag{3.28}$$

This expression is however divergence free and difficult to handle numerically and for this reason an approximation which is nearly divergence free is derived by these authors instead and is given as

$$< \mathbf{v}_d >\approx g(\theta)\nabla \times K_A \frac{\mathbf{B}}{B} + \frac{Prv\acute{\Gamma}}{3cA(1+\acute{\Gamma}^2)(\alpha+\Delta\theta_{ns})}\mathbf{e}_r, \tag{3.29}$$

where

$$g(\theta) = \begin{cases} 1 & \text{for } 0 \leq \theta \leq \frac{\pi}{2} - \alpha - \Delta\theta_{ns}, \\ \frac{2}{\pi}\sin^{-1}\left(\frac{\frac{\pi}{2}-\theta}{\alpha+\Delta\theta_{ns}}\right) & \text{for } \frac{\pi}{2} - \alpha - \Delta\theta_{ns} < \theta < \frac{\pi}{2} + \alpha + \Delta\theta_{ns}, \\ -1 & \text{for } \frac{\pi}{2} + \alpha + \Delta\theta_{ns} \leq \theta \leq \pi \end{cases} \tag{3.30}$$

where α is the tilt angle, v the particle speed, P the rigidity, $\Delta\theta_{ns} = \frac{2R_L}{r}$ the angle spanned by two gyroradii, with $R_L = \frac{P}{Bc}$ the Larmor radius, r the radial distance from the Sun, c the speed of light, $\Gamma = \tan\psi$, with ψ the spiral angle, $\acute{\Gamma} = \frac{\Omega(r-r_\odot)}{V}\cos\left(\frac{\alpha}{\sqrt{2}}\right)$, V the magnitude of the radial solar wind velocity and $r_\odot$ the radius of the Sun.

It follows that Equation 3.29 consists of the term that represents curvature and gradient drifts $< \mathbf{v}_d^* >$ and the term representing HCS drifts $< \mathbf{v}_d^{ns} >$, so that

$$< \mathbf{v}_d^* >= g(\theta)\nabla \times K_A \frac{\mathbf{B}}{B}, \tag{3.31}$$

and

$$< \mathbf{v}_d^{ns} >= \frac{Prv\acute{\Gamma}}{3cA(1+\acute{\Gamma}^2)(\alpha+\Delta\theta_{ns})}\mathbf{e}_r. \tag{3.32}$$

The function $g(\theta)$ scales the curvature and gradient drifts down over the HCS region. However, outside the current sheet regions HCS drift is zero. The HCS region is the region swept out by particles drifting along the HCS during one solar rotation, as per definition, which makes the simulation of the effect of HCS by the WCS model possible.

The comparison of the approximation of the 3D with a 2D model for galactic cosmic ray electrons in the heliosphere was done by Ferreira et al. [1999] to establish the reliability of the 2D model and the extent they can be applied to modulation studies.

Figure 3.5 shows computed electron spectra calculated by the 2D and 3D drift models with the outer boundary of the simulated heliosphere assumed at 100 AU. The differential intensities are shown for 1 AU and 60 AU at a polar angle of $\theta = 30°$ (left panel) for A > 0 and for polar angle of $\theta = 90°$ (right panel). Note that for A > 0 cycle electrons drift in along the HCS.

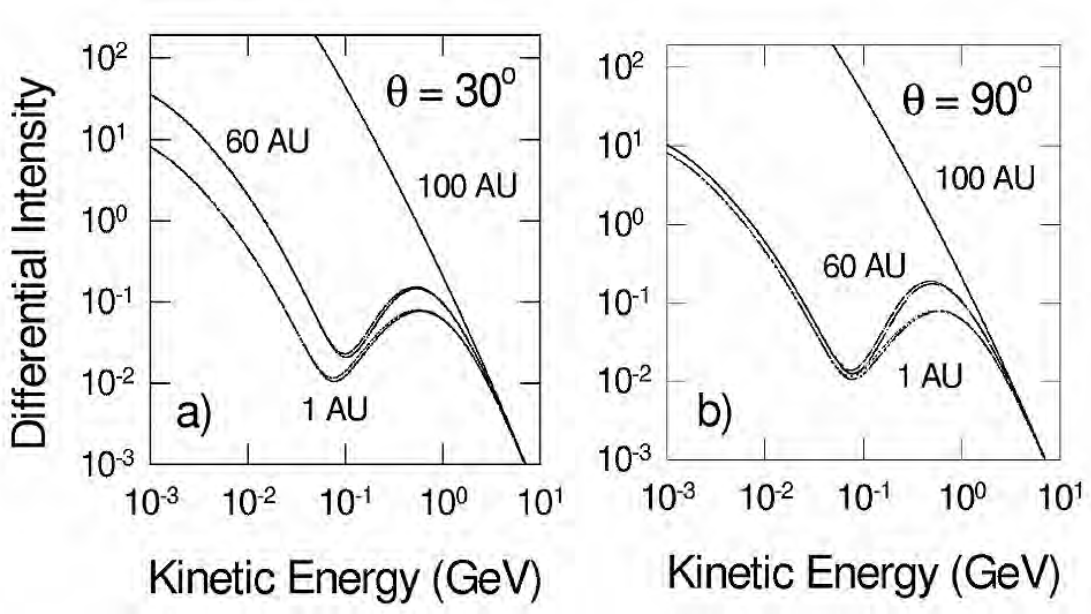

FIGURE 3.5: Computed electron spectra using the 2D and 3D drift model. The left panel shows differential intensities at 1 AU and 60 AU at polar angle of $\theta = 30°$ and the right panel at polar angle of $\theta = 90°$. In both instances the tilt angle is 20° in units of $m^{-2}sr^{-1}s^{-1}MeV^{-1}$ and for A > 0 HMF polarity cycle. From Ferreira et al. [1999].

From the figure it follows that the two models computed electron spectra which largely coincide. Not much difference is visible on this scale. However, at kinetic energy between ~ 0.1 - 0.5 GeV, the two models on both panels show a notable difference with one model computing intensities slightly higher than the other. Because HCS is not treated the same for 2D as it is for 3D model, Ferreira et al. [1999] compared the two models by examining the α dependence of the differential intensities.

Figure 3.6 shows the computed ratio of the results of the 2D and 3D differential intensities as a function of α for both the A > 0 and A < 0 HMF polarity cycles. The top panel shows for 1.94 GeV electrons: a) computed values at 1 AU, b) computed values at 60 AU and the bottom panel shows for 0.30 GeV electrons: c) computed values at 1 AU, d) computed values at 60 AU.

It follows from the figure that for 1.94 GeV electrons at both 1 AU and 60 AU for both polarity cycles, the variation of the ratio of the two models from unity is significantly small for all α

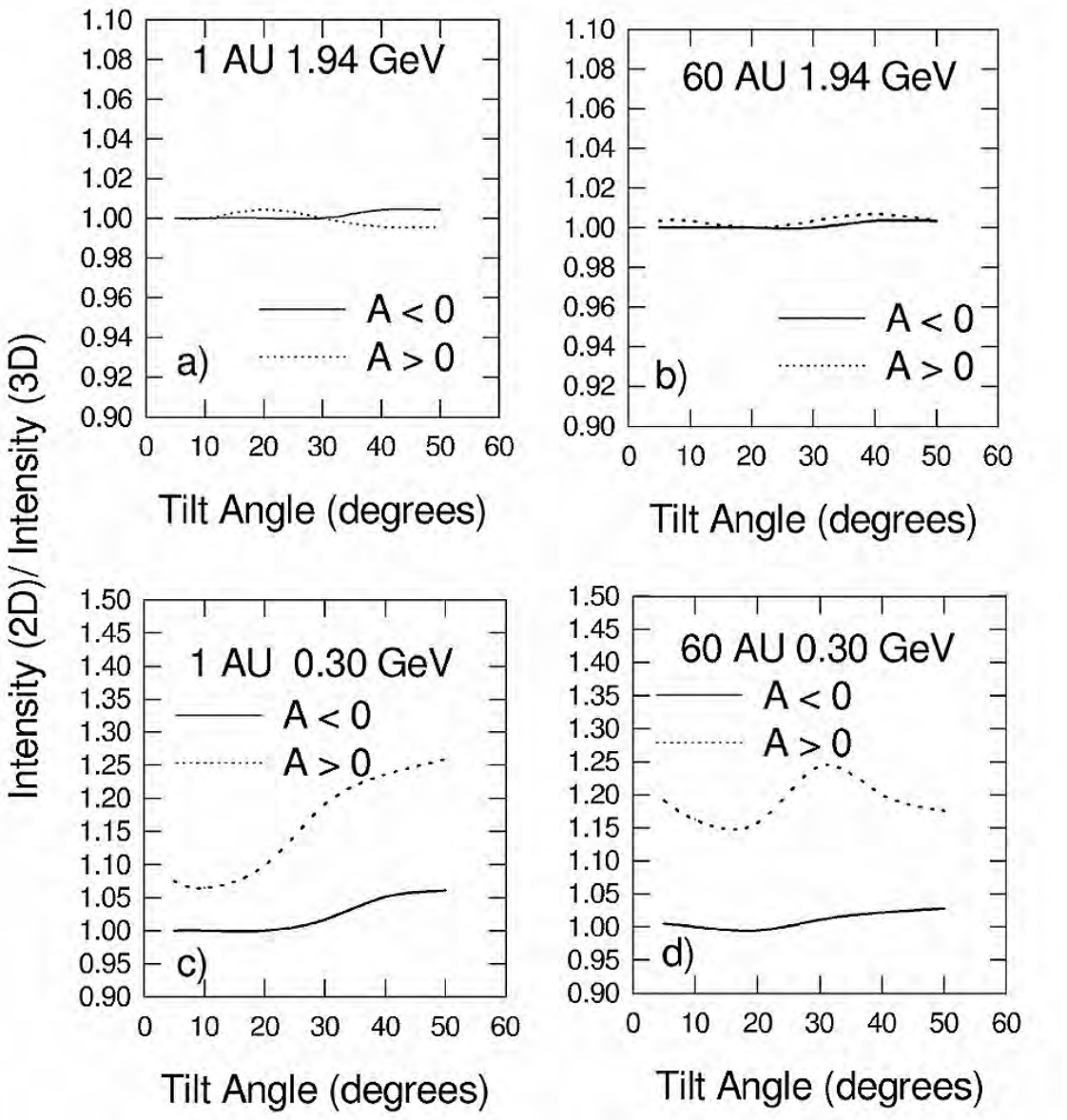

FIGURE 3.6: The ratio of the electron differential intensities computed with the 2D and 3D drift models as a function of tilt angle for both A > 0 and A < 0 HMF polarity cycles. Panel a) shows ratio for 1.94 GeV electrons at 1 AU, b) ratio for 1.94 GeV electrons at 60 AU, c) ratio for 0.30 GeV electrons at 1 AU, d) ratio for 0.30 GeV electrons at 60 AU. From Ferreira et al. [1999].

values shown. At 0.30 GeV, for the A < 0 polarity cycle the deviation from unity is small for $\alpha <\sim 30°$, but significantly large for A > 0 polarity cycle, but still less than 25%.

Ferreira et al. [1999] found no qualitative differences between 2D and 3D model solutions. Quantitative differences were insignificant either and as a result the use of the 2D drift model in modulation studies was well justified, especially in this work which concentrated on energies around 2.5 GV.

Recently Raath et al. [2015] studied modulation effects of the wavy HCS towards increased solar activity. The numerical modulation model employed by these authors uses an approach

based on stochastic differential equations which is different from the modified compound approach followed in this work. This approach allows for trajectories of pseudo-particles to be followed. These authors constructed two scenarios that investigate how the geometry of the wavy HCS can affect the modulation of cosmic rays. The two scenarios are given by the expressions,

$$\acute{\theta} = \frac{\pi}{2} + \arcsin\left[\sin\ \alpha\ \sin\left(\phi + \frac{\Omega(r - r_{\odot})}{V}\right)\right], \tag{3.33}$$

given by Jokipii and Thomas [1981] and

$$\acute{\theta} = \frac{\pi}{2} - \arctan\left[\tan\ \alpha\ \sin\left(\phi + \frac{\Omega(r - r_{\odot})}{V}\right)\right], \tag{3.34}$$

given by Kóta and Jokipii [1983]. Note that Equation 3.34 is the correct expression for the HCS while Equation 3.33 is only valid for small tilt angles such that $\tan a \sim \sin a$. The HCS profile resulting from Equations 3.33 and 3.34 is shown in Figure 3.7. These profiles are compared in the meridional plane for different α values.

It follows from Figure 3.7 that small α values, e.g. $\alpha = 5°$ and $\alpha = 35°$, do not yield clear geometrical differences between the two profiles. However, for large α values, e.g. $\alpha = 85°$, the geometrical differences between the two profiles become clear. HCS profile by Equation 3.33 appears to be more sharp compared to profile following Equation 3.34, which is notably broader and more rounded.

Figure 3.8 shows the effects of the two HCS profiles, shown in Figure 3.7, on 1.0 GeV protons during both A $>$ 0 and A $<$ 0 polarity cycles at Earth. The scenario named $\mathrm{HCS_{arctan}}$ (red line) refers to the case using HCS profile from Equation 3.34 and the $\mathrm{HCS_{arcsin}}$ (blue line) refers to the case using HCS profile from Equation 3.33. Shown also for comparison is a zero-drift scenario.

Figure 3.8 shows that during an A $>$ 0 cycle $\mathrm{HCS_{arctan}}$ and $\mathrm{HCS_{arcsin}}$ result in almost same intensities up to $\alpha \simeq 6°$. For increasing α values up to $\sim 72°$, $\mathrm{HCS_{arcsin}}$ result in intensities below $\mathrm{HCS_{arctan}}$ and then $\mathrm{HCS_{arctan}}$ continues to rapidly decrease up to the solution of the zero-drift at $\alpha = 90°$. But $\mathrm{HCS_{arcsin}}$ solution is seen to result in a flat profile at $\sim 75°$.

On the other hand, solutions for A $<$ 0 shows that $\mathrm{HCS_{arctan}}$ and $\mathrm{HCS_{arcsin}}$ result in almost the same intensities up to $\alpha \simeq 10°$, then $\mathrm{HCS_{arctan}}$ fall below $\mathrm{HCS_{arcsin}}$ till $\alpha \simeq 80°$. Both $\mathrm{HCS_{arctan}}$ and $\mathrm{HCS_{arcsin}}$ fall below zero-drift solution at $\alpha \sim 35°$ and $\alpha \sim 43°$, respectively.

The notable decrease in both A $>$ 0 and A $<$ 0 solutions with increasing solar activity is due to an increasing waviness of the HCS, which acts against protons from reaching Earth. From a geometrical perspective as outlined in Figure 3.7 for A $>$ 0, it follows that protons of a

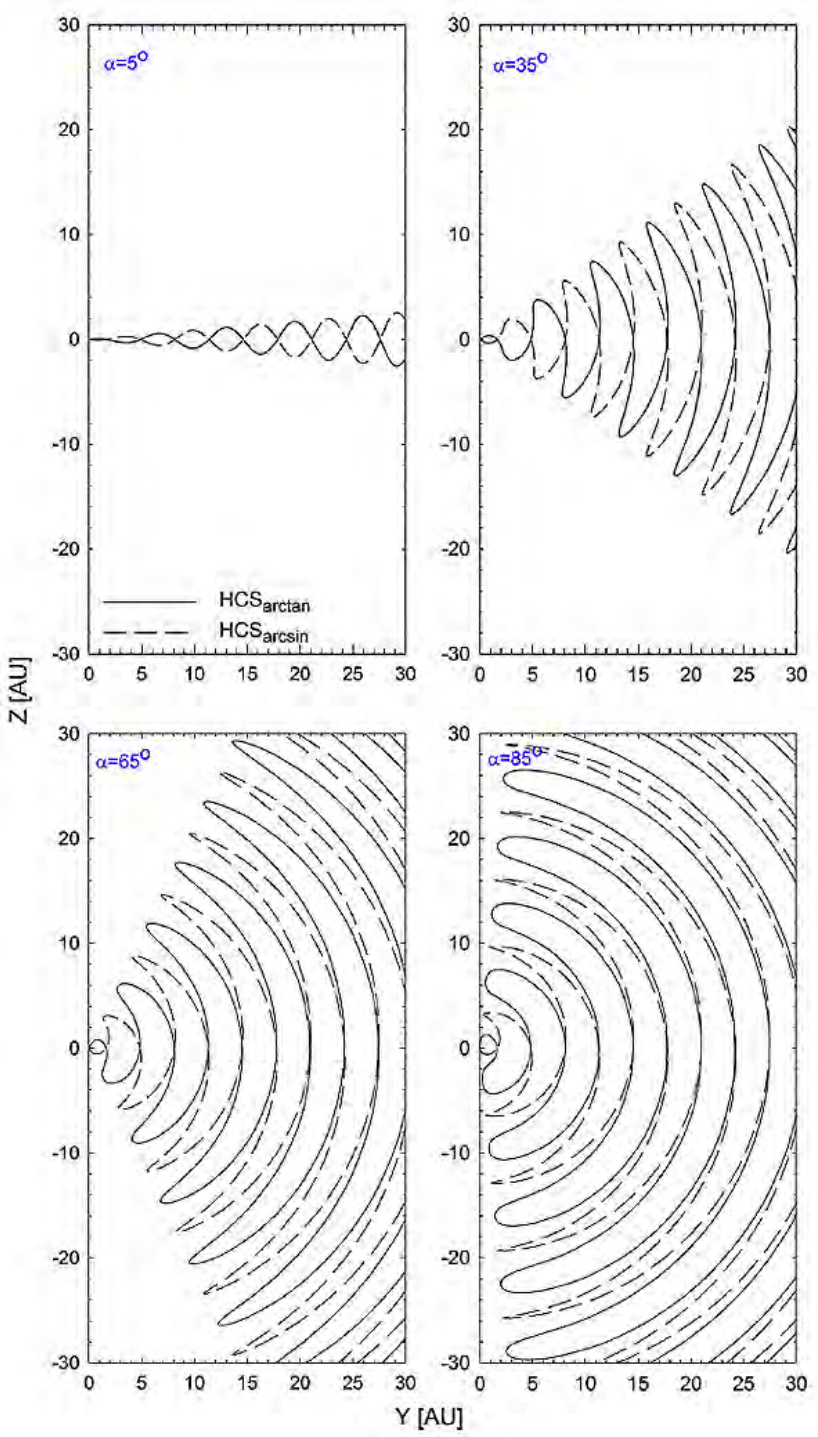

FIGURE 3.7: HCS profiles given by Equations 3.33 (shown by dashed line) and 3.34 (shown by solid line), compared for different α values as indicated and shown in the meridional plane. Note that the two profiles are plotted out-of-phase for illustrative purposes. From Raath et al. [2015].

given energy will easily short-circuit the narrow arms of $\mathrm{HCS_{arcsin}}$ profile, therefore reaching Earth more frequently and resulting in higher intensities at Earth towards increased solar activity. The reverse is true for the $\mathrm{HCS_{arctan}}$ profile with broader arms. For $A < 0$ cycle, $\mathrm{HCS_{arctan}}$ profile results in less protons drifting out over the polar regions, thus resulting in

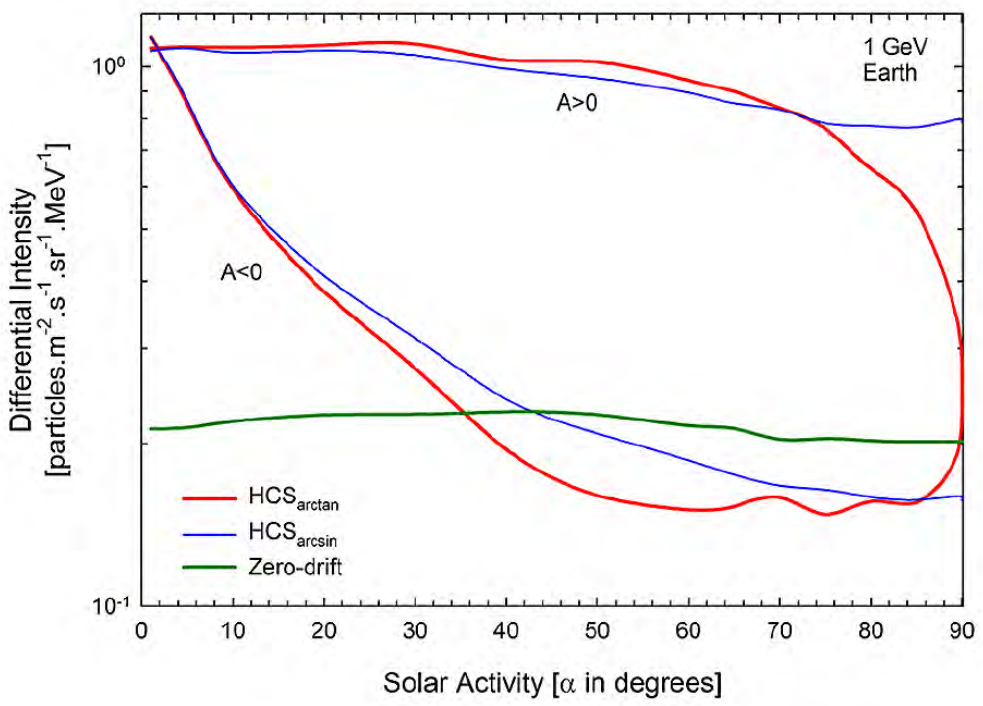

FIGURE 3.8: Intensities of 1 GeV protons at Earth during both A $>$ 0 and A $<$ 0 cycles, comparing results of HCS_{arcsin} and HCS_{arctan} profiles. Shown also is the zero-drift solution. From Raath et al. [2015].

higher intensities than HCS_{arcsin} towards increased solar activity.

Due to a certain HCS geometry affecting cosmic ray modulation differently than the other geometry, it is therefore necessary to make use of an effective tilt angle α_e as proposed by le Roux and Potgieter [1992]. It is expected that, at a fixed α, large enough for the geometrical differences between HCS_{arcsin} and HCS_{arctan} profiles to be significant, proton encountering HCS_{arcsin} profile will react to a tilt angle $\alpha_e < \alpha$. It follows that α_e for HCS_{arctan} profile is larger than for HCS_{arcsin} profile. Later in Chapter 7 the tilt angle values are modified and the effects of such a modification on calculated intensities are discussed.

3.7 The Effects of Drifts on the Global Distribution of Cosmic Rays

Because particle drifts and its dependence on magnetic field polarity are so important in understanding the cosmic ray distribution in the heliosphere, this section focuses on giving a brief overview on the global cosmic ray distribution during different polarity cycles.

An illustration of cosmic ray drift trajectories is shown in Figure 3.9. This figure shows a meridional projection of the different drift velocity directions for 2.0 GeV protons during an $A > 0$ magnetic polarity cycle. It follows that for this polarity cycle, positively charged

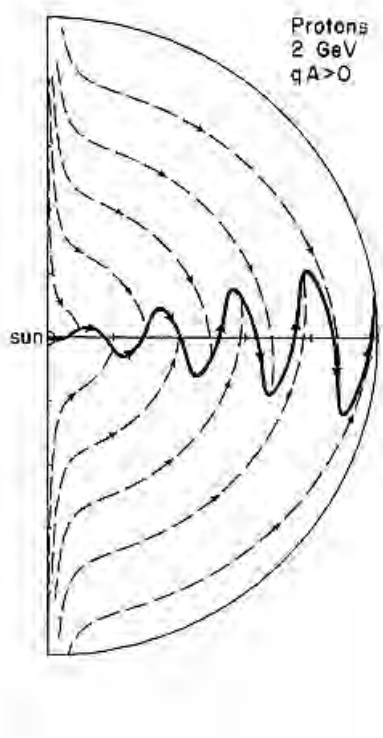

FIGURE 3.9: Meridional projection of drift trajectories for 2 GeV protons during a $A > 0$ HMF polarity cycle. For negatively charged particles or for a $A < 0$ HMF polarity cycle the arrows will point in the opposite direction. From Jokipii and Thomas [1981].

particles drift into the heliosphere from the polar regions down the equatorial regions and exit through along the HCS. The thick wavy curve represents the drift along the HCS. However, during an $A < 0$ magnetic polarity cycle (not shown here) positively charged particles drift inward along the HCS and exit through the polar regions.

Strauss et al. [2012] showed the effects of heliospheric current sheet drift on cosmic rays using a stochastic cosmic ray transport model. Of particular interest from their work is the cosmic ray distribution in the meridional plane of the heliosphere for different HMF polarities. Their results are shown in Figures 3.10. The top and middle panels of Figure 3.10 show pseudo-particle traces (trajectories) for cosmic ray protons during A < 0 cycle for different α values (as indicated in the figure). The bottom panel shows results for A > 0 cycle. These figures demonstrate the effectiveness of cosmic ray drifts into the inner heliosphere for different HMF polarity cycles. The dotted lines represent the projection of the HCS on the meridional plane.

It is clearly visible from the top and middle panels of Figure 3.10 that, during A < 0 cycle, particle trajectories into the inner heliosphere are largely within the latitudinal extent of HCS. Also of importance to notice in these figures is that, for small α values, e.g. $\alpha = 10°$, there's a high tendency for particles to follow HCS wavy pattern. For larger α values, e.g. $\alpha = 75°$, drift patterns are highly altered by diffusion. This is an important result to keep in mind for

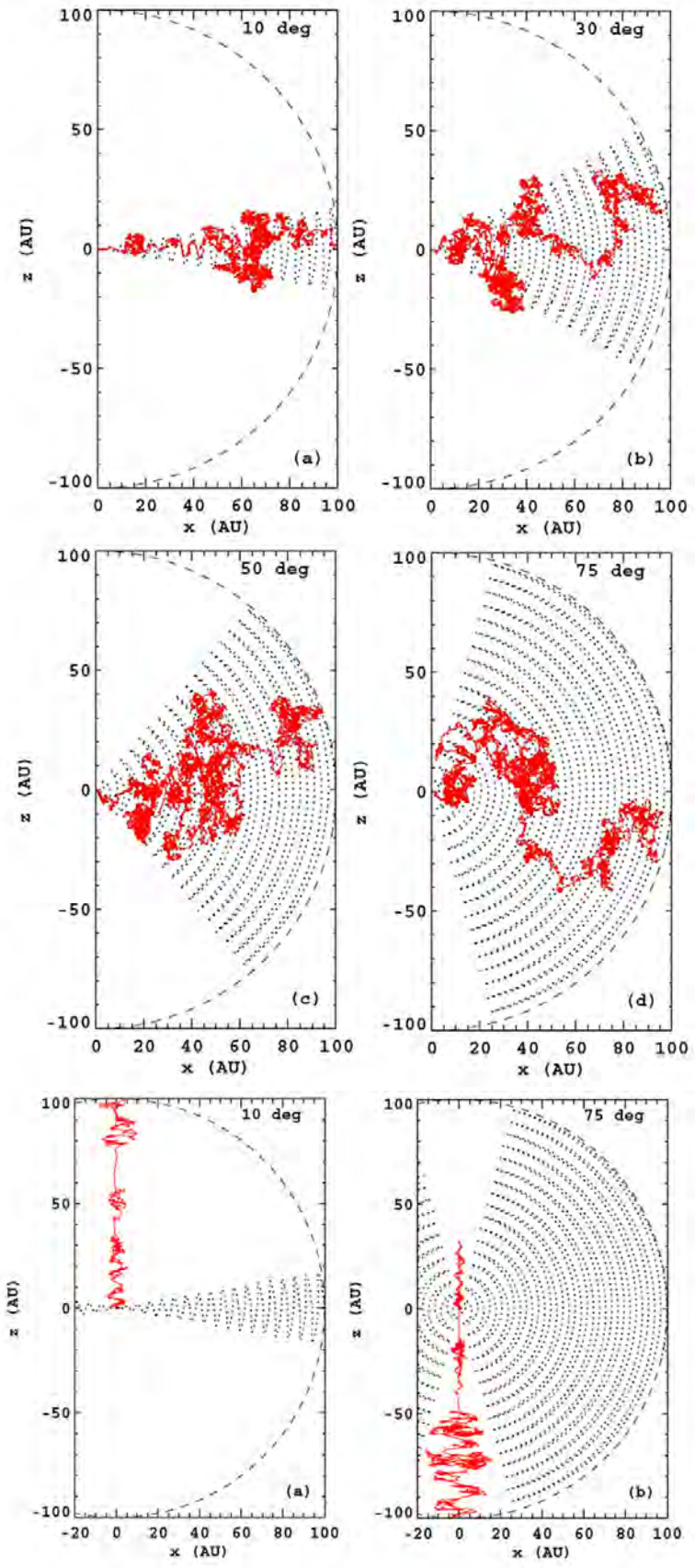

FIGURE 3.10: Pseudo-particle trajectories for galactic protons for E = 100 MeV, projected onto the meridional plane of the heliosphere. Calculations are shown for different α values as indicated. The top and middle panels show results for A < 0 cycle and the bottom panel for A > 0 cycle. Particle trajectories are shown in red and the heliopause position is shown by dashed line. The dotted line shows a projection of the HCS. From Strauss et al. [2012].

the following chapters. The bottom panel of the figure shows the results for the A $>$ 0 cycle. Here cosmic ray protons drift inward through the polar regions without sampling the HCS, with an exception for the extreme case where α reaches its maximum value. Similar behaviour can be seen from recent calculations done by Prinsloo [2016]. Note that the approaches by Prinsloo [2016] and Ngobeni [2015] included acceleration of cosmic rays at the termination shock.

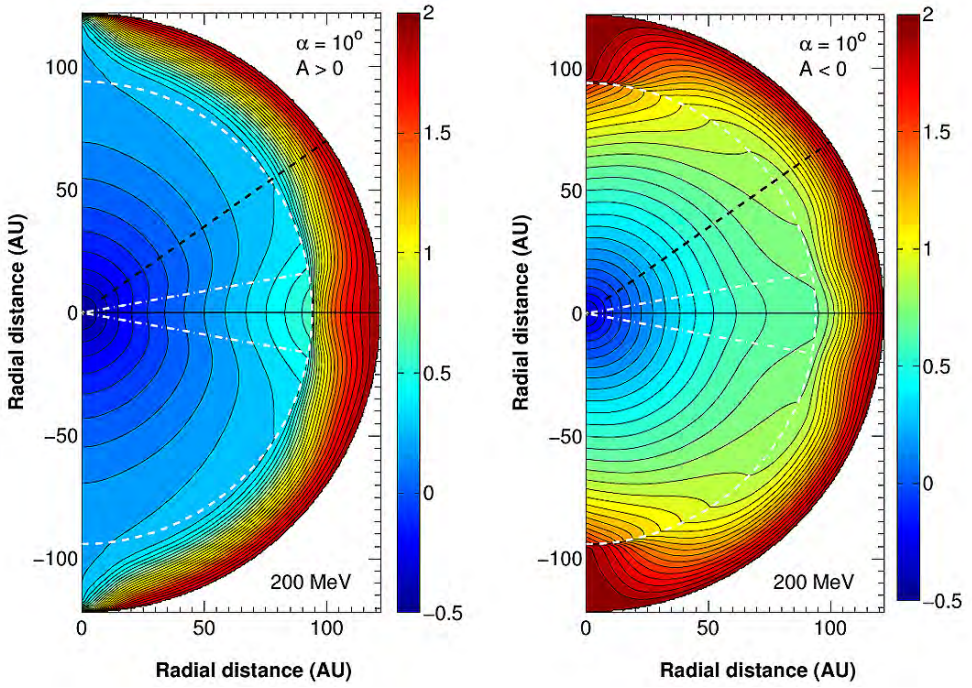

FIGURE 3.11: Contour plots showing 200 MeV galactic electron intensities, calculated in the meridional plane of the heliosphere for $\alpha = 10$ deg as indicated, with the left panel showing results for A $>$ 0 cycle and the right panel for A $<$ 0 cycle. Shown also by a dashed white halfcircle is the termination shock position at 94 AU, the dash-dotted white lines indicate the latitudinal extent of the HCS and the dashed black line the Voyager 1 trajectory along $\theta = 55°$. From Prinsloo [2016].

Figure 3.11 shows the spatial distribution of 200 MeV galactic electron intensities in the meridional plane of the heliosphere for different HMF polarity cycles. Shown also by a dashed white half-circle is the termination shock position at 94 AU, the dash-dotted white lines indicate the latitudinal extent of the HCS and the dashed black line the Voyager 1 trajectory along $\theta = 55°$. Recall that the electron drift pattern is expected to be the opposite of the drift pattern displayed by protons, i.e., during A $<$ 0 polarity cycle electrons drift outward along HCS and downward along the poles toward the equatorial regions in the heliospheric interior and the directions are reversed during A $>$ 0 polarity cycle. These drift patterns are illustrated in Figure 3.11 [from Prinsloo, 2016], with contours assuming a convex shape in the direction electrons are travelling, hence during A $>$ 0 cycle increased intensities around the equatorial region and during A $<$ 0 cycle increased intensities around the polar regions of the heliosphere, therefore confirming the electron's drift pattern as expected to be so.

Another recent study came from Ngobeni [2015], see also Ngobeni and Potgieter [2015], who investigated the drift reduction in the heliosphere by using the knowledge about the spatial and rigidity dependence of the scattering parameter ($\omega\tau$), where ω is gyro-frequency and τ represents some time scale defined by scattering. Based on the assumption of weak scattering with $\omega\tau \gg 1.0$, the generalized drift coefficient is given as

$$K_T = f_s \frac{\beta P}{3B}, \tag{3.35}$$

where f_s is the drift reduction due to diffusive scattering. See for example the work of Giacalone et al. [1999], Minnie et al. [2007] and Tautz and Shalchi [2012] showing by direct numerical simulations the suppression of particle drift motions by diffusive scattering. Note in the equation above that when $f_s = 0$ drift velocities vanish and when $f_s = 1.0$ drift velocities reach maximal under the assumption of the weak scattering. The expression for f_s is given by Bieber and Matthaeus [1997] as

$$f_s = \frac{(\omega\tau)^2}{1 + (\omega\tau)^2}, \tag{3.36}$$

where ω is the gyro-frequency and τ some time scale defined by scattering. Substituting Equation 3.35 into Equation 3.25 results in

$$< \mathbf{v}_d >= \frac{\beta P}{3} \left[f_s \nabla \times \frac{\mathbf{B}}{B^2} + \bigtriangledown f_s \times \frac{\mathbf{B}}{B^2} \right], \tag{3.37}$$

which is the averaged drift velocity caused by gradient and curvature in the HMF.

It follows from Equation 3.37 that when f_s is constant, i.e. no spatial dependence in $\omega\tau$, then $\bigtriangledown f_s = 0$, which results in reduction of drift velocity due to the effect of particle scattering by a factor f_s, which translates to the spatial dependence of the HMF resulting as the only drive of the gradient and curvature drifts. But in the case where $\omega\tau$ has a spatial dependence and $\bigtriangledown f_s \neq 0$, then the second term on the right hand side of Equation 3.37 will have a significant contribution to the drift coefficient.

Ngobeni [2015] looked at four different scenarios of $\omega\tau$ and f_s based on the work by Burger et al. [2000], Burger and Visser [2010] and Engelbrecht and Burger [2013]. See Ngobeni [2015] and references therein for more details and mathematical descriptions of the equations used for these four scenarios. For the four scenarios, B2000 refers to the work from Burger et al. [2000], BV2010 from Burger and Visser [2010], and EB2013 from Engelbrecht and Burger [2013]. Note also that for the B2000 scenario, there is drift reduction but $\bigtriangledown f_s = 0$ and for the other scenarios BV2010 and EB2013 there is drift reduction and $\bigtriangledown f_s \neq 0$. Note that λ_A is the drift scale which can be expressed as

$$\lambda_A = \frac{3}{v} K_T, \tag{3.38}$$

where λ_A uses values of $\omega\tau$ and f_s.

Figure 3.12 shows the effects of different drift reduction scenarios on the galactic cosmic ray carbon intensities in the equatorial plane of the heliosphere at radial distances of 1 AU, 60 AU and 110 AU. Note that red lines represent calculated spectra for A $>$ 0 polarity cycle and black lines for A $<$ 0 polarity cycle during solar minimum conditions.

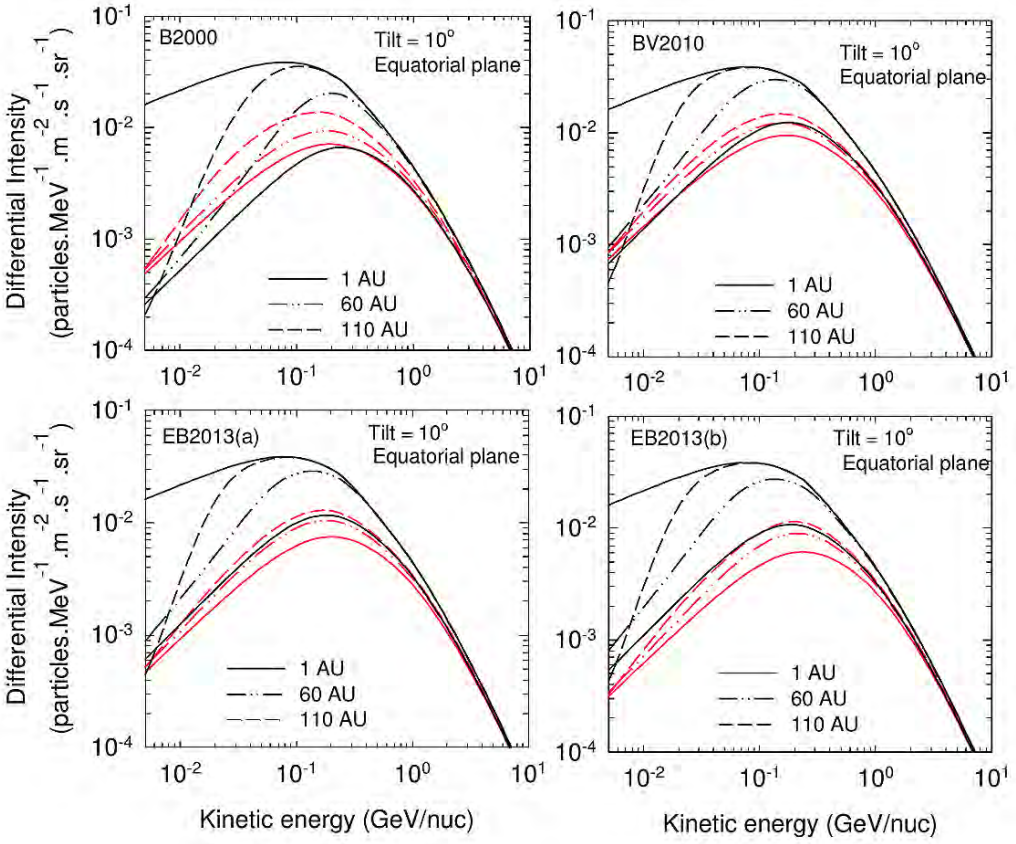

FIGURE 3.12: The computed galactic cosmic ray carbon differential intensities as a function of kinetic energy/nuc in the equatorial plane at radial distances 1 AU, 60 AU and 110 AU during solar minimum. The four scenarios computed follows from the four scenarios of λ_A with B2000 representing solutions when $\omega\tau$ from Burger et al. [2000] is used, BV2010 when $\omega\tau$ from Burger and Visser [2010] is used and EB2013(a) and EB2013(b) from Engelbrecht and Burger [2013]. From Ngobeni [2015].

It follows from Figure 3.12 that λ_A values based on the work of Burger et al. [2000] and Burger and Visser [2010] result in the expected drift effects at Earth as shown in the top panel of this figure, with spectra computed during the A $>$ 0 cycle crossing that of the A $<$ 0 cycle at low energies. The other scenarios, i.e. EB2013(a) and EB2013(b) in the bottom panel, result in unexpected drift effects in the equatorial plane when $\omega\tau$ decreases from large values in the equatorial region to very small values in the polar region. Under these conditions the

computed intensities for A < 0 cycle become larger than for A > 0 cycle at all energies in the equatorial plane.

Under the assumption of the weak scattering approach, the drift coefficient K_A given by the standard approach [see e.g. Burger and Potgieter, 1989] is,

$$K_A = K_{A0}\frac{\beta P}{3B}, \tag{3.39}$$

with $\beta = v/c$, where v is the particle's speed, c the speed of light, B is the modified HMF magnitude [e.g. Jokipii and Kóta, 1989] where the mean field magnitude is increased in the heliospheric polar regions compared to the pure Parker type field and K_{A0} is a dimensionless constant that scales K_A and ranges between 0 and 1.

However, this work used the modified approach of the drift coefficient from Burger et al. [2000, 2008] which is given by

$$K_A = K_{A0}\frac{\beta P}{3B}\frac{\left(\frac{P}{P^*}\right)^2}{\left[\left(\frac{P}{P^*}\right)^2 + 1\right]} \tag{3.40}$$

where $P^* = \frac{1}{\sqrt{10}}$ GV. The modified approach for $P < 600$ MV is steeper compared to the weak scattering approach. A justification for this modified approach is based on calculations of the rigidity dependence for proton latitudinal gradients and comparisons with Ulysses observations [Burger et al., 2000]. Also, this choice of modification is consistent with numerical simulations of Giacalone et al. [1999] and Minnie et al. [2007], but also with the observational results of Lockwood and Webber [1992].

3.8 Summary

The distribution of the cosmic rays in the heliosphere is the result of the four different major transport processes, i.e., drifts due to the gradient and curvature of the heliospheric magnetic field or any abrupt changes in the direction of the magnetic field in the current sheet, diffusion due to fluctuations in the heliospheric magnetic field that result in particles undergoing diffusive propagation, convection by the solar wind propagating radially outwards from the Sun and the adiabatic energy changes due to the solar wind velocity expanding or compressing. These four major modulation processes are contained in the Parker [1965] transport equation.

The diffusion tensor $\mathbf{K}$ in a HMF aligned coordinate system was shown to comprise of the symmetric diffusion tensor, $\mathbf{K_S}$, which describes cosmic ray diffusion along ($K_{||}$, the parallel diffusion coefficient) and perpendicular ($K_{\perp\theta}$, the perpendicular diffusion coefficient in the

polar direction, and $K_{\perp r}$, the perpendicular diffusion coefficient in radial direction) to the averaged HMF. The asymmetric drift tensor, $\mathbf{K_A}$, which contains the drift coefficient K_A, describes cosmic ray drift motions due to gradient and curvature of HMF and the current sheet drifts.

The parallel diffusion coefficient $K_{||}$ used in this work is based on the work of Teufel and Schlickeiser [2002, 2003]. The rigidity dependence of $K_{||}$ for protons at 1 AU as proposed by these authors and as assumed by Manuel et al. [2014], was given by Equation 3.14. The radial dependence used in this work was approximated by Strauss et al. [2010], Manuel et al. [2011*b*] and Manuel [2012] to a simple radial dependence given by Equation 3.18. At the termination shock position, r_{ts}, all diffusion coefficients are decreased by a factor $s_k = 2$ and then further decreases as r^{-1} in the modulation model.

It is assumed that the perpendicular diffusion coefficient scales spatially as the parallel diffusion coefficient, $K_\perp \propto K_{||}$. An anisotropic $K_\perp$, i.e. $K_{\perp\theta} > K_{\perp r}$, was also assumed in order to attain more realistic computation of the latitudinal gradients of cosmic ray intensities. An enhancement given by Equation 3.22, was also assumed.

Cosmic ray particles in the heliosphere experience gradient, curvature and current sheet drift motions as well. In the 2D time-dependent modulation model utilized in this work, the HCS is simulated based on the Wavy Current Sheet (WCS) model. The modified approach of the drift coefficient given by Equation 3.40 is used as well. This modification results in K_A decreasing much faster for $P < 600$ MV as a function of decreasing rigidity than does the weak-scattering approach.

Because drift effects are important in understanding the rest of this work, a brief overview of recent work done by Strauss et al. [2012], Ngobeni [2015] and Prinsloo [2016] was given. These authors showed the distribution of cosmic rays in the heliosphere and the dependence on the drift coefficient.

Chapter 4

Time-dependent modulation

4.1 Introduction

As discussed in previous chapters, cosmic rays in the heliosphere are modulated by the outblowing turbulent solar wind and the embedded HMF which carries with it different heliospheric conditions that change over a solar cycle. This chapter gives a brief overview of time-dependent cosmic ray modulation concentrating on authors who used different numerical modulation models to compute cosmic ray intensities and who compared results with observations. The Global Merged Interaction Region (GMIR)-Drift approach of le Roux and Potgieter [1995], the compound approach of Ferreira and Potgieter [2004] and Ndiitwani et al. [2005] as well as the application of this approach by Magidimisha [2011] are discussed. The more recent modified compound approach of Manuel [2012] and Manuel et al. [2014] is discussed with the aim to improve on this approach in later chapters.

4.2 Propagating Diffusion Barriers

Embedded in the 11-year solar cycle and 22-year drift cycle (discussed in Chapter 2), are the large step decreases in observed cosmic ray intensities, especially during increasing solar activity. These observed step decreases are a result of propagating diffusion barriers [Perko and Fisk, 1983, le Roux and Potgieter, 1989]. They form due to solar wind and magnetic field co-rotating structures interacting. The fast and slow solar wind streams interact with each other forming interaction regions when the fast solar wind runs into slow solar wind stream and compressing it [Burlaga et al., 1985]. Because the magnetic field is frozen-in in the solar wind, it is also enhanced at the interaction region.

When observed over two consecutive solar rotations, these interaction regions become corotating interaction regions (CIRs) [Burlaga, 1984, Burlaga and Ness, 1998]. From $\sim$ 10 AU the

CIRs spread and merge and form merged interaction regions (MIRs) [e.g. le Roux, 1999], with intense magnetic fields that modulates cosmic ray intensities. A relation between the magnetic field strength and changes in cosmic ray intensities beyond $\sim$ 10 AU was observed by Burlaga et al. [1985]. Using Voyager 1 and 2 observations, these authors found that cosmic ray intensity increases in rarefactions (where magnetic field is relatively weak) and decreases in interaction regions (where magnetic field is stronger), resulting in step-increases and step-decreases.

Beyond $\sim$ 10 AU, MIRs are grouped into 3 categories, i.e., Local MIRs (LMIRs), Corotating MIRs (CMIRs), and Global MIRs (GMIRs) [e.g. McDonald and Burlaga, 1997]. LMIRs have limited azimuthal and longitudinal extent and result in cosmic ray intensities changing only locally [McDonald and Burlaga, 1997]. CMIRs have a spiral shape extending to few AUs and result in recurrent decrease in cosmic ray intensities. However, they do not result in long-term cosmic ray modulation [le Roux, 1999].

Beyond $\sim$ 20 AU, MIRs merge and become GMIRs, extending all the way around the Sun and reaching to at least 30° in heliographic latitude [Burlaga et al., 1993]. GMIRs are large-scale interaction regions with a shell-like geometry that lasts for several solar rotations. They act as barriers to the incoming cosmic rays and produce step-like decreases in cosmic ray intensities [e.g. le Roux and Potgieter, 1995].

4.3 GMIR-Drift Approach

le Roux and Potgieter [1990] studied long-term cosmic ray modulation with a time-dependent drift model. These authors simulated a wavy current sheet which evolved with time and changes in the waviness of the current sheet were propagated radially outward at the solar wind speed in their model.

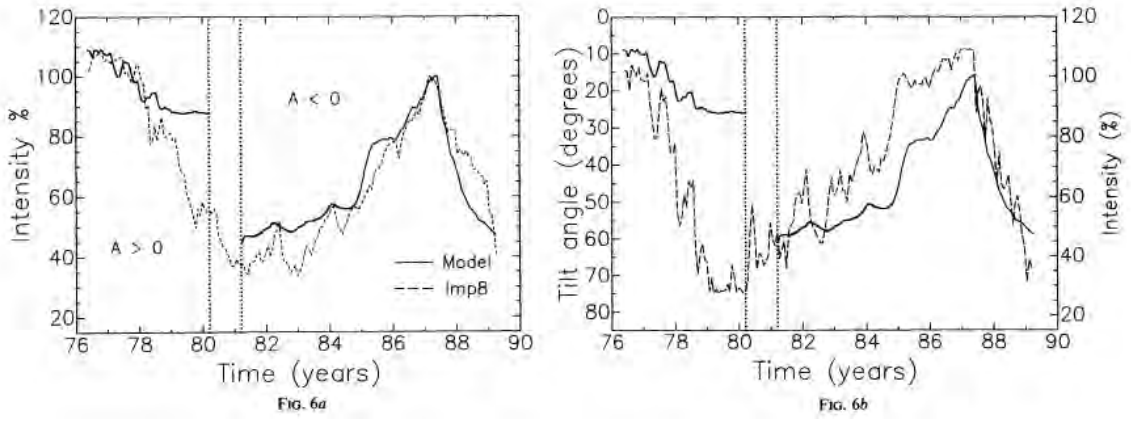

Figure 4.1: Calculated cosmic ray intensities (solid line) as a function of time using a time-dependent drift model. Shown also are the IMP 8 observations on the left panel and the HCS tilt values at Earth on the right panel. The vertical lines indicate the period of polarity reversal. From le Roux and Potgieter [1990].

With the tilt angle, α, as the only assumed time-dependent parameter, le Roux and Potgieter [1990] showed that this approach is only compatible to long-term modulation during low solar activity periods as shown in Figure 4.1. This figure shows that for $A > 0$ polarity cycle during increased solar activity the calculated cosmic ray intensities do not respond much to changes in α. This is because of cosmic rays drifting inward from the polar regions and therefore not sensitive to changes in α. The model of le Roux and Potgieter [1990] showed better compatibility when compared to observations just after $\sim$ 1981 for $A < 0$ polarity during solar maximum. However the observed modulation amplitude between solar minimum and solar maximum could not be realistically computed. These results showed that modulation models with waviness of the HCS as the only time-dependent parameter cannot reproduce cosmic ray observations for increasing solar activity, especially when large step decreases are observed. See also le Roux and Potgieter [1995] and le Roux [1999].

One example of these series of step decreases in cosmic ray intensities is shown in Figure 4.2. Shown here are 26-day averaged 130-225 MeV proton intensities by IMP 8 and Pioneer 10 from 1977 to 1983. Emphasised are the step-decreases represented by roman numerals I, II, III and IV [Fujii and McDonald, 1995]. These step decreases are prominent during moderate to high solar activity when changes in the HCS are less important to cosmic ray modulation.

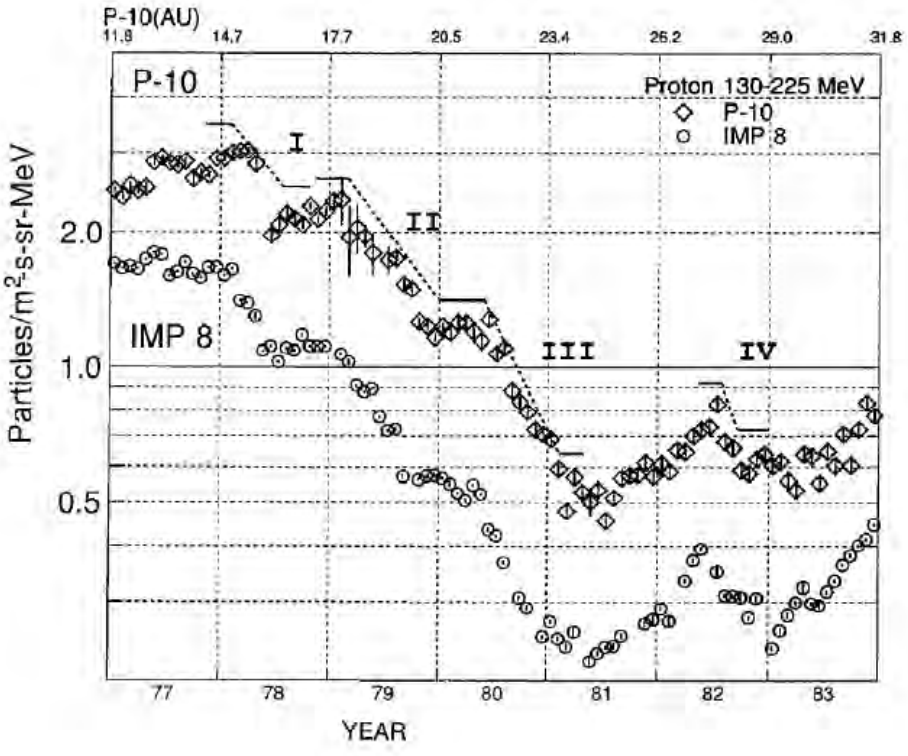

FIGURE 4.2: The 26 day averaged 130-225 MeV proton intensities from IMP 8 and Pioneer 10. Shown by the roman numerals are the four step decreases in cosmic ray intensities. From Fujii and McDonald [1995].

Perko and Fisk [1983] proposed that, in order to model long-term cosmic ray modulation, one need some form of propagating diffusive barrier (e.g. GMIRs as proposed by Burlaga

et al. [1993]), especially for moderate to high solar activity periods (e.g. when $\alpha > 30°$). To integrate propagating diffusion barriers into a 2D time-dependent drift model, le Roux and Potgieter [1995] modelled regions of enhanced magnetic field which moved outward with the solar wind. In this drift-GMIR approach the diffusion tensor is inversely proportional to the time-dependent HMF. The assumption is that a passage of a GMIR causes temporal change of diffusion from the background values and in return reduces the diffusion coefficient. The GMIR is therefore a partial barrier for cosmic rays diffusing and drifting into the heliosphere. These authors did simulations for radial distances larger than 20 AU which allows enough time for the formation of a GMIR.

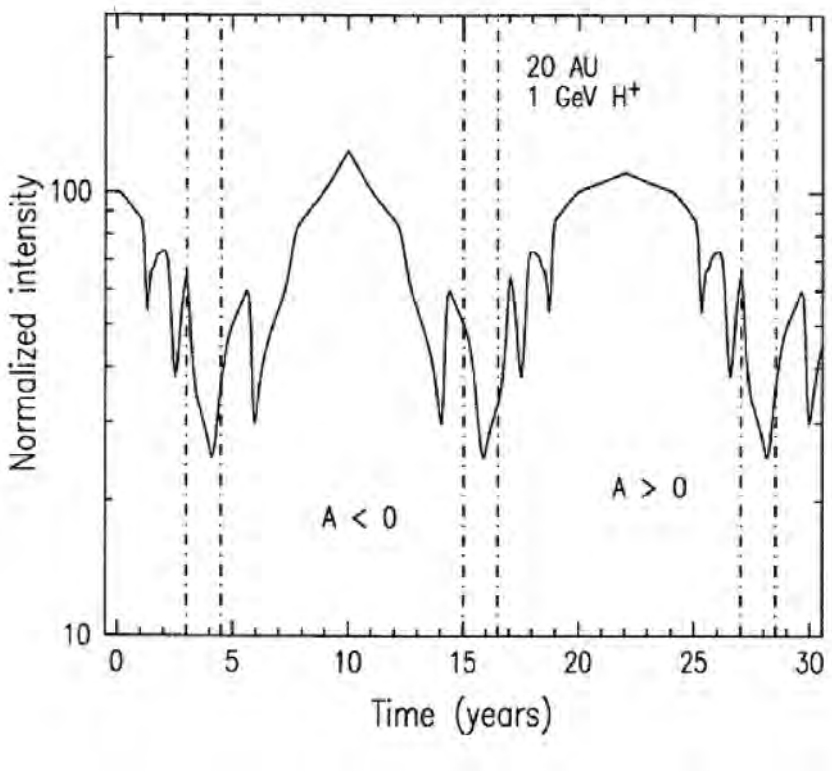

FIGURE 4.3: The simulated 22 year cosmic ray modulation cycle using a 2D time-dependent GMIR-Drift model by le Roux and Potgieter [1995]. The vertical dashed lines shows period of the HMF polarity reversal. From le Roux and Potgieter [1995].

As shown in Figure 4.3, le Roux and Potgieter [1995] successfully simulated to first order a complete 11 and 22 year cosmic ray modulation cycle. The peak- and plateau-like intensity profiles shown in the figure during $A < 0$ and $A > 0$ polarity cycles are due to particle drift effects. Also calculated are the step decreases and increases in intensities which are due to propagating GMIRs. These authors concluded that the inclusion of GMIRs in the drift model resulted in a computed long-term modulation profile which is compatible to observations.

4.4 Compound Approach

Cane et al. [1999] and Wibberenz et al. [2002] argued that the cosmic ray step decreases observed at Earth could not solely be due to GMIRs. They argued from observations that these decreases occurred already at 1 AU before the formation of GMIRs. They suggested in addition that time-dependent global changes in the HMF were also responsible. le Roux and Fichtner [1999] also studied the time-dependent cosmic ray modulation including GMIRs in their model. They found that the cosmic ray step decreases caused by GMIRs could not alone explain long-term cosmic ray modulation and that in addition, long-term changes in the diffusion coefficients were also needed.

This concept was tested by Ferreira [2002] and Ferreira and Potgieter [2004] by introducing a time-dependence for all transport parameters through a function

$$f(t) = \left(\frac{B_0}{B\,(t)} \right)^n , \tag{4.1}$$

where n is a constant, $B_0 = 5$ nT, the magnitude of the averaged measured HMF at Earth during solar minimum and $B(t)$ the time-dependent HMF measured at Earth. These time-dependent changes in the transport parameters are then propagated outward in the model at the solar wind speed. Choosing $n = 1$ in Equation 4.1 resulted in their model resembling the observed 11 year cosmic ray modulation cycle by neutron monitors at Earth, as shown in Figure 4.4. This figure shows the normalised 16 GV computed cosmic ray intensities using Equation 4.1. As shown, the model resulted in intensities which are compatible with the neutron monitor observations. Computed step decreases/increases which are shown in Figure 4.4 were reproduced without including GMIRs directly in the model.

Ferreira and Potgieter [2004] also computed intensities at lower energies compared to Figure 4.4. Shown in Figure 4.5 are the computed 1.2 GV electron intensities at Earth for different values of n as in Equation 4.1. The computed intensities are compared to the ISEE/ICE and Ulysses/KET observations. The figure shows that for $n = 0$, the model failed to produce compatibility with observations for intermediate to increasing solar activity conditions. For this value of n the time-dependence for transport parameters vanishes and the model translates back to the drift dominated model of Potgieter and le Roux [1992]. This emphasises that long-term cosmic ray modulation cannot be reproduced by only changing the HCS tilt, but that other solar-cycle related changes in all modulation processes are necessary.

When assuming $n = 1$ in Figure 4.5 the model results are not globally compatible with observations towards increased solar activity periods. However, for $n = 1$ there is improved compatibility with observations compared to $n = 0$. Setting $n = 3$ shows improved compatibility towards maximum solar conditions when compared to observations and other n values.

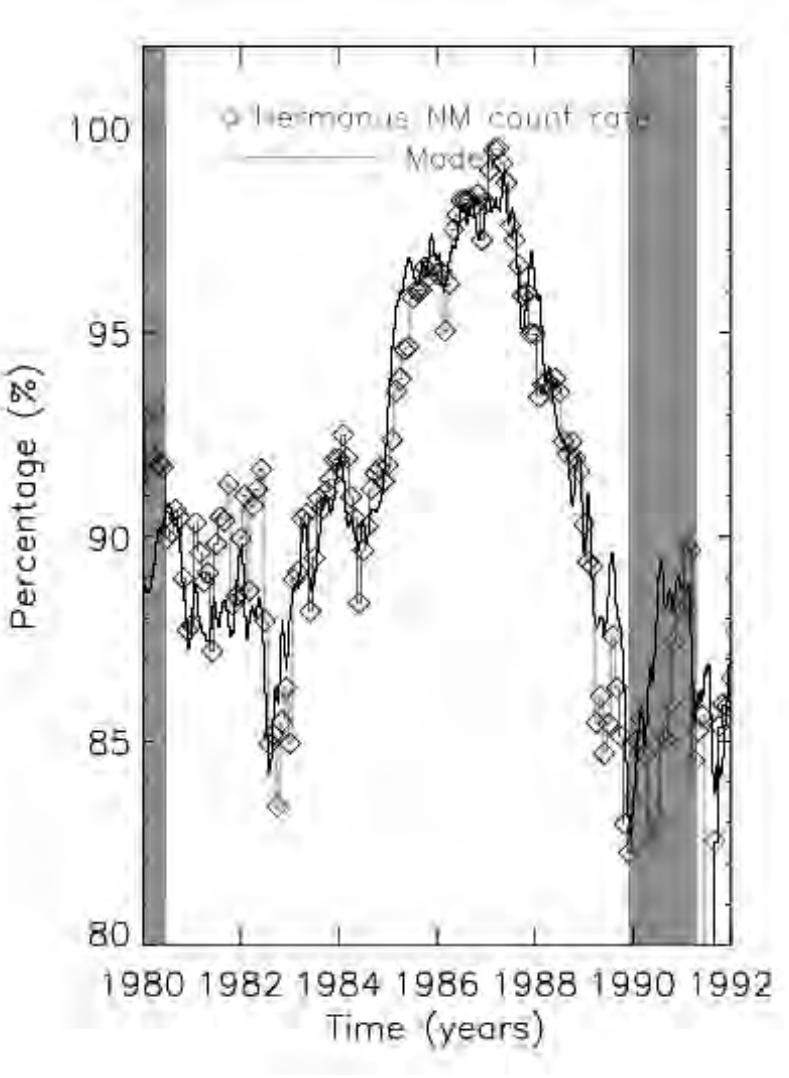

FIGURE 4.4: The computed 16 GV cosmic ray intensities compared to the Hermanus neutron monitor count rates for the period 1980 - 1992 (A $<$ 0 polarity cycle). Note, intensities are normalised to 100 % in 1987. The shaded area shows the period of the HMF polarity reversal. From Ferreira and Potgieter [2004].

Ferreira and Potgieter [2004] concluded from this that, in order for model computations to be realistic, n in Equation 4.1 must change over time, e.g. be solar activity dependent.

Approximating a value that will vary between solar minimum and maximum, Ferreira [2002] and Ferreira and Potgieter [2004] decided on changing n as a function of the tilt angle, α, which is a natural proxy for solar activity. It was assumed that the time-dependence of n be given by:

$$n = \frac{\alpha(t)}{\alpha_0}, \tag{4.2}$$

where $\alpha(t)$ is a time-varying tilt angle and α_0 is a constant. Using Equation 4.2 for n in Equation 4.1 results in a combination of a time-dependence in the HMF and a time-dependent

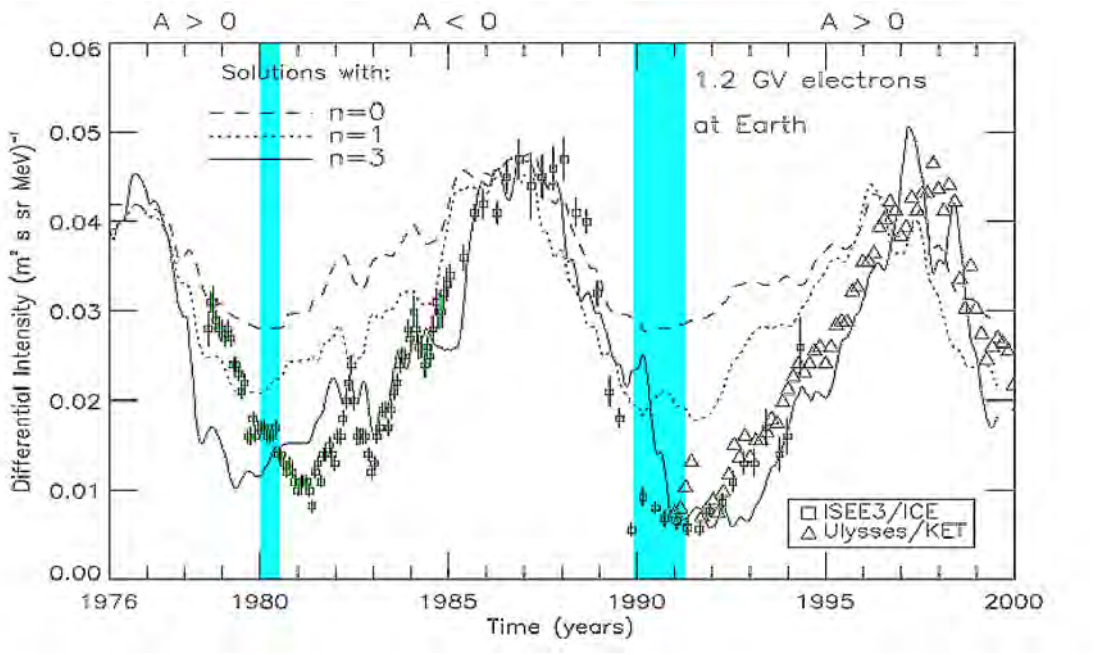

FIGURE 4.5: The computation of 1.2 GV cosmic ray electron differential intensities at Earth for different n values in Equation 4.1 during the period 1976-2000. The model results are compared to the ISSE/ICE and Ulysses/KET observations. Shaded area shows periods of no well-defined HMF polarity. From Ferreira [2002].

HCS tilt angle to establish a time-dependence in the diffusion coefficients. This is the basis of the traditional compound approach. Using this scheme, Ferreira [2002] and Ferreira and Potgieter [2004] computed 1.2 GV cosmic ray electron intensities and compared model runs for two different tilt angle models, as Figure 4.6 shows. These two models correspond to the two different tilt angle models (see discussion in Chapter 2), namely the "classic" model and the "new" model.

From Figure 4.6 it follows that the model computations with the new tilt angle model values as input for Equation 4.2 result in better compatibility with observations for an increasing phase of solar activity compared to the classic tilt angle. However, for decreasing solar activity the model shows better compatibility to observations with the classic tilt angle as input for Equation 4.2. It was then decided that the α with the smallest rate of change over a solar cycle was best to use in the compound approach since it provided the best compatibility with the observations. See also review paper by Ferreira and Potgieter [2003].

4.4.1 Refinement of the Compound Approach

4.4.1.1 Ndiitwani et al. [2005]

Ndiitwani et al. [2005] studied time dependent cosmic ray modulation in the inner heliosphere using the compound approach discussed above. When charge-sign dependent modulation was investigated, Ferreira and Potgieter [2004] realised that their approach still over-estimated

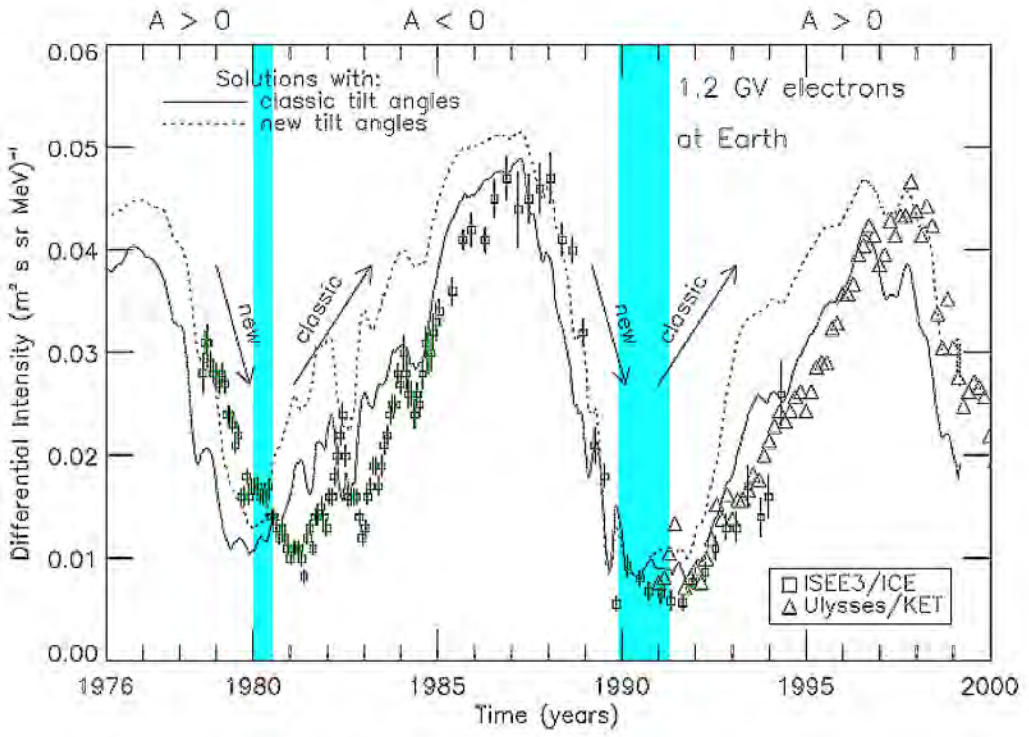

FIGURE 4.6: The computed 1.2 GV cosmic ray electron differential intensities at Earth during the period 1976-2000. The model results are compared to the ISSE/ICE and Ulysses/KET observations. Two model results are shown corresponding to, model results with the classic tilt angle values as input and the other with the new tilt angle values as input to the model. Shaded area shows periods of no well-defined HMF polarity. From Ferreira [2002].

drifts during extreme solar maximum. Ndiitwani et al. [2005] came to a similar conclusion after computing cosmic ray differential intensities for different K_{A0} values using the compound approach, as shown in Figure 4.7. The top panel of this figure shows computations of 2.5 GV cosmic ray proton intensities and the bottom panel the 2.5 GV electrons, both along the Ulysses trajectory. Model calculations are done for different values of K_{A0} using the compound approach. The model shows that, at extreme solar minimum, $K_{A0} = 1.0$ results in better compatibility with observations. As solar activity increases K_{A0} needs to be reduced to $K_{A0} = 0.0$ to result in compatibility with observations.

Estimating the amount of drifts needed over a solar cycle to compute realistic modulation was the main interest of the work of Ndiitwani et al. [2005]. In particular, comparing Ulysses observations to model computations over a full 11-year modulation cycle by studying charge-sign dependent modulation was the aim of their work. By carefully comparing the computed electron and proton intensities along the Ulysses trajectory to observations as in Figure 4.7, Ndiitwani et al. [2005] estimated the amount of drifts needed in the model to compute compatibility with Ulysses observations. Shown in Figure 4.8 is the tilt angle giving an indicative of the solar activity and the percentage drifts needed to compute compatibility with observations along Ulysses trajectory. This figure shows that large drifts are needed for solar

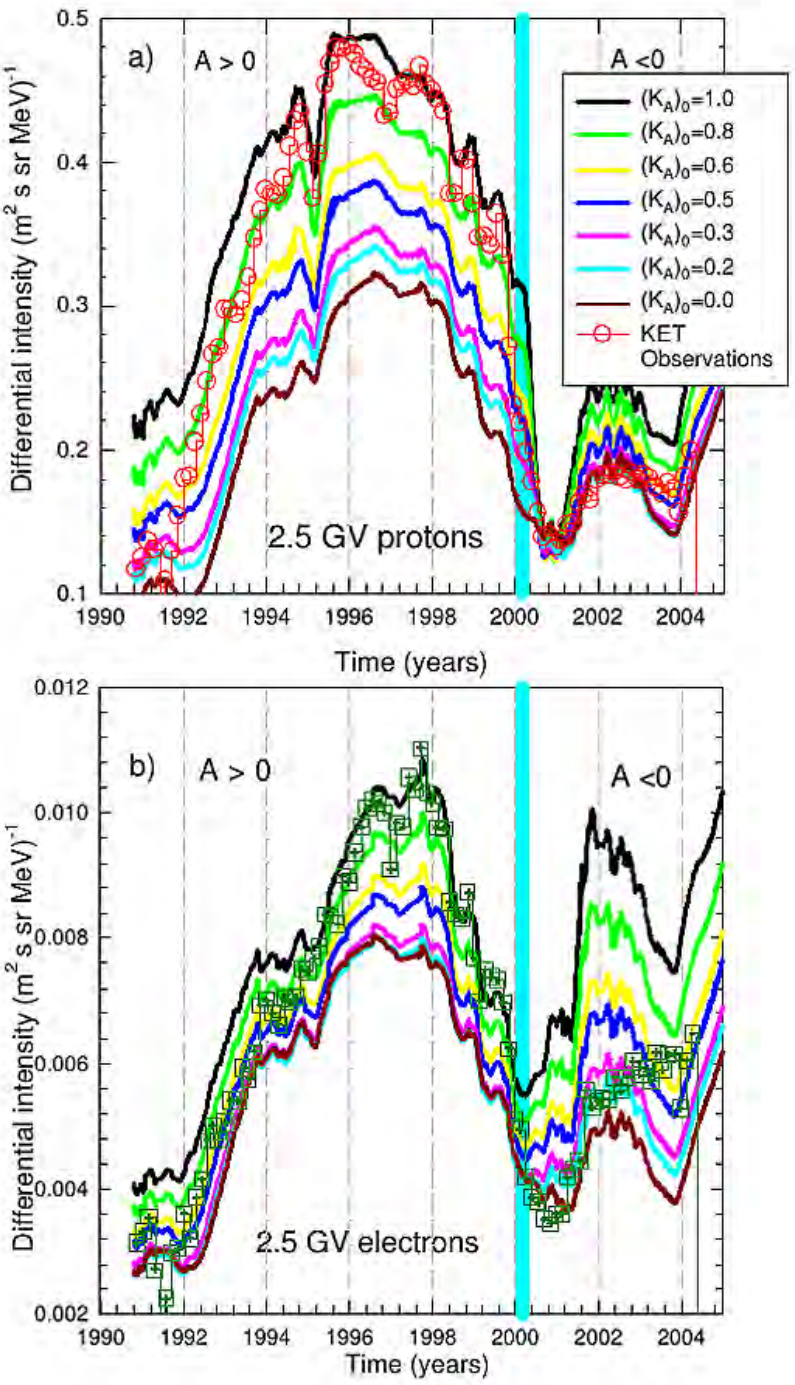

FIGURE 4.7: The computed 2.5 GV cosmic ray proton (top panel) and 2.5 GV cosmic ray electron (bottom panel) differential intensities along the Ulysses trajectory, computed for different K_{A0} values. The model results are compared to the Ulysses/KET observations. The vertical blue line indicates where HMF polarity changes. From Ndiitwani et al. [2005].

minimum (small tilt angle values) and very small drifts even 0% for solar maximum (large tilt angle values) to compute realistic charge-sign dependent modulation.

Using this additional reduction, as shown in Figure 4.8, in the compound approach, Ndiitwani et al. [2005] computed cosmic ray intensities along the Ulysses trajectory, as Figure 4.9 shows.

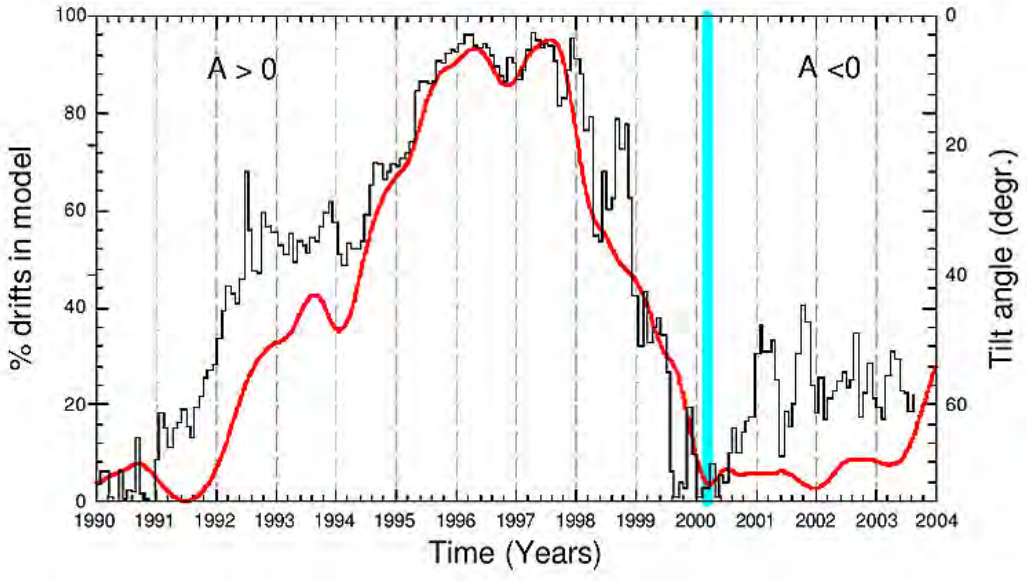

FIGURE 4.8: The percentage of drifts (solid red line) needed in the model to compute realistic modulation when compared to observations. Shown also is the tilt angle (solid black line) as a function of time. Note the axis for the tilt angle is from top (0°) to bottom (80°). From Ndiitwani et al. [2005].

Shown in the figure are the computed 2.5 GV cosmic ray proton and electron intensities (top panel) and the computed 1.2 GV cosmic ray helium and electron intensities (bottom panel) compared to the Ulysses/KET observations. Shown also is the Ulysses trajectory in radial distance and latitude for first and second fast latitude scans. It follows that this additional reduction in drift compute model results that are in excellent agreement with observations at all heliolatitudes and radial distances along the Ulysses trajectory and for different cosmic ray species and energies shown in Figure 4.9.

4.4.1.2 Magidimisha [2011]

Later on, Magidimisha [2011] applied the compound approach as discussed above to calculate cosmic ray proton and electron intensities along the Ulysses trajectory by modifying the scaling of drifts over a solar cycle. The time-dependent function constructed by Magidimisha [2011] to vary drifts as a function of solar activity is given by:

$$f(t) = 1.0 \left[1.1 - \frac{\alpha(t)}{75°}\right]^{0.8}, \tag{4.3}$$

with $\alpha(t)$ a time-varying tilt angle.

Magidimisha [2011] used this function in a time-dependent modulation model to study the charge-sign dependent behaviour of cosmic rays during the three fast latitude scan periods of the Ulysses spacecraft. Figure 4.10 shows the author's modelling of 2.5 GV cosmic ray

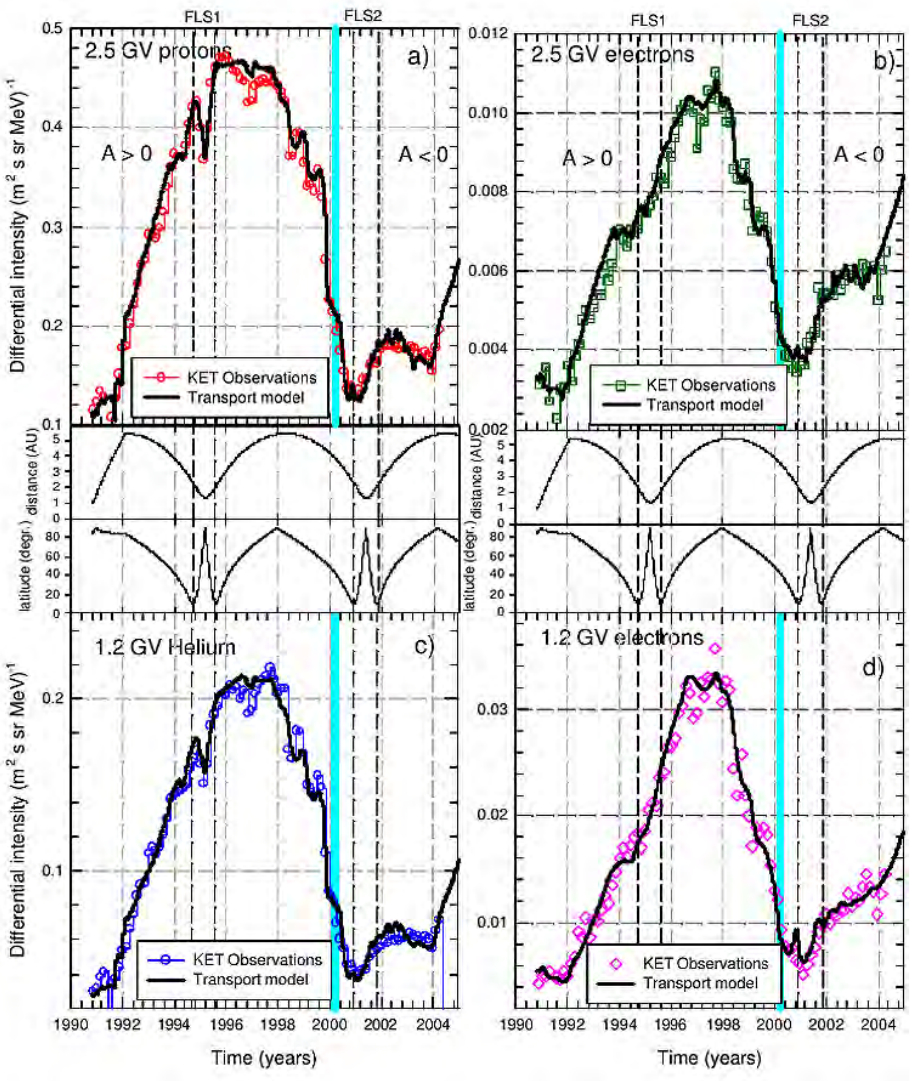

FIGURE 4.9: The computed intensities for 2.5 GV protons and electrons, and for 1.2 GV helium and electrons, compared to the Ulysses/KET observations. Shown in the middle panel are the Ulysses trajectory in radial distance and latitude, with the vertical dashed lines corresponding to the beginning and end of the first fast latitude scan and second fast latitude scan. From Ndiitwani et al. [2005].

proton intensities compared to observations along the Ulysses trajectory. Apart from the model calculations and observations, the latitude of the Ulysses spacecraft is also shown as the dashed red line.

The top panel of Figure 4.10 shows that both the model and the Ulysses observations do respond to changes in Ulysses latitude during the first fast latitude scan. This occurred during an A $>$ 0 polarity cycle and solar minimum. During this cycle positively charged particles drift into the heliosphere over the poles and one expect higher intensities at the polar regions. Both the model and observations confirmed this. The middle panel shows that both the model and observations do not respond to changes in Ulysses latitude for the second fast latitude scan. This occurred during solar maximum when drift effects are reduced [see also Potgieter

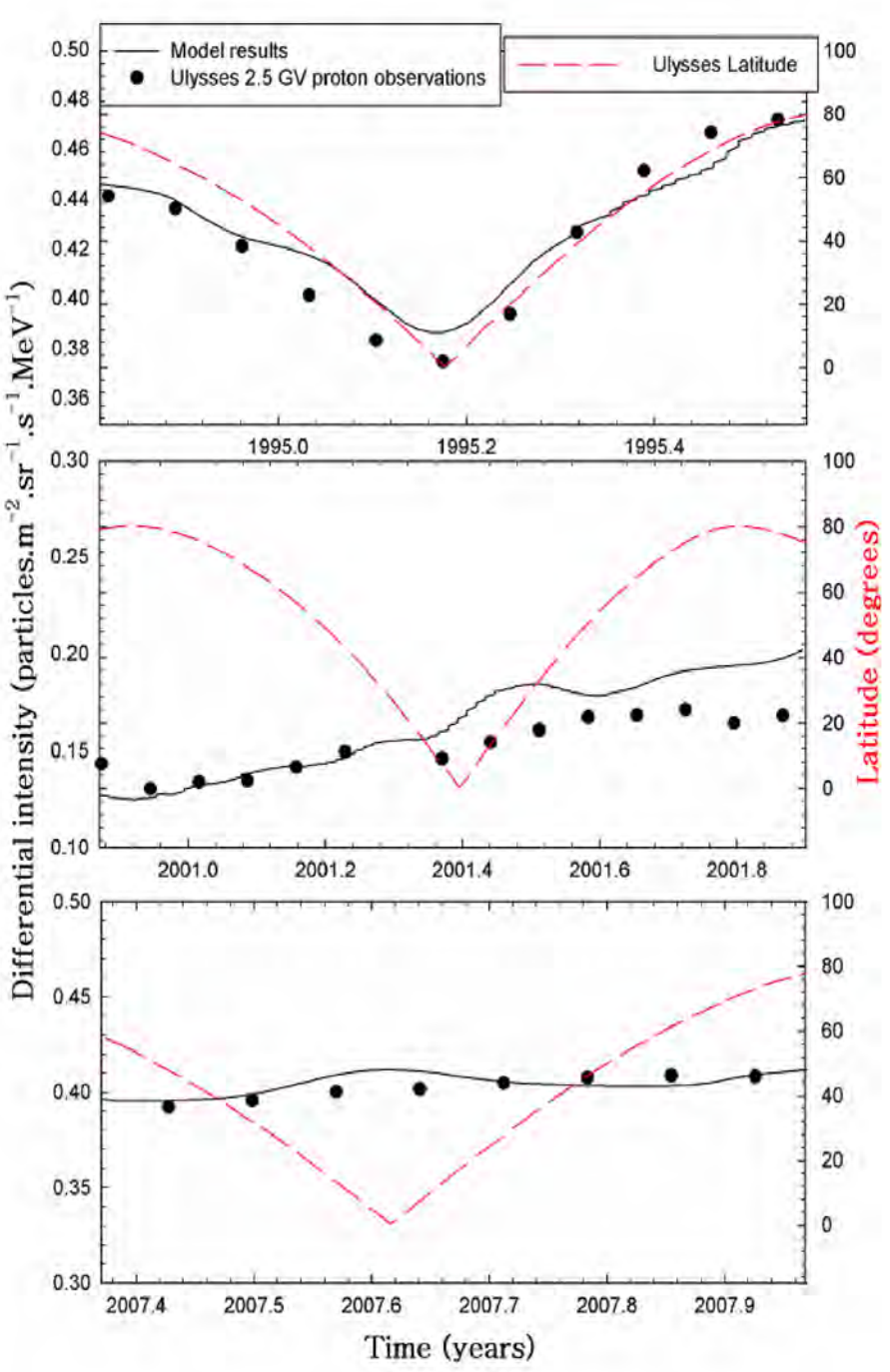

FIGURE 4.10: Model computations (solid lines) of 2.5 GV cosmic ray proton intensities during the three fast latitude scan periods of the Ulysses spacecraft. Shown also are the Ulysses observations (filled circles) and the latitude (red dashed lines) of the Ulysses spacecraft, with the equatorial plane at 0°. From Magidimisha [2011].

and le Roux, 1992]. The third fast latitude scan by Ulysses occurred during an A < 0 cycle. Model results and observations are shown in the bottom panel. This fast latitude scan also took place during solar minimum. Both the model and observations show no clear latitudinal gradients for this polarity cycle when protons drift inward along the HCS.

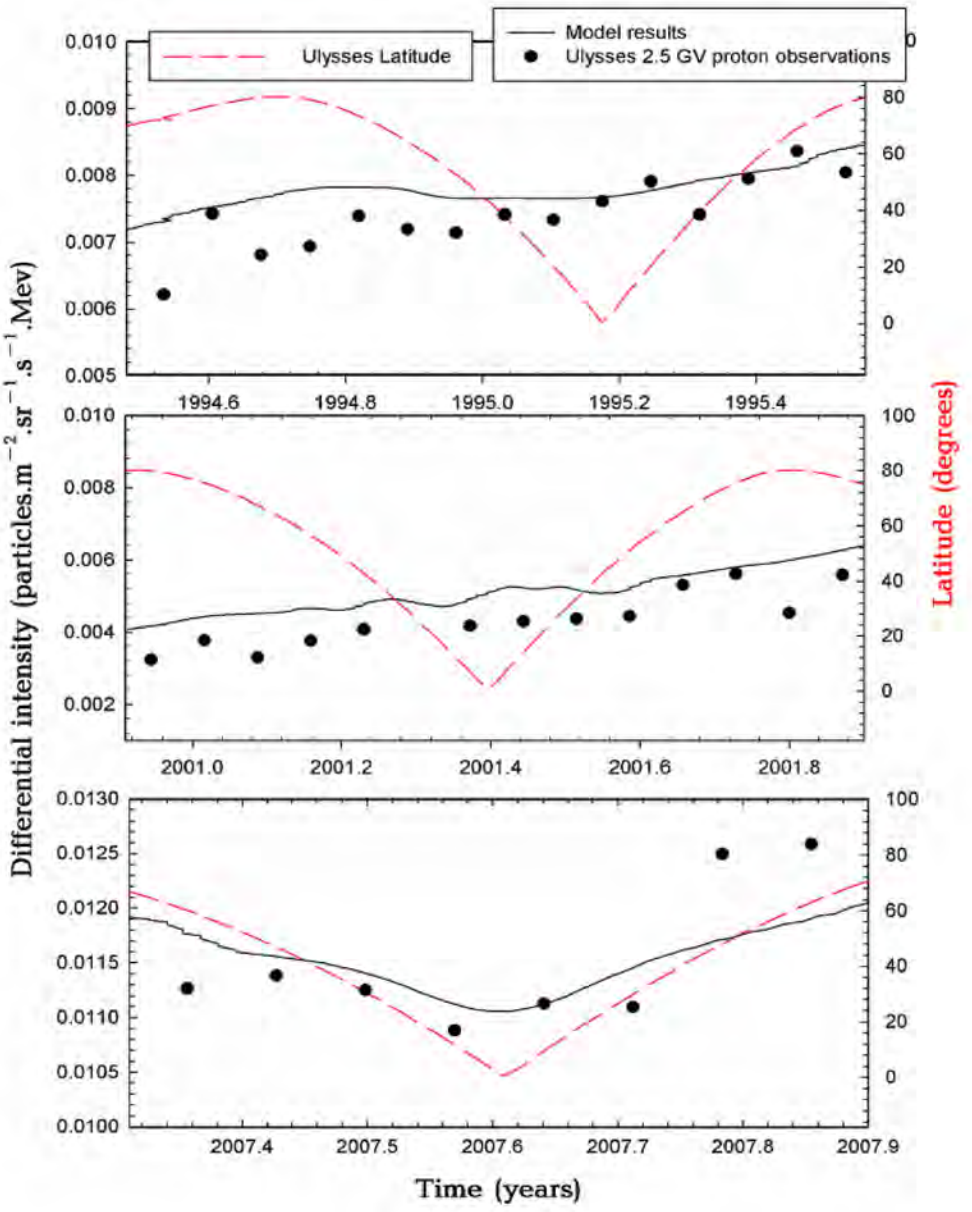

FIGURE 4.11: Similar to Figure 4.10 but for electrons (Note the legend should read 'Ulysses 2.5 GV electron observations'). From Magidimisha [2011].

Figure 4.11 is similar to Figure 4.10 but for cosmic ray electrons. The top panel shows that, for electrons during the first fast latitude scan which occurred during the A $>$ 0 polarity cycle, there was no clear latitudinal gradients as it was with the cosmic ray protons (see top panel of Figure 4.10). During this cycle negatively charged particles drift inward along the equatorial region. The middle panel shows results for the second fast latitude scan period which occurred during solar maximum. Similar to protons, the electrons show no clear latitudinal gradient as both the model and the observations did not respond to changes in the Ulysses latitude. For the third fast latitude scan, the model and electron observations show a clear latitudinal dependence. This fast latitude scan occurred during an A $<$ 0 cycle, where negatively charged particles drift inward over the poles. This is similar to the first fast latitude scan period for

protons.

4.4.1.3 Manuel [2012]

After the study of Magidimisha [2011], the compound approach was also applied by Manuel [2012] and some of the results of this application were published by Manuel et al. [2011*a*, 2014]. Figure 4.12 shows the compound approach results of computed 2.5 GV proton cosmic ray intensities along Voyager 1 and 2 trajectories and at Earth and compared to the $E >$ 70 MeV Voyager 1 and 2 (from $http : //voyager.gsfc.nasa.gov$) observations in the outer heliosphere and to the $E >$ 70 MeV IMP 8 (from $http : //astro.nmsu.edu$) and 2.5 GV Ulysses [Heber et al., 2009] observations in the inner heliosphere.

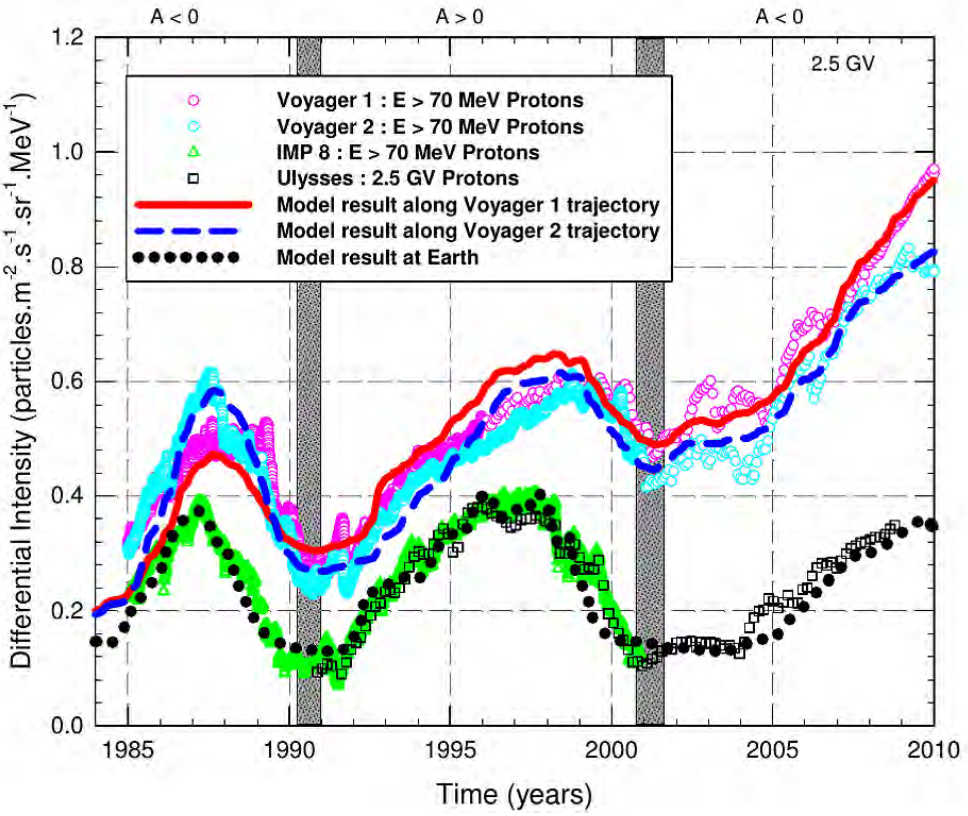

FIGURE 4.12: Computation of 2.5 GV cosmic ray proton intensities at Earth and along the Voyager 1 and 2 trajectories using the compound approach. The model results are compared to $E >$ 70 MeV proton observations by Voyager 1 and 2 (from $http : //voyager.gsfc.nasa.gov$), at Earth the model results are compared to $E >$ 70 MeV proton observations from IMP 8 (from $http : //astro.nmsu.edu$) and $\sim$ 2.5 GV proton observations from Ulysses [Heber et al., 2009] and the shaded areas represent the transition of the HMF when there is no dominant HMF polarity. From Manuel [2012].

The figure shows that the traditional compound approach as used by Ferreira and Potgieter [2004], Ndiitwani et al. [2005] and Magidimisha [2011] computed on a global scale is compatible to 2.5 GV cosmic ray differential intensities in the inner and outer heliosphere when compared to different spacecraft observations. It also reproduced correct latitudinal cosmic ray intensity

gradients when compared to the Voyager observations, with Voyager 1 and 2 at different heliolatitudes. However, note that Ulysses observations were used as an extension for IMP 8 data at Earth (1 AU).

However, as mentioned earlier, the time-dependence for all transport coefficients in the compound approach was first constructed by Ferreira [2002] and Ferreira and Potgieter [2004] by comparing model results with different spacecraft observations over consecutive solar cycles. This was done solely because at that stage it was not well-known how the diffusion and drift coefficients should change over a solar cycle. However, progress as discussed in Chapter 3 by e.g. Teufel and Schlickeiser [2002], Shalchi et al. [2004] and Minnie et al. [2007] on how transport coefficients depend on turbulence quantities, paved a way for Manuel [2012] and Manuel et al. [2014] to modify the compound approach by incorporating these theoretical advances on transport coefficients in a time-dependent modulation model. This modified compound approach is discussed next.

4.4.2 The Modified Compound Approach

The work of Teufel and Schlickeiser [2002] gives an applicable expression of the parallel mean free path in the range 10^{-1} MV < P < 10^{4} MV (as of interest in this work) for protons in the inner heliosphere, as $\lambda_{||} \propto P^{1/3}$. This was assumed for the parallel mean free path in the numerical model by Manuel [2012] and Manuel et al. [2014] and at 2.5 GV and the expression is given by

$$\lambda_{||} = C_1 \left(\frac{P}{P_0}\right)^{\frac{1}{3}} \left(\frac{r}{r_0}\right)^{C_2} f_2(t), \quad \text{for } r < r_{ts} \tag{4.4}$$

and

$$\lambda_{||} = \frac{C_1}{s_k} \left(\frac{P}{P_0}\right)^{\frac{1}{3}} \left(\frac{r}{r_0}\right)^{C_2} \left(\frac{r_{ts}}{r}\right) f_2(t), \quad \text{for } r \geq r_{ts} \tag{4.5}$$

where $P_0 = 1$ MV, $r_0 = 1$ AU, C_1 (in units of AU) is a constant that determines the absolute value of the mean free path, C_2 a constant that determines the radial dependence, r_{ts} is the termination shock position, s_k is the compression ratio and $f_2(t)$ a dimensionless time-dependent function for $\lambda_{||}$. The time-dependent changes as incorporated by this function are transported out into the heliosphere at the solar wind speed.

It was pointed out by Burlaga et al. [2007] following the Voyager observations in the inner heliosheath that for $r > r_{ts}$, $B \propto r$. This implies that, if the diffusion coefficient have some dependence on B, it will be affected across the termination shock. The work of Manuel [2012]

and Manuel et al. [2014] assumed that Equation 4.4 is valid in the inner heliosphere and Equation 4.5 in the outer heliosphere, but also that in the outer heliosphere diffusion coefficients are inversely proportional to B. Similar assumptions were made also by e.g. Florinski et al. [2003] and Ferreira and Scherer [2006] when calculating cosmic ray intensities in the heliosphere. These authors used results from hydrodynamic and magneto-hydrodynamic models to calculate the plasma and magnetic field in this region.

For particles moving with speed v, the parallel diffusion coefficient is given by,

$$K_{||} = \lambda_{||}\frac{v}{3}. \tag{4.6}$$

To determine a time-dependence $f_2(t)$ in Equations 4.4 and 4.5, the full expression of the mean free path from the work of Teufel and Schlickeiser [2003] given by

$$\lambda_{||} = \frac{3s}{\sqrt{\pi}(s-1)}\frac{R^2}{b_k k_{min}}\left(\frac{B}{\delta B_{slab,x}}\right)^2\left[\frac{b_k}{4\sqrt{\pi}} + \frac{2}{\sqrt{\pi}(2-s)(4-s)}\frac{b_k}{R^2}\right], \tag{4.7}$$

where $s = 5/3$ is the spectral index of the inertial range as derived by Kolmogorov, b_k a fraction of particle speed to Alfvén speed assuming maximum dynamical effects, $k_{min} = 10^{-10}\mathrm{m}^{-1}$ is the spectral break point between the inertial and energy range on the turbulence power spectrum at 1 AU, $R = k_{min}R_L$, $R_L = \frac{P}{Bc}$ is the Larmor radius, c the speed of light and $\delta B^2_{slab,x}$ the x-component of the slab variance, is used.

Considering only the time-varying quantities B and δB^2, Equation 4.7 can be approximated as

$$\lambda_{||} \propto \left(\frac{1}{\delta B_{slab,x}}\right)^2\left[\frac{1}{4} + \frac{18}{7}\left(\frac{Bc}{Pk_{min}}\right)^{5/3}\right]. \tag{4.8}$$

The quantity δB should be a vector (of the fluctuating field) of length zero (averaging over the turbulent field), however, the root-mean-square value of this quantity is used in the model.

The time-dependent function $f_2(t)$ can then be assumed as

$$f_2(t) = C_4\left(\frac{1}{\delta B(t)}\right)^2\left[\frac{1}{4} + \frac{18}{7}\left(\frac{B(t)c}{Pk_{min}}\right)^{5/3}\right], \tag{4.9}$$

with C_4 a constant with the units of $(\mathrm{nT})^2$.

For perpendicular diffusion in the radial direction, Manuel [2012] and Manuel et al. [2014] assumed

$$K_{\perp r} = aK_{||}\frac{f_3(t)}{f_2(t)}, \tag{4.10}$$

and for perpendicular diffusion in the polar direction

$$K_{\perp \theta} = bK_{||}F(\theta)\frac{f_3(t)}{f_2(t)}. \tag{4.11}$$

As before, a is the ratio of the perpendicular diffusion coefficient in the radial direction to the parallel diffusion coefficient, b the ratio of the perpendicular diffusion coefficient in the polar direction to the parallel diffusion coefficient, $F(\theta)$ as in Equation 3.22 in Chapter 3, is a function that increases $K_{\perp\theta}$ towards the poles by a factor of 6 as was used by e.g. Ferreira and Potgieter [2004], Manuel et al. [2011*a*] and Manuel et al. [2011*b*]. In Equations 4.10 and 4.11 $f_3(t)$ is a time-dependent function incorporating solar cycle related changes in the perpendicular diffusion coefficients. Note that Equations 4.10 and 4.11 are divided by $f_2(t)$ to remove the time-dependence of $K_{||}$ in $K_\perp$. The scaling of $K_\perp$ as $K_{||}$ used here is adopted based on earlier simulations (e.g. Giacalone and Jokipii [1999] and Qin et al. [2002]).

For the time-dependence in the $K_\perp$ Shalchi et al. [2004] supplied an expression for the perpendicular mean free path $\lambda_\perp$ as,

$$\lambda_\perp \approx \left[\frac{2\eta - 1}{4\eta}F_2(\eta)a_k^2\frac{\delta B_{2D}^2}{B^2}\sqrt{3}l_{2D}\right]^{2/3}\lambda_{||}^{\frac{1}{3}}, \tag{4.12}$$

which Manuel et al. [2014] used to deduce $f_3(t)$. Here $\eta = 5/6$ is the spectral index of slab/2D model magnetic field, $a_k = 1/\sqrt{3}$ a numerical factor, l_{2D} the 2D correlation length and

$$F_2(\eta) = \sqrt{\pi}\frac{\Gamma(\eta)}{\Gamma(\eta - \frac{1}{2})}\frac{2\eta}{2\eta - 1}, \tag{4.13}$$

where $\Gamma(\eta) = \int_0^\infty x^{\eta-1}e^{-x}dx$ for $\eta > 0$.

Considering only time varying quantities, Manuel et al. [2014] approximated the $\lambda_\perp$ expression as

$$\lambda_\perp \propto \left(\frac{\delta B_{2D}}{B}\right)^{4/3}\left(\left(\frac{1}{\delta B_{slab,x}}\right)^2\left[\frac{1}{4} + \frac{18}{7}\left(\frac{Bc}{Pk_{min}}\right)^{5/3}\right]\right)^{1/3}, \tag{4.14}$$

from which these authors deduced an expression for $f_3(t)$, given as

$$f_3(t) = C_5 \left(\frac{\delta B(t)}{B(t)}\right)^{4/3} \left(\left(\frac{1}{\delta B(t)}\right)^2 \left[\frac{1}{4} + \frac{18}{7}\left(\frac{B(t)c}{Pk_{min}}\right)^{5/3}\right]\right)^{1/3}, \tag{4.15}$$

which is the time-dependence for the $K_\perp$, with C_5 a constant in units of $(\mathrm{nT})^{2/3}$.

The expression for a time-dependence of the drift coefficient is based on the theoretical work done by Minnie et al. [2007]. These authors showed that as δB changes over a solar cycle it affects the drift coefficient. Manuel et al. [2014] also assumed a similar dependence for the drift coefficient on solar activity, but rather used the tilt angle α instead of δB^2. The reason for this is to scale the drift K_A for increasing/decreasing solar activity [Ferreira and Potgieter, 2004, Ndiitwani et al., 2005, Manuel et al., 2011*b*] in order to compute realistic charge-sign dependence over a solar cycle as was done by Ndiitwani et al. [2005] and Magidimisha [2011]. A function to scale drifts to almost zero for extreme solar maximum and almost full drifts for solar minimum is given as

$$f_1(t) = 0.013 \times \frac{75.0^\circ - \alpha(t)}{\alpha_c}, \tag{4.16}$$

with $\alpha(t)$ a time-varying tilt angle, and $\alpha_c = 1^\circ$. Note that this expression is only valid for $\alpha(t)$ less than 75°.

The drift coefficient as assumed in the work of Manuel et al. [2014], is given by

$$K_A = K_{A0}\frac{\beta P}{3B}\frac{10P^2}{10P^2+1}f_1(t). \tag{4.17}$$

Manuel et al. [2014] used these time-dependent functions for transport coefficients with this new approach known as the modified compound approach.

The results of Manuel et al. [2014] using the modified compound approach are shown in Figure 4.13. The figure shows the computed cosmic ray intensities at Earth and along the Voyager 1 and 2 trajectories. Shown also are $E > 70$ MeV proton observations by Voyager 1 and 2, $E > 70$ MeV proton observations from IMP 8 and ~ 2.5 GV proton observations from Ulysses spacecraft.

Figure 4.13 shows that the model agrees on a global scale with observations along both Voyager 1 and 2 trajectories and also at Earth. For some periods the model is less compatible, e.g. at Earth it is not compatible with observations for the period 2001 - 2004 corresponding to extreme solar maximum. Also along the Voyager 1 and 2 trajectories the model shows incompatibility with observations from $\sim$ 2001 onwards. For the period 1985 - 1990 the model along the Voyager 1 trajectory is also in disagreement with observations. For this period observations showed a plateau-like intensity profile but the model shows a peak-like profile.

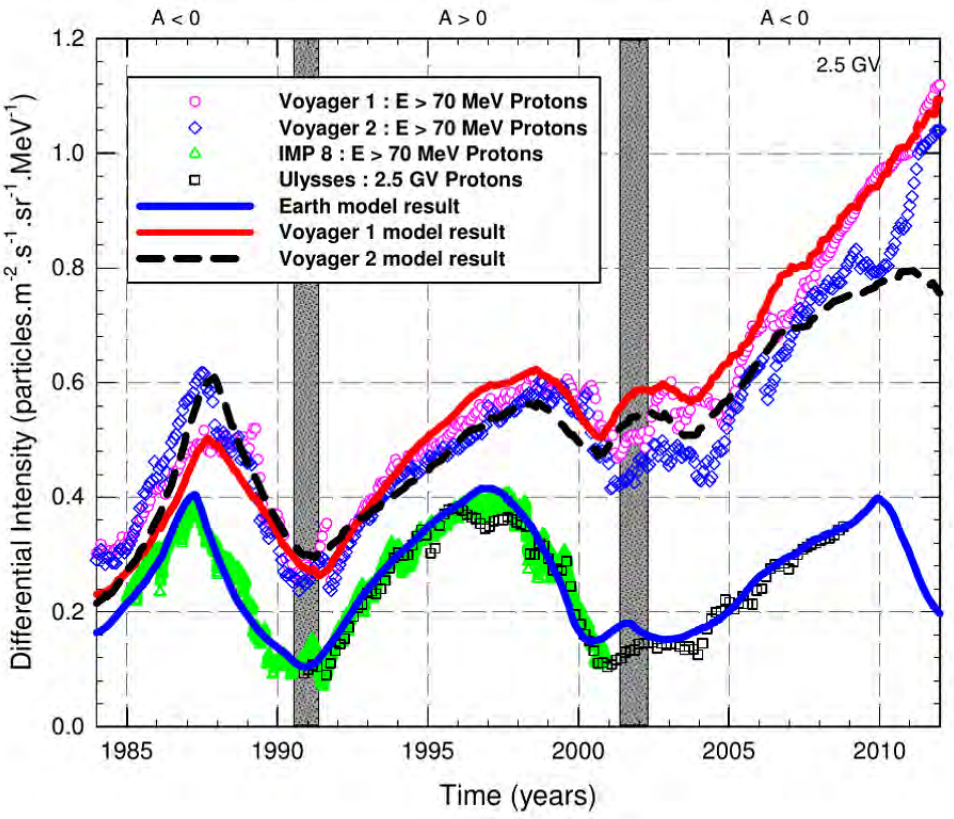

FIGURE 4.13: Results from the modified compound approach computation of 2.5 GV cosmic ray proton intensities at Earth and along the Voyager 1 and 2 trajectories. The model results are compared to $E > 70$ MeV proton observations by Voyager 1 and 2 (from $http://voyager.gsfc.nasa.gov$), at Earth the model results are compared to $E > 70$ MeV proton observations from IMP 8 (from $http://astro.nmsu.edu$) and $\sim$ 2.5 GV proton observations from Ulysses [Heber et al., 2009]. The shaded areas represent the transition of the HMF when there is no dominant HMF polarity. From Manuel [2012].

Along the Voyager 2 trajectory the model agrees with observations for this period. The incompatibility between the model and the mentioned Voyager observations for some periods is investigated in chapters to follow.

4.4.2.1 Time-dependent Termination Shock Position

The work of Manuel [2012] also showed the effects of a time-dependent termination shock position on cosmic ray modulation along the Voyager spacecraft trajectories. The model incorporated the calculated time-dependent termination shock positions as proposed by Snyman [2007] and Webber and Intriligator [2011].

Figure 4.14 shows the time-dependent termination shock positions as proposed by Snyman [2007] and those by Webber and Intriligator [2011]. Predictions are shown both along the Voyager 1 and 2 trajectories and in the outer heliosphere. As shown, along the Voyager 1 trajectory around $\sim$ 2006 the termination shock is at $\sim$ 86.5 AU, around $\sim$ 2008 is at $\sim$ 86

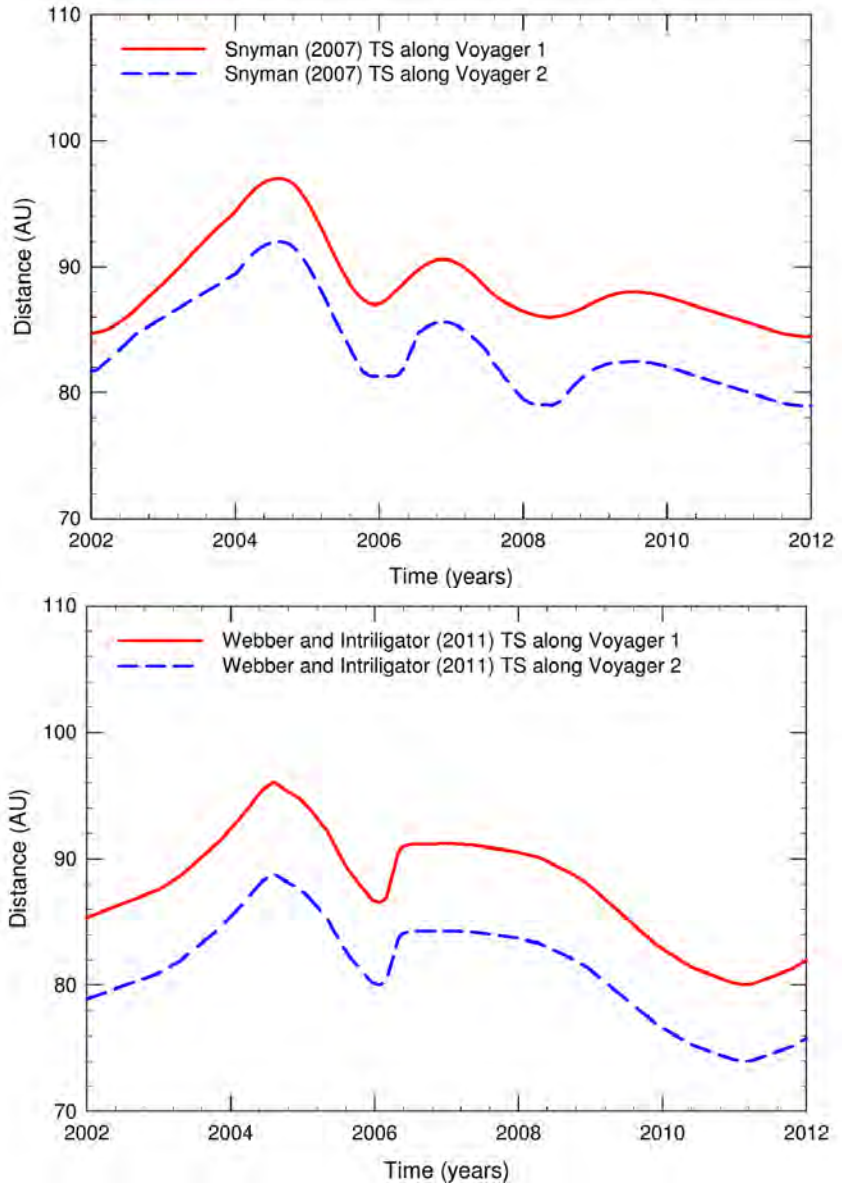

FIGURE 4.14: Shown in the top panel is the time-dependent termination shock positions as proposed by Snyman [2007], and in the bottom panel is the time-dependent termination shock positions as proposed by Webber and Intriligator [2011], both along Voyager 1 and 2 trajectories and for the period 2002 - 2012. From Manuel [2012].

AU and in 2012 the termination shock is at $\sim$ 84 AU. In the bottom panel oscillations appear to be more random as compared to the top panel, along the Voyager 1 trajectory around $\sim$ 2006 the termination shock is at $\sim$ 86 AU, around $\sim$ 2008 is at $\sim$ 90 AU and in 2012 the termination shock is at $\sim$ 82 AU.

Figure 4.15 shows the corresponding computed 2.5 GV cosmic ray proton intensities along Voyager 1 trajectory, with the first calculation assuming a static termination shock position (shown by a solid red line) in the model. The other two calculations assume the two time-dependent termination shock positions proposed by Snyman [2007] (shown by dashed blue line)

and Webber and Intriligator [2011] (shown by dotted black line). Shown also for comparison is $E > 70$ MeV proton observations by Voyager 1.

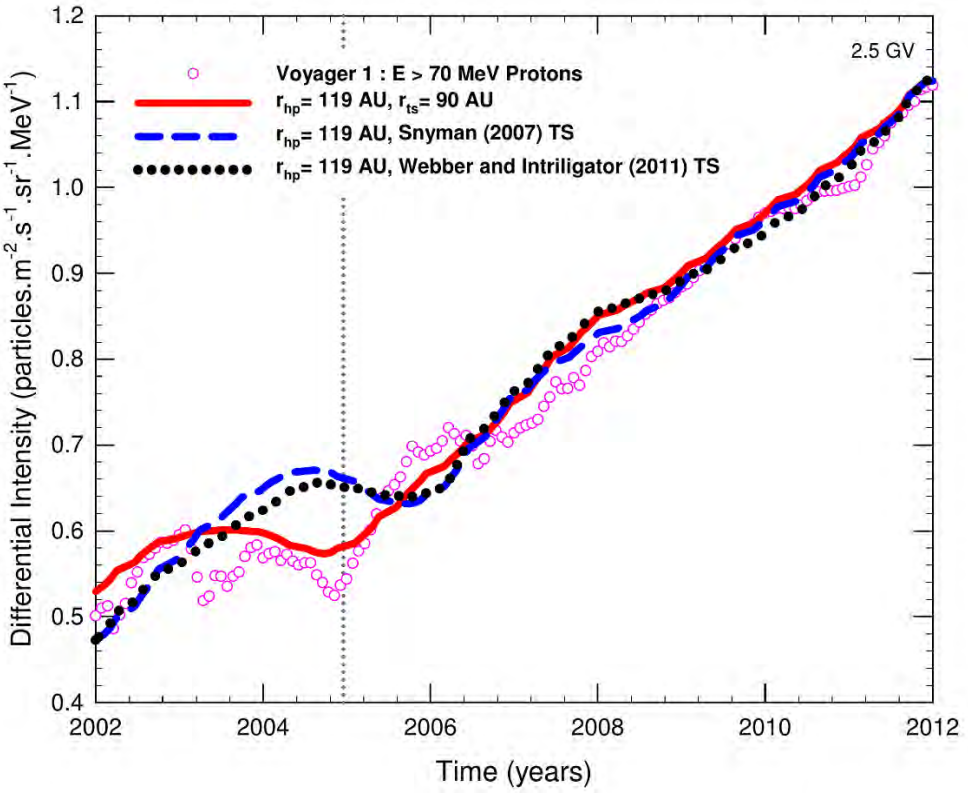

FIGURE 4.15: Computed 2.5 GV cosmic ray proton intensities along Voyager 1 trajectory for the time period 2002 - 2012. Results shown are for three different scenarios, i.e., the first scenario shown by red solid line is with a static termination shock position, the second scenario shown as a dashed blue line is with time-dependent termination shock position according to Snyman [2007], and the last scenario shown by a dotted black line is with time-dependent termination shock position according to Webber and Intriligator [2011]. From Manuel [2012].

From Figure 4.15 it follows that the first scenario (static termination shock and heliopause) agrees with observations on a global scale, but also failed to reproduce observations especially during periods e.g., $\sim$ 2003 - 2005 when step-like decreases were observed due to propagating diffusion barriers as these structures are not included in the model. However, results of the other two scenarios show that both time-dependent termination shock positions proposed by Snyman [2007] and Webber and Intriligator [2011] are in agreement with observations except for the period $\sim$ 2003 - 2005, during which the model computed intensities which are out of phase with observations, i.e. the model results (with a moving shock) increase while the observations decrease. From these results it follows that a time-dependent termination shock position is only important for regions close to the termination shock. The periods of interest in this work do not correspond to either Voyager spacecraft being close to the termination shock and therefore a static shock position is assumed.

4.5 Summary

In this chapter time-dependent cosmic ray modulation was discussed as reported by different authors using different numerical modulation models. As shown, the time-dependent drift model of le Roux and Potgieter [1990] which computed long-term cosmic ray modulation with the tilt angle as the only time-dependent parameter, was compatible with observations only for periods of low solar activity. The model was improved by le Roux and Potgieter [1995] by incorporating GMIRs in the time-dependent drift model. This GMIR-drift approach successfully simulated a complete 11 and 22 year cosmic ray modulation cycle.

Cane et al. [1999], le Roux and Fichtner [1999] and Wibberenz et al. [2002] also suggested that long-term changes in the diffusion coefficients are needed. Ferreira [2002] and Ferreira and Potgieter [2004] developed a compound approach to study this concept by introducing a time-dependence for all transport parameters without including GMIRs directly in the model. It was shown that this approach successfully computed compatible cosmic ray intensities in the inner and outer heliosphere when compared to observations. Later, refinements to the compound approach were proposed by Ndiitwani et al. [2005], Magidimisha [2011] and Manuel [2012].

The compound approach is based on an empirical approach where model results were compared to different spacecraft observations to construct a realistic time-dependence in the transport coefficients. This was done because it was not well-known at that time how diffusion and drift coefficients change over a solar cycle. Progress in the theoretical work on transport parameters made possible the modification of the compound approach by Manuel [2012] and Manuel et al. [2014]. It was shown that, on a global scale, the modified compound approach is compatible with observations from different spacecraft, but there are periods that the model results disagree with observations. One of them is the 1985 - 1990 period, which is one of the periods of interest for this work.

Chapter 5

Investigating the 1985 - 1990 period of cosmic ray observations along Voyager spacecraft trajectories

5.1 Introduction

It was pointed out in the previous chapter, that model results show, when compared to Voyager 1 and 2 spacecraft observations, that the modified compound approach of Manuel [2012] and Manuel et al. [2014] computed intensities compatible to Voyager 2 measurements for the period 1985 - 1990. However, this is not the case for the Voyager 1 measurements. Along the Voyager 1 trajectory the modified compound approach computes a peak-like intensity profile around solar minimum while observations show a plateau-like intensity profile.

In this chapter this period is further investigated by analysing different modulation parameters while the next chapter focuses on improving the modified compound approach of Manuel [2012] and Manuel et al. [2014]. A refinement of the model is proposed and applied in detail to the 1985-1990 period in the next chapter. This chapter however focuses on first understanding the observed modulation parameters (i.e. solar wind speed, heliospheric magnetic field and the tilt angle) along Voyager 1 and 2 trajectories, in order to establish if there is a possibility that they could lead to different modulation conditions between Voyager 1 and 2 due to their different positions in latitude and radial distance.

5.2 The 1985 - 1990 period

As a first objective, the Voyager mission had to do an investigation of different planets (i.e. Jupiter, Saturn, Neptune, and Uranus) (voyager.jpl.nasa.gov/mission/interstellar.html). Following the launch of Voyager 1, the spacecraft was realigned by NASA in 1980 for its encounter with Saturn, after it completed an investigation of Jupiter and its system. NASA found themselves in a tricky situation of choosing whether to use Voyager for a flyby of Titan (Saturn's

moon) and therefore risk the possibility of continuing to Pluto, or to do a flyby of Saturn, which would reduce the risk and therefore not affect the possibility of an up-close study of Pluto. It was then decided in favour of Titan for being of greater scientific value. Changes were then made to Voyager's trajectory, which resulted in Voyager 1 being out of the ecliptic plane and travelling to higher latitudes compared to Voyager 2.

The trajectories of the Voyager 1 and 2 spacecraft are shown in Figure 5.1. The top panel of the figure shows the radial distance of Voyager 1 and 2 and the bottom panel the polar angle, both as a function of time. This figure shows the two Voyager spacecraft being at different radial distances and latitudes (polar angles). As the figure illustrates and the discussion above shows Voyager 1 went up to higher latitudes (smaller polar angle) in the northern hemisphere of the heliosphere after $\sim$ 1981 while Voyager 2 stayed near the equatorial region for the time interval considered in this chapter.

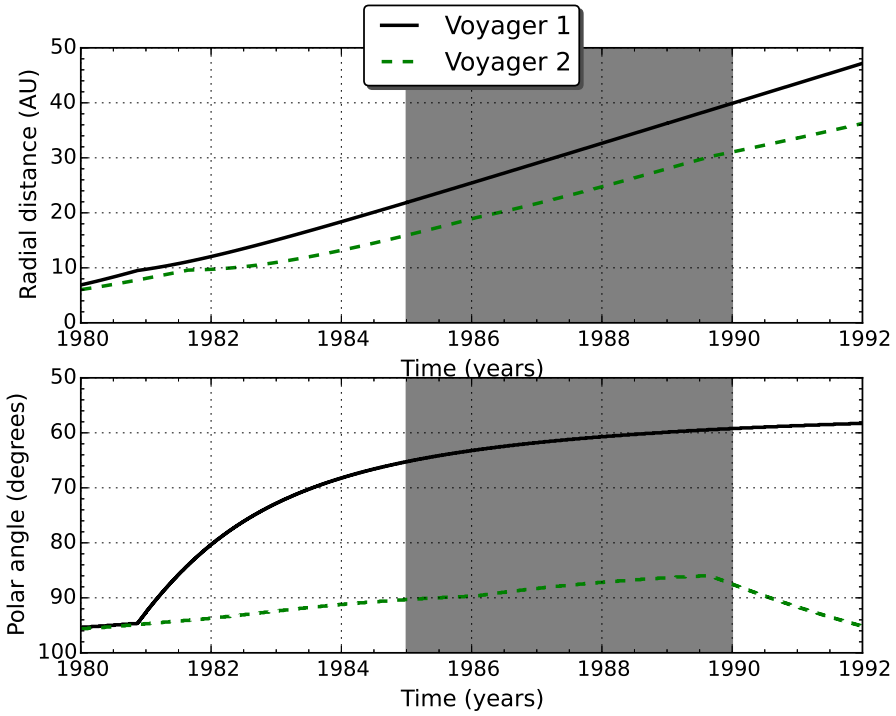

FIGURE 5.1: The Voyager 1 and Voyager 2 spacecraft trajectories, with the top panel showing the radial distance and the bottom panel the polar angle as a function of time. The equatorial plane is at $\theta = 90°$ and the shaded areas show the period of interest in this work. Data from *http : //cohoweb.gsfc.nasa.gov*.

The period of interest in this work is shown as shaded areas in Figure 5.1. For this period, the radial and latitudinal gradients of cosmic ray observations by Voyager 1 and 2 were successfully simulated in detail by Potgieter and le Roux [1992]. This is shown in the top panel of Figure 5.2, which shows the calculated 1 GeV cosmic ray proton intensities for two moving observers resembling Voyager 1 and 2. These authors used a time-dependent drift model which included the effects of the wavy HCS as the only changing parameter. Their approach correctly

predicted the time difference between the minimum modulation at Earth and at some radial distance further from the Sun and also that drift effects give rise to the latitude-dependence as observed by Voyager 1 and 2 for this period.

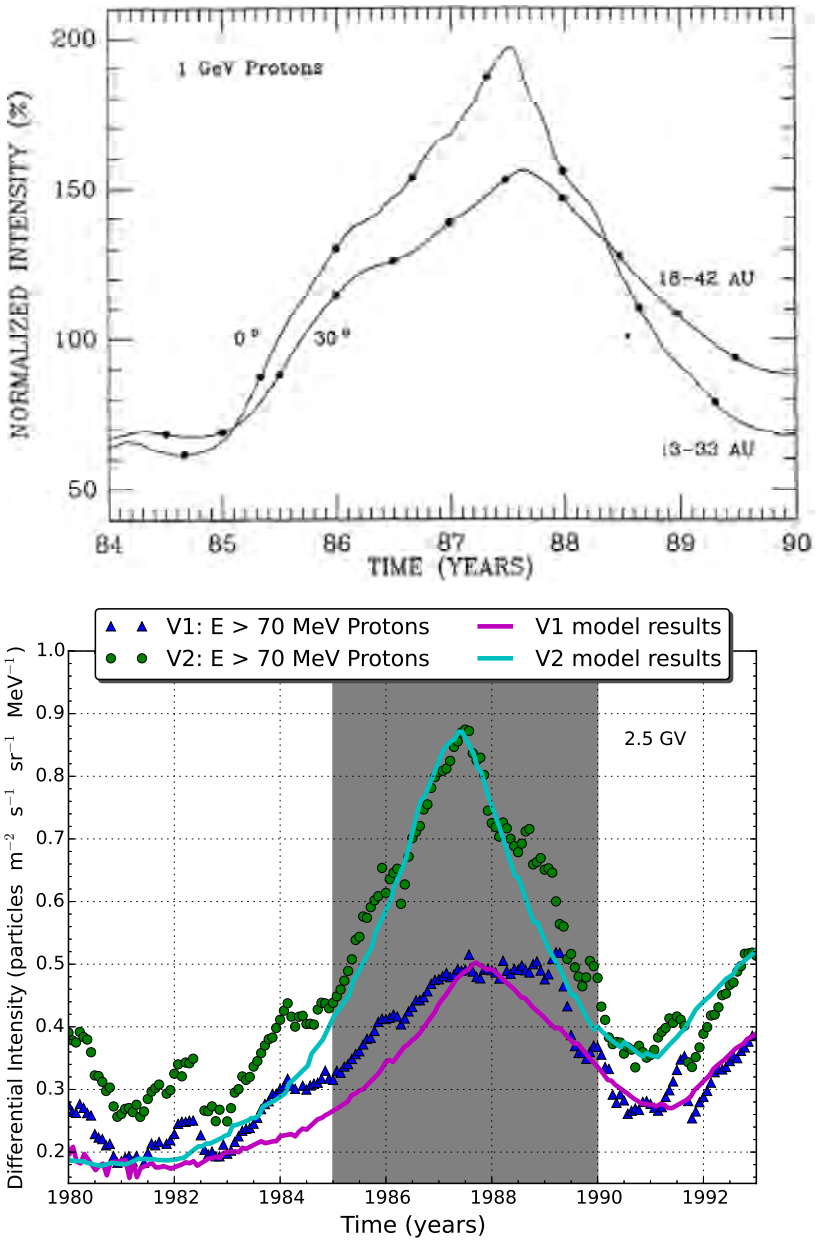

FIGURE 5.2: Top panel shows the calculated 1 GeV cosmic ray proton intensities for two moving observers resembling the movements of Voyager 1 and Voyager 2 (Adapted from Potgieter and le Roux [1992]). Bottom panel shows the computed 2.5 GV cosmic ray proton intensities along Voyager 1 and 2. The results are compared to Voyager 1 and 2 E > 70 MeV protons. Data from *http* : *//voyager.gsfc.nasa.gov*.

As shown in the previous chapter, Manuel [2012] and Manuel et al. [2014] also produced results which are in good agreement with observations on a global scale, as the bottom panel of Figure 5.2 shows the computed 2.5 GV cosmic ray proton intensities along the Voyager 1 and 2 and are compared to Voyager 1 and 2 protons with $E > 70$ MeV. It is true from observations that for a negative HMF polarity cycle protons gain access into the heliosphere along the

HCS and this is clear from the Voyager 2 observations and model predictions showing higher intensities along the Voyager 2 trajectory compared to the Voyager 1 that went up to higher latitudes for the period 1985-1990. However, there are other shorter-term periods where the model and observations disagree.

Zooming in on the period of interest (1985-1990), the Voyager 2 measurements from the year $\sim$ 1987 to $\sim$1991 shows a steady increase in solar activity (a decrease in the measured intensities) while for Voyager 1 from $\sim$ 1987 - 1989 a flat intensity profile was observed, shown in the bottom panel of Figure 5.2. As mentioned before the computed 2.5 GV intensities are produced using the modified compound approach of Manuel [2012] and Manuel et al. [2014], with time-dependent functions $f_1(t)$, $f_2(t)$ and $f_3(t)$ as discussed in Chapter 4, see Equations 4.16, 4.9 and 4.15. The corresponding parameters used for optimal reproducing of the cosmic ray profiles along Voyager 1 are: $r_{hp} = 122$ AU, $r_{ts} = 90$ AU, $a = 0.02$, $b = 0.01$, $K_{A0} = 0.75$, $C_1 = 3.0$, $C_2 = 0.8$, and $s = 3.0$; and along Voyager 2 are: $r_{hp} = 100$ AU, $r_{ts} = 80$ AU, $a = 0.017$, $b = 0.01$, $K_{A0} = 0.9$, $C_1 = 4.0$, $C_2 = 0.7$, and $s = 3.0$.

Shown in this figure is that along the Voyager 2 trajectory, the model results are generally in good agreement with Voyager 2 observations, with the computed intensities following the increase in the observations from $\sim$ 1985 - 1987.5 (solar minimum). However, from $\sim$ 1980 - 1985 the model of Manuel et al. [2014] is below the observed intensities and this is something that needs to be addressed. Along the Voyager 1 trajectory both the model and observations increase to $\sim$ 1987.5, but during this period the model stays below the observations up to extreme solar minimum. The observed intensities show a flat intensity profile from $\sim$ 1987 - 1989 while the model shows a peak instead.

To investigate whether this feature may be unique for the $E > 70$ MeV channel, measurements from two other energies are also investigated. Shown in Figure 5.3 are the Voyager 1 and 2 proton cosmic ray intensity measurements at different energies, i.e. 30 - 69 MeV shown by the red line and 133 - 242 MeV shown by the black line. For both these energy ranges, Voyager 1 observations show a flat intensity profile from $\sim$ 1987.5 - 1989, while Voyager 2 measurements have a peak-like intensity profile around $\sim$ 1987.5. The measured intensity profile for these energy ranges are similar to those for the $E > 70$ MeV for the period of interest for both Voyager 1 and 2 as shown in the bottom panel of Figure 5.2. Interestingly however is that for the observed 30 - 69 MeV protons along the Voyager 1 trajectory, the intensity profile is less flat compared to that of higher energies, e.g. energies at 133 - 242 MeV and $E > 70$ MeV protons.

This incompatibility, where Voyager 1 observations stayed flat around solar minimum while the model calculated a peaked-intensity profile, is the main topic of this and the next chapter. It was the aim of this work to propose a refinement of the model to compute improved compatibility for this period. The model used by Manuel et al. [2014] uses various modulating parameters (i.e. solar wind speed, tilt angle and heliospheric magnetic field) as input

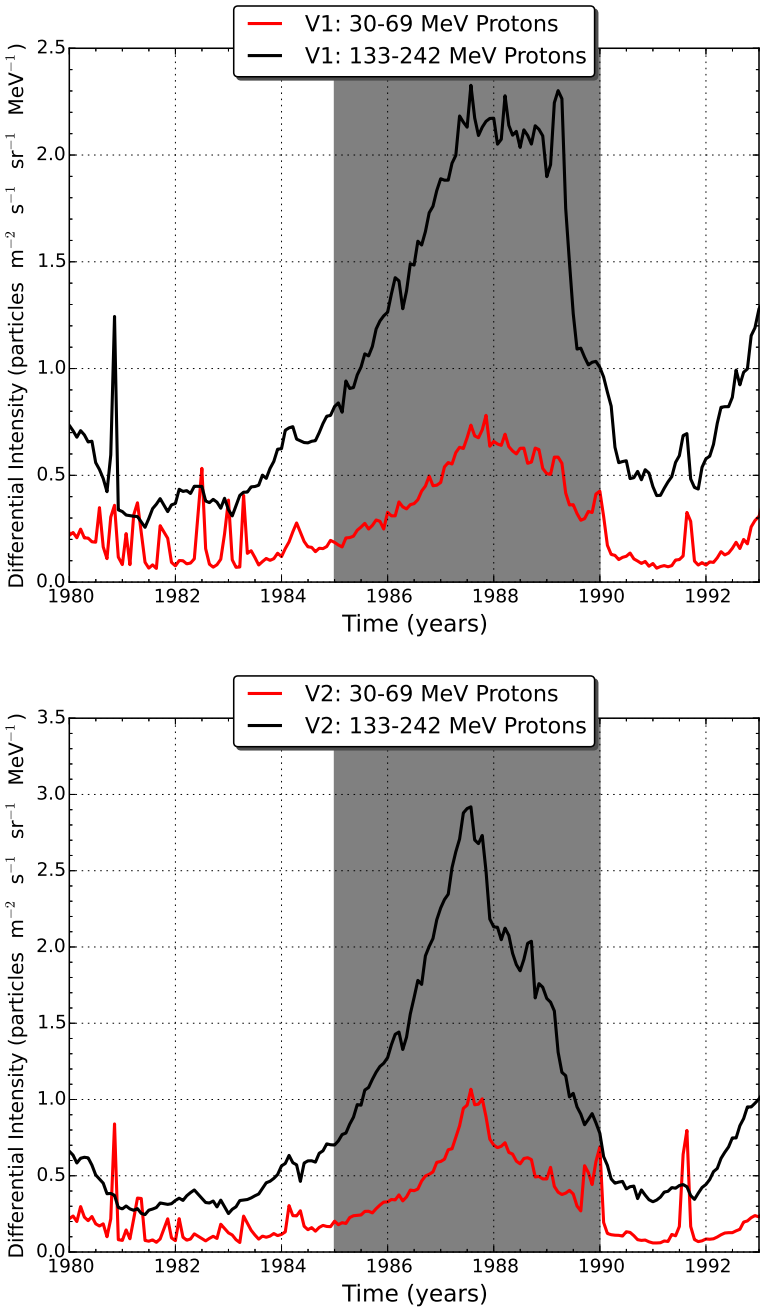

FIGURE 5.3: The proton cosmic ray observations from the Voyager 1 (top panel) and 2 (bottom panel) spacecraft in the energy range of 30 - 69 MeV and 133 - 242 MeV. The shaded areas show the period of interest in this chapter. Data from *http* : *//voyager.gsfc.nasa.gov*.

parameters to calculate cosmic ray modulation. As a first approach, these parameters are now investigated to establish possible reasons for this incompatibility.

5.3 Observed Modulation Parameters for the 1985 - 1990 period

As shown in Figure 5.1, Voyager 1 moved to higher latitudes while Voyager 2 stayed close to the equatorial plane in the same hemisphere during the period of interest. This section investigates if there are any differences in the solar wind speed, HMF, HCS tilt angle and the coronal magnetic field between the two hemispheres of the heliosphere for this period.

As mentioned before, all solar cycle related changes are embedded in the radially outward propagating solar wind plasma that is radial up to the termination shock. The solar wind speed measured by Voyager 1 and 2 as a function of time is shown in Figure 5.4. Also shown is the Omni_M solar wind speed observations at Earth (1 AU).

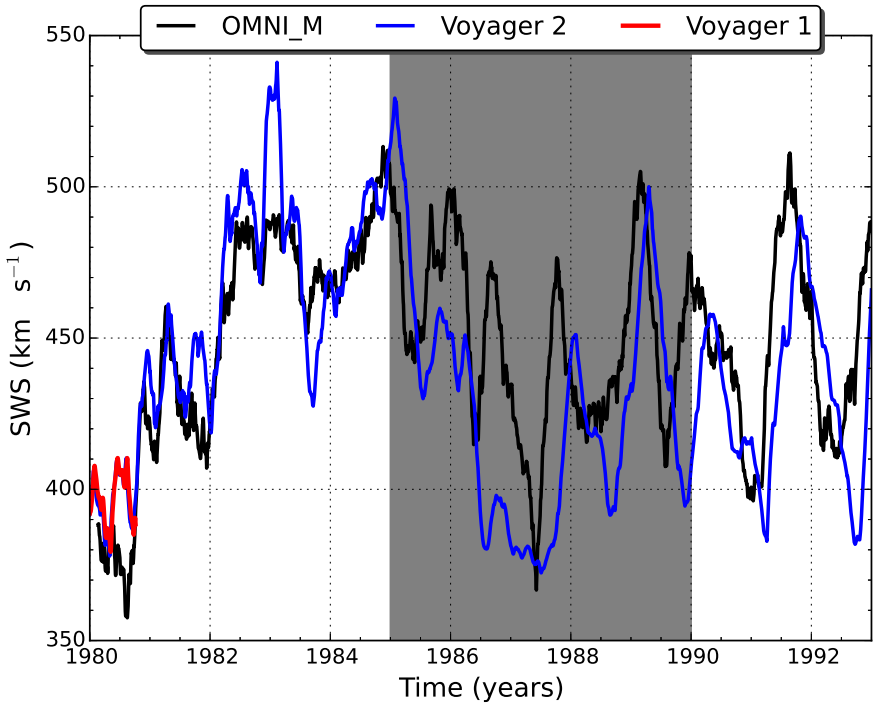

FIGURE 5.4: Daily averaged solar wind plasma speed measured by the Voyager 1 and 2 spacecraft as a function of time. Also shown is the Omni_M solar wind speed measurements at the Earth (1 AU) and the shaded area show a period of interest in this chapter. Data from *http://omniweb.gsfc.nasa.gov/coho/*.

A comparison between the solar wind speed measured by Voyager 1 and 2 spacecraft is not possible because Voyager 1 measurements are available only up to $\sim$ 1981 due to the plasma detector that has stopped working ever since. But the Voyager 2 measurements can be compared to the Omni_M data as shown in Figure 5.4. Note that for this period Voyager 2 was at $\sim$ 15 AU from the Sun in 1985 and $\sim$ 32 AU in 1990 and with an average solar wind speed of 450 km.s^{-1}, which roughly gives about $\sim$ 2.2 months propagation time from 1985 - 1990. Note that this propagation time is not corrected for in the Omni_M data, but should be kept

in mind when comparing Voyager 1, Voyager 2 and Earth measurements as in Figure 5.4. Apart from the obvious phase difference, the figure shows that Voyager 2 and Omni_M have the same trend on a global scale, with the only notable difference at $\sim 1986 - 1987$ when Voyager 2 observations decreased while Omni_M observations increased. However, this is over a relatively short period, so that Figure 5.4 suggests, from a solar wind speed perspective, that, apart from the year $\sim$ 1986 - 1987, there's nothing unexpectedly different on a global scale when comparing Voyager 2 and Omni_M data.

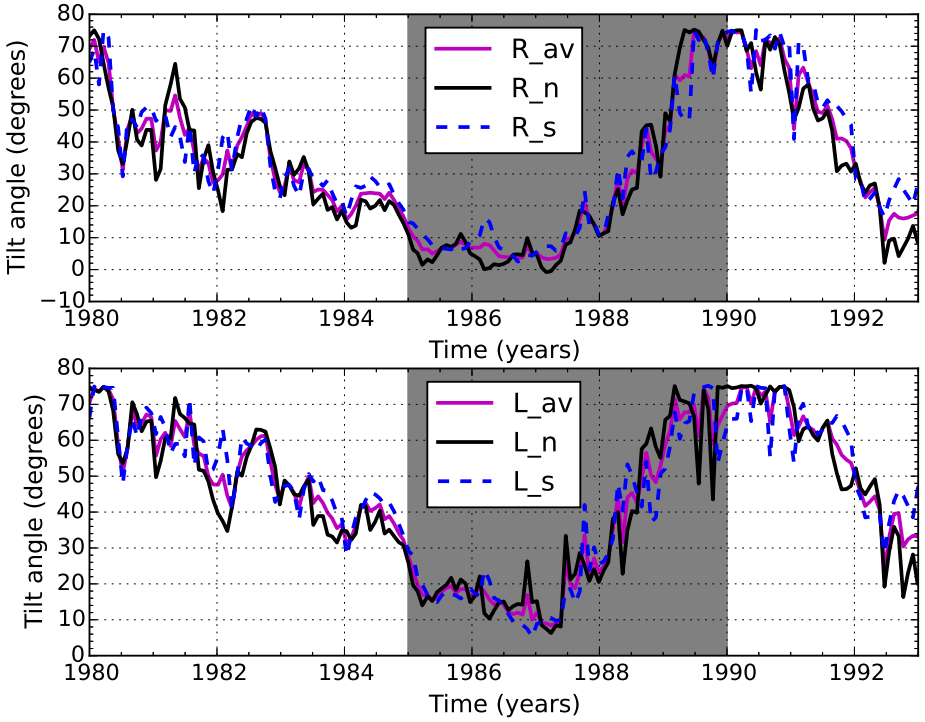

FIGURE 5.5: HCS tilt angles based on two different calculation methods, 'R' and 'L', are shown for the two solar hemispheres, i.e. 'n' for north and 's' for south. The shaded areas show the period of interest in this chapter. Data from $http://wso.stanford.edu/Tilts.html$.

One of the four major modulation processes is particle drifts and as discussed before, cosmic rays respond to changes in the HCS tilt angle, especially at solar minimum conditions. The tilt angle is a proxy for solar activity and is anti-correlated to the cosmic ray modulation cycle. The tilt angle, as computed over the two hemispheres by two different methods (see $http://wso.stanford.edu/Tilts.html$ for further discussion), is shown in Figure 5.5 as a function of time. The two methods are the classic "line-of-sight" model denoted by L and the newer radial model denoted by R. For both models the northern and southern hemisphere values are shown, which are denoted by 'n' and 's' respectively, together with the average values indicated by 'av'.

It follows from the figure that these tilt angle values are quite similar for both hemispheres and for both L and R models. Only small differences exist on a scale of a few months and

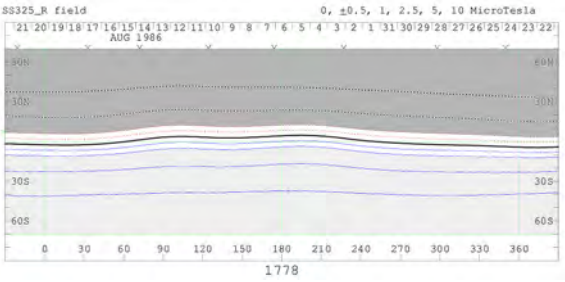

(A) August 1986

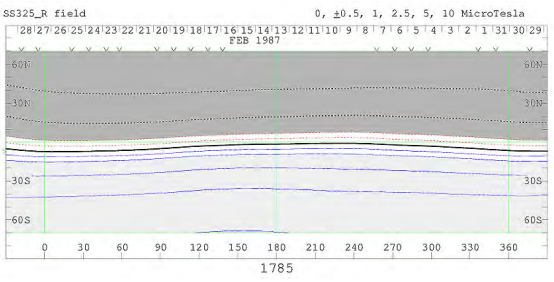

(B) February 1987

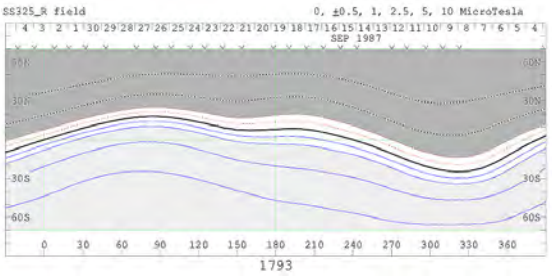

(C) September 1987

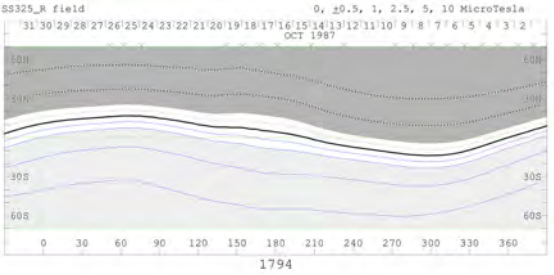

(D) October 1987

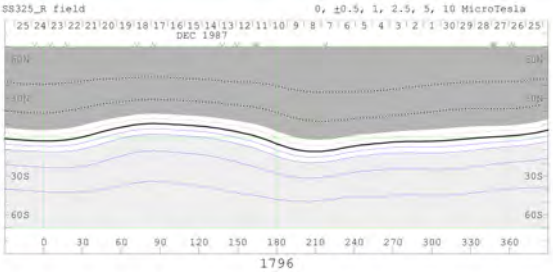

(E) December 1987

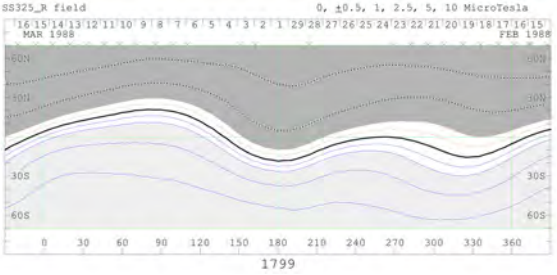

(F) March 1988

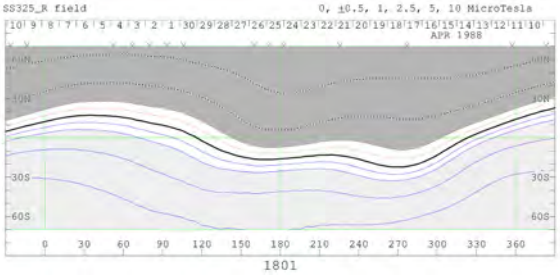

(G) April 1988

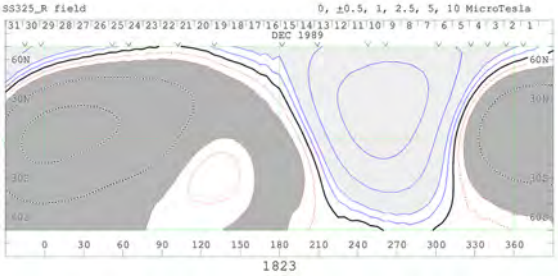

(H) December 1989

FIGURE 5.6: Contour plots of the coronal magnetic field computed using the Potential Field Source Surface model with a source surface at $3.25r_{\odot}$. These contour plots are shown for different Carrington rotations. The thick solid black line corresponds to the neutral line and the dark grey area is the solar hemisphere where the field lines are pointing towards the Sun and the light grey area the solar hemisphere where the field lines are pointing away from the Sun. From *http* : *//wso.stanford.edu*.

not global differences, as would be needed to explain a possible asymmetry in the modulation conditions between the Voyager 1 and 2 trajectories at different latitudes, which may cause the incompatibility as discussed above.

Figure 5.6 shows the coronal maps of the solar polar magnetic field strength and the polarity

in the northern and southern hemispheres for different Carrington rotations (CRs). The maps shown here cover the period in question. Panel (A) corresponds to August 1986 CR 1778; Panel (B) to February 1987 CR 1785; Panel (C) to September 1987 CR 1793; Panel (D) to October 1987 CR 1794; Panel (E) to December 1987 CR 1796; Panel (F) to March 1988 CR 1799; Panel (G) to April 1988 CR 1801 and Panel (H) to December 1989 CR 1823. These maps are an indication of the magnetic field environment, especially the form of the HCS in which cosmic rays are modulated.

From Figure 5.6 it follows that panel (A) for CR 1778 corresponds to a solar minimum period (August 1986), during which the HCS was relatively flat as shown by the thick solid black line, indicating a small tilt angle. Evidently, this thick solid black line begins to meander with time and shift further from the horizontal solid green line at 0°, which is an indication of an increasing solar activity. Panel (H) for CR 1823 corresponds to an increased solar activity period (December 1989) because the solid black line, which is an indicative of the HCS, is greatly curved and varied from the horizontal green line, indicating large tilt angles and magnetic field busy times.

Comparing all these coronal maps reveals nothing extraordinary except that the current sheet is slightly asymmetric about the equator and that this might result in the cosmic ray modulation asymmetry between the north and the south solar poles [see e.g. Hattingh et al., 1997, Smith et al., 2000, Erdos and Balogh, 2010]. However, the association of north-south asymmetry with displacement of the HCS is still under much scrutiny to determine whether such observation is indeed related to the displacement of HCS or to an asymmetrical magnetic flux [Potgieter, 2013*b*]. However, the observed differences between Voyager 1 and 2 measurements for the period 1985 - 1988 are unlikely to be explained by the observed asymmetry of the HCS because for this period both Voyager 1 and 2 spacecraft were sampling the same hemisphere but far apart from each other in heliolatitude (see Figure 5.1).

Embedded in the outward propagating solar wind is the HMF which plays a crucial role in cosmic ray modulation. The Voyager spacecraft's HMF magnitude measurements plotted as a function of time is shown in Figure 5.7. Also shown are the Omni_M observations at Earth (at 1 AU). As discussed above there is an expected phase difference in the measured intensities between the different spacecraft measurements due to their different radial and latitude positions. There is a difference in radial distance of $\sim$ 7 AU between Voyager 1 and 2 at 1988.

It follows from Figure 5.7 that Voyager 2 measurements of the HMF magnitude in the equatorial region are higher than Voyager 1 measurements at higher latitudes as expected if a Parker HMF model is assumed. For the shaded area the HMF values measured by both Voyager 1 and 2 decreases from $\sim$ 1985 up to $\sim$ 1987, afterwards the values increase again towards solar maximum. The Omni_M HMF values at Earth (1 AU) decrease as well for the shaded area from $\sim$ 1985 up to $\sim$ 1987 as the Voyager 1 and 2 HMF measurements do and begin

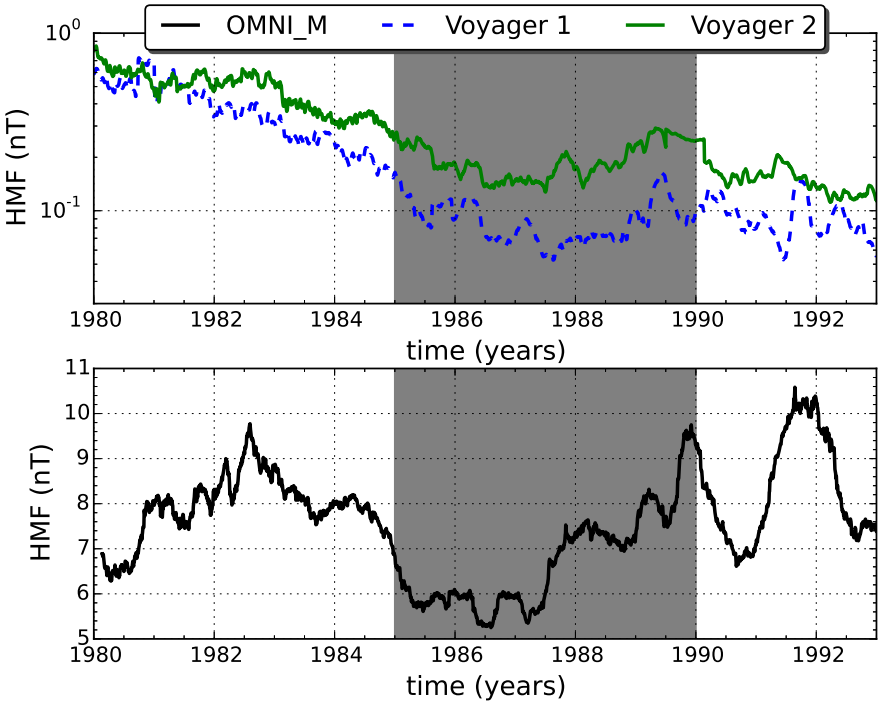

FIGURE 5.7: Top panel: Shows on a logarithmic scale daily averaged HMF magnitude as measured by the Voyager 1 and 2 spacecraft as a function of time. Bottom panel: Shows on a linear scale the Omni_M data at the Earth (1 AU). The shaded areas show a period of interest in this chapter. Data from *http* : *//omniweb.gsfc.nasa.gov/coho/*.

to increase towards solar maximum. Voyager 1 and 2 HMF values decrease with increasing radial distance while the Omni_M measurements have an average value of $\sim$ 5.5 nT during solar minimum and an average of $\sim$ 10.5 nT during solar maximum. The conclusion can be made that since some small differences in a period of a few months exist, there are no global differences which may suggest different modulation conditions between Voyager 1 and 2 for the period of interest.

5.4 Summary and Conclusions

In previous work, a well established 2D time-dependent cosmic ray modulation model including the modified compound approach of Manuel et al. [2014] was utilized to calculate cosmic ray intensities along Voyager 1 and 2 trajectories. It was found that the model is compatible with observations on a global scale, however for the period 1985 - 1990 which corresponds to a solar minimum period, the computed intensities along the Voyager 1 trajectory were not compatible with observations. For this period the model computed a peak-like intensity profile while observations showed a plateau-like intensity profile along Voyager 1 trajectory, but along the Voyager 2 trajectory observations and model results are in good agreement.

For this period Voyager 1 went up to high latitudes in the northern hemisphere while Voyager 2 stayed near the equatorial region. Along their trajectories they experienced different modulation conditions. Different modulation parameters utilized as input parameters in the model were investigated in this chapter to establish possible reasons for the differences between Voyager 1 and 2 cosmic ray measurements and also incompatibility between Voyager 1 observations and model calculations. It was shown that, even though some small differences of a few months between these parameters exist, these type and scale of differences are not enough to account for the differences between Voyager 1 and 2 measurements for the period of interest. In the next chapter a refinement of the modified compound approach is rather proposed.

Chapter 6

Modelling the 1985 - 1990 period of cosmic ray intensities along Voyager spacecraft trajectories

6.1 Introduction

It was mentioned in the previous chapter that a refinement of the modified compound approach of Manuel et al. [2014] is necessary to increase compatibility with observations, especially for the case of the Voyager 1 observations for the period 1985 - 1990. It is shown in this chapter that, for the modified compound approach, a time-dependent drift coefficient played an important role during the solar minimum conditions in the mid 1980s. A modification to the time-dependent function, that scales drifts as a function of solar activity, is proposed for this period. This leads to an improved compatibility between Voyager 1 observations and model results for the 1985 - 1990 period.

6.2 Original Compound and Modified Compound Model

Before re-visiting the time-dependence of the transport coefficients, as in the modified compound approach, it is important to determine which transport coefficient (drifts or diffusion) may be dominant and over what level of solar activity this might be the case for the particular period of interest in this chapter. This is done by investigating the individual contributions of the transport coefficients to the total modulation of cosmic ray intensities over a solar cycle by varying the manner in which they depend on time. Figures 6.1 and 6.2 show model results corresponding to different scenarios (as discussed below) along the Voyager 1 and 2 trajectories respectively. The top panel of each figure shows model results computed using the original compound approach of Ferreira and Potgieter [2004] with the time-dependent scaling of drifts over a solar cycle using the refinement proposed by Magidimisha [2011]. The bottom panel of the figure is computed using the modified compound approach of Manuel et al. [2014]. Shown

also for comparison are $E > 70$ MeV cosmic ray proton observations from the Voyager 1 and 2 spacecraft.

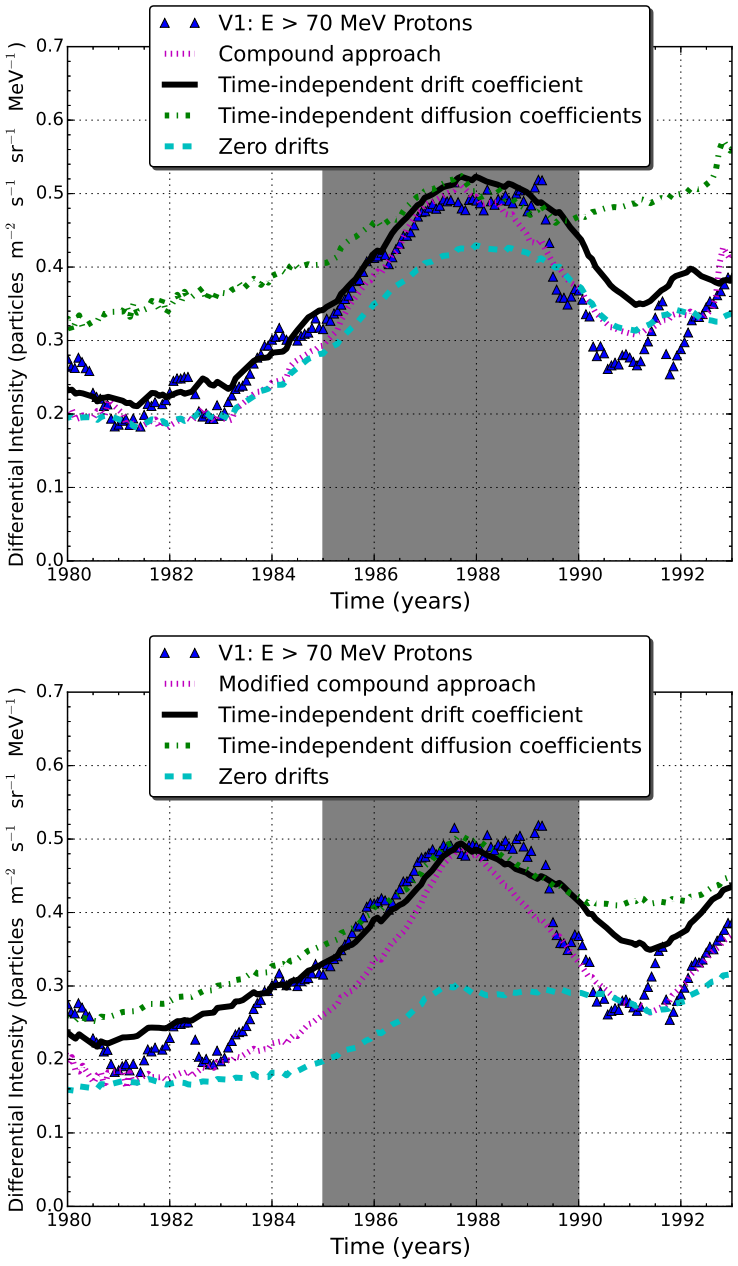

FIGURE 6.1: Shown in the top panel are the computed 2.5 GV cosmic ray proton intensities using the original compound approach of Ferreira and Potgieter [2004] and the bottom panel using the modified compound approach of Manuel et al. [2014]. Calculations are along the Voyager 1 trajectory. Three scenarios corresponding to: (1) time-independent drift coefficient; (2) time-independent diffusion coefficients; and (3) zero drifts, are shown as indicated in the label. Also shown are $E > 70$ MeV cosmic ray proton observations from the Voyager 1. Data from *http* : *//voyager.gsfc.nasa.gov*.

The first computed scenario in Figures 6.1 and 6.2, which is shown by the black solid lines, corresponds to time-dependent cosmic ray intensities computed by assuming a time-independent drift coefficient, e.g. $f_1(t) = 0.7$, in Equation 4.3 for the original compound approach and in Equation 4.16 for the modified compound approach. For this scenario drifts are changing

over a solar cycle via changes in the tilt angle but the drift coefficient itself is not. For the second scenario, shown by the green dash-dot line, the time-dependence in the drift coefficient over a solar cycle is implemented but now with time-independent diffusion coefficients, e.g. $f_2(t) = f_3(t) = 1.0$, in Equations 4.9 and 4.15. For the third scenario, shown by the cyan dashed line, diffusion coefficients are scaled time-dependently over a solar cycle (according to Equations 4.9 and 4.15) but now with drifts turned off (i.e. $f_1(t) = 0.0$). The results of the compound approach of Ferreira and Potgieter [2004] (denoted 'Compound Approach') and the modified compound approach of Manuel et al. [2014] (denoted 'Modified Compound Approach'), as discussed in Chapter 4, are also shown by the magenta dotted lines for comparison.

It follows from the top panel of Figure 6.1 that for the traditional compound approach along the Voyager 1 trajectory, for the first scenario (solid black line), the model gives compatibility with observations for most of the period. However, during increasing solar activity from $\sim$ 1989 onwards, the model gives cosmic ray intensities that are above the observed intensities. For this scenario the drift coefficient is not changing over time, therefore resulting in a smaller total variation between solar minimum and solar maximum. The modified compound approach (shown in the bottom panel) computed intensities which are slightly less sensitive to changing modulation conditions. For this scenario, the computed total variation between solar minimum and solar maximum is smaller for the modified compound approach. For the modified compound approach, the time-dependent changes in the diffusion coefficients between solar minimum and solar maximum are less pronounced compared to the original compound approach.

This feature is more evident in the second scenario (shown by dash-dot green line), where it is assumed that the drift coefficient changes over time, but all diffusion coefficients (i.e. parallel and perpendicular) are kept constant over a solar cycle. As expected, apart from extreme solar minimum conditions, both original and modified compound approaches compute incompatibility along the Voyager 1 trajectory for this scenario. The compound approach shows a weak solar cycle response, whereas the modified compound approach gives intensities changing somewhat over a solar cycle. For the third scenario (dashed cyan line), where drifts are switched off, the differences between the two approaches are highlighted. The modified compound approach shows almost no response to the solar cycle compared to the compound approach which shows a much larger total variation between solar minimum and solar maximum when drifts are switched off. Along the Voyager 2 trajectory shown in Figure 6.2, similar conclusions can be made.

To be more specific about the individual contributions of the time-dependent functions used in the compound approach of Ferreira and Potgieter [2004] and the modified compound approach of Manuel et al. [2014] shown in Figures 6.1 and 6.2, solar minimum is chosen at 1988 and solar maximum at 1991. It follows that along the Voyager 1 trajectory from Figure 6.1 for the results

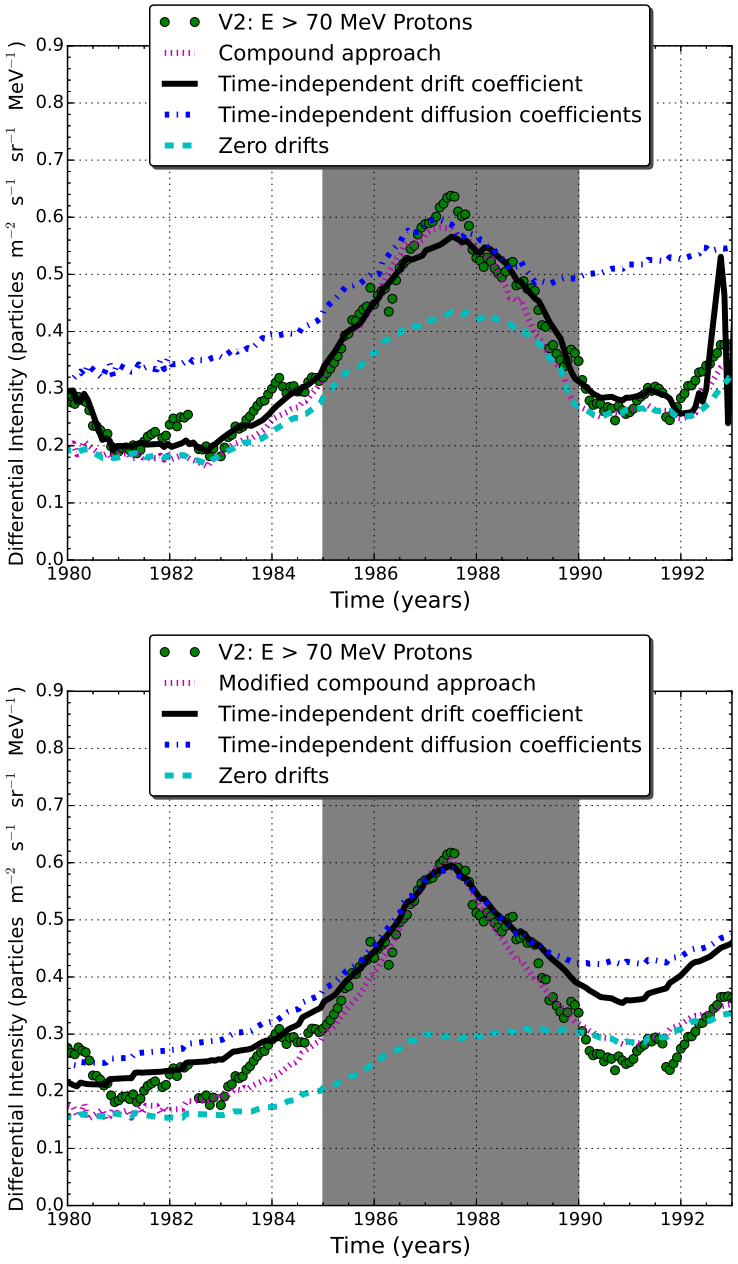

FIGURE 6.2: Similar to Figure 6.1 but along the Voyager 2 trajectory.

shown in the top panel, the total variation between solar minimum and solar maximum changes as follows: solar maximum is 40.0% lower than solar minimum for the compound approach, 31.4% lower for the first scenario, 4.0% lower for the second scenario and 27.3% lower for the third scenario. For the results in bottom panel, the resulting total variation between solar minimum and solar maximum is 44.0% lower for the modified compound approach, 28.0% lower for the first scenario, 16.0% lower for the second scenario and 6.7% lower for the third scenario. Along the Voyager 2 trajectory shown in Figure 6.2, in the top panel, the total variation between solar minimum and solar maximum is 55.2% lower for compound approach, 48.3% lower for the first scenario, 13.8% lower for the second scenario and 33.3% lower for the third scenario. In the bottom panel, the total variation between solar minimum and

solar maximum is 50.0% lower for the modified compound approach, 40.0% lower for the first scenario, 30.0% lower for the second scenario and 6.7% lower for the third scenario.

Comparing the two approaches quantitatively, it follows that the modified compound approach gives a smaller total variation between solar minimum and solar maximum for the third scenarios (the non-drift case), along the Voyager 1 and 2 trajectories. But for the second scenario (time-independent diffusion coefficients) the traditional compound approach gives a smaller total variation between solar minimum and solar maximum when compared to the modified compound approach. For the first scenario (time-independent drift coefficient) it follows that the modified compound approach gives a smaller total variation when compared to the traditional compound approach. These time-dependent functions are discussed and shown in the figure below.

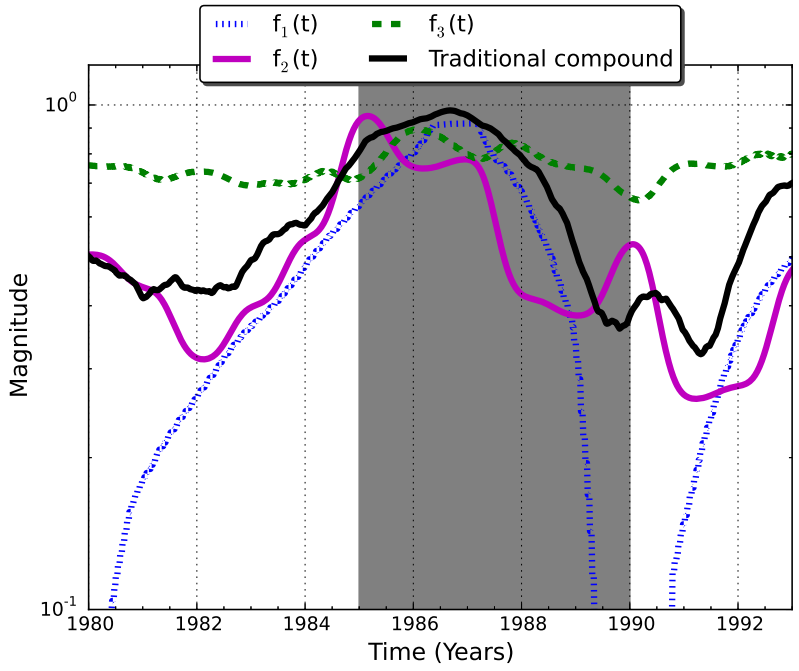

FIGURE 6.3: The time-dependent functions $f_1(t), f_2(t)$ and $f_3(t)$ given by Equations 4.16, 4.9 and 4.15 respectively. The time-dependence for the diffusion coefficients in the compound approach is given by Equations 4.1 and 4.2.

Shown in Figure 6.3 are: the time-dependent function $f_1(t)$ (shown by the blue dotted line) as given by Equation 4.16 for the drift coefficient, $f_2(t)$ (shown by the magenta solid line) as given by Equation 4.9 for the parallel diffusion coefficient and $f_3(t)$ (shown by the green dashed line) as given by Equation 4.15 for the perpendicular diffusion coefficients. These are used in the modified compound approach of Manuel et al. [2014]. Also shown is the time-dependent function given by Equations 4.1 and 4.2 which is the time-dependent function for the diffusion coefficients used by Ferreira and Potgieter [2004] in the compound approach as shown by the black solid line. The time-dependent drift function for this approach is the same as $f_1(t)$ as proposed by Magidimisha [2011]. The figure shows that $f_1(t)$ has a maximum value of ~ 0.9 during solar minimum and very small values during solar maximum, $f_2(t)$ has a maximum of

~ 0.95 during solar minimum and minimum value of ~ 0.3 during solar maximum and $f_3(t)$ has a maximum value of ~ 0.9 during solar minimum and minimum value of ~ 0.65 during solar maximum. The function of Ferreira and Potgieter [2004] reaches a maximum value of $\sim$ 1.0 during solar minimum and a minimum value of ~ 0.3 during solar maximum. Noticeable is that the amplitude of time-dependence in the original compound approach for diffusion coefficients is larger compared to that of the modified compound approach for perpendicular diffusion coefficient. For the latter, model computations using this approach show to be much more sensitive to changes in the tilt angle and scaling of drifts over a solar cycle.

Comparing Figures 6.1 and 6.2 shows that the original compound approach for the period of interest results in model solutions which are more compatible to observations along the Voyager 1 trajectory compared to the modified compound approach. The original compound approach produces a flatter intensity profile than the modified compound approach due to its particular dependence on the magnetic field magnitude. For Voyager 2 it is the opposite, with the modified compound approach giving optimal compatibility with observations. Here the original compound approach also gives a flat intensity profile while Voyager 2 observations show a peaked-intensity profile. Note that observations at Earth, e.g. Figure 2.13, shows a similar peaked profile for this period. This peaked-intensity profile indicates that, in the original compound approach, the sensitivity of the diffusion coefficients to changes in the magnitude of the HMF could be over-estimated. A possible weaker dependence on HMF for this approach could result in improved compatibility. However, this work now continues to propose a modification to the modified compound approach of Manuel et al. [2014] to improve compatibility with observations.

6.3 Particle Drift Effects

As previously discussed, one of the four major mechanisms determining the global modulation of galactic cosmic rays in the inner heliosphere, are the gradient, curvature and HCS particle drifts. These are more effective during solar minimum periods [e.g. le Roux and Potgieter, 1992] as compared to solar maximum periods. The period of interest for this chapter occurs during an A < 0 HMF polarity when positively charged particles drift inward into the heliosphere along the HCS, so that their intensity is more sensitive to changes in tilt angle α.

As shown in Figure 5.1 Voyager 2 stayed close to the equatorial regions and measured a peak-like intensity profile at $\sim$ 1987.5 as expected during an A < 0 solar minimum activity period. As shown in Figure 6.2 for the period of interest, i.e. 1985 - 1990, the modified compound model agrees with Voyager 2 measurements. However, for Voyager 1 which travelled out of the ecliptic plane, it measured a more plateau-like intensity profile for 1987 - 1989 period while the modified compound model computed a peak-like intensity profile at $\sim$ 1987.5 as shown in Figure 6.1.

As mentioned in the previous chapter the time-dependence in the drift coefficient (Equation 4.17) for the modified compound approach is given by:

$$f_1(t) = 0.013 \times \frac{(75.0^\circ - \alpha(t))}{\alpha_c}, \tag{6.1}$$

which is a time-varying function that utilizes the tilt angle α as a time-dependent input parameter depending on the solar activity. This function is used to scale K_A for increasing solar activity to almost $\sim 0\%$ for solar maximum conditions, but increases the drift effects to $\sim 90\%$ for solar minimum conditions [Manuel et al., 2011*b*, Manuel, 2012]. Figure 6.4 shows the behaviour of this time-dependent function compared with the tilt angle. Shown in this figure is that the time-dependent function increases with decreasing tilt angle, thus implying increased drift effects of particles during solar minimum conditions and decreased drift effects during solar maximum conditions. The highlighted area in Figure 6.4 shows the effectiveness of particle drift effects between $\sim$ 1985 and $\sim$ 1987 where-after solar activity started to increase to $\sim$ 1990.

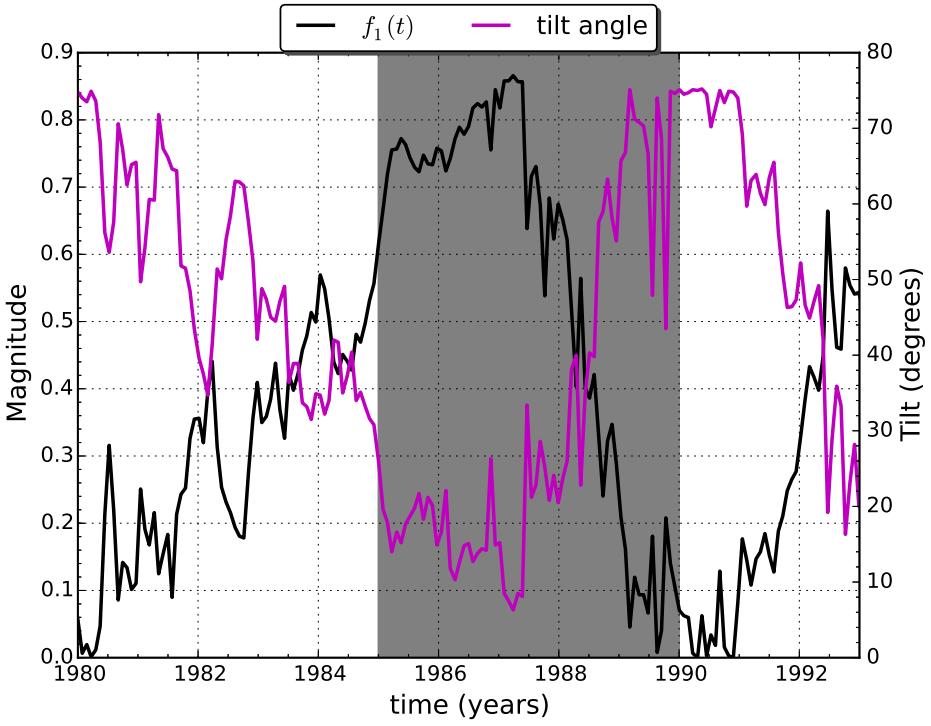

FIGURE 6.4: Time-dependent function $f_1(t)$ given by Equation 4.16 and the L_n model of the tilt angle in the northern hemisphere with the appropriate scale displayed on the right side. Data from *http* : *//wso.stanford.edu/Tilts.html*.

It was shown in the bottom panel of Figure 6.1 that, when the drift coefficient is not scaled time dependently over a solar cycle, a flatter profile is computed which is more compatible with observations. This aspect is now explored further in the model with the time-dependent function in Equation 4.16 switched off (i.e. $f_1(t) = 1.0$). This means that the drift coefficient

is not scaled time-dependently over a solar cycle as implemented through Equation 4.16. The drift coefficient, however, depends on the HMF magnitude which changes over time, and hence, the drift coefficient will still have a time dependence, even if the scaling function over a solar cycle is switched off. Therefore, drift effects are changing over a solar cycle due to changes in the tilt angle but also the HMF in the drift coefficient.

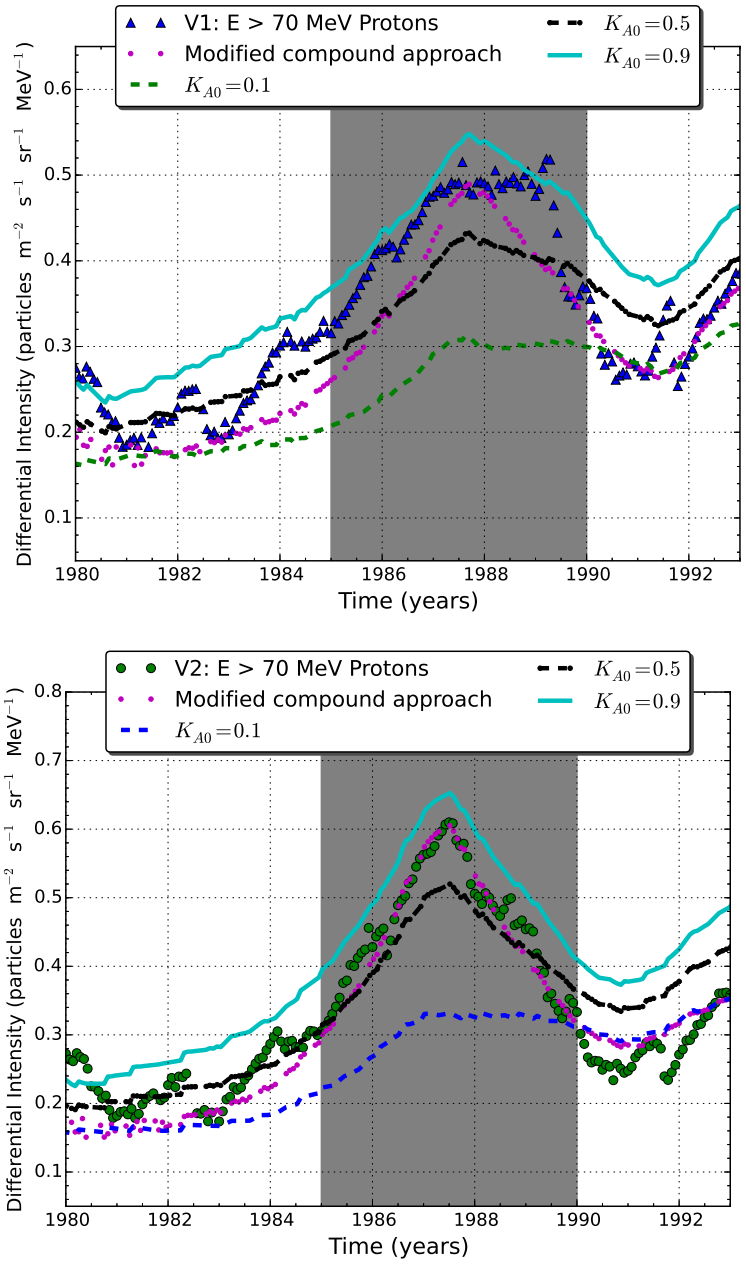

FIGURE 6.5: The top panel shows the computed 2.5 GV cosmic ray proton intensities along the Voyager 1 trajectory and the bottom panel shows computations along the Voyager 2 trajectory. Three scenarios are computed corresponding to: (1) $K_{A0} = 0.1$; (2) $K_{A0} = 0.5$; and (3) $K_{A0} = 0.9$, for time-independent drift coefficient. Also shown are the $E > 70$ MeV proton observations from the Voyager 1 and 2. Data from *http* : *//voyager.gsfc.nasa.gov*.

Shown in Figure 6.5 are computed intensities corresponding to different K_{A0} values when $f_1(t) = 1.0$. Results are shown along the Voyager 1 and 2 trajectories in the top and bottom

panel, respectively. Along the Voyager 1 trajectory the green dashed line corresponds to $K_{A0} = 0.1$, the black dot-dash line corresponds to $K_{A0} = 0.5$ and the cyan solid line corresponds to $K_{A0} = 0.9$ and along the Voyager 2 trajectory the blue dashed line corresponds to $K_{A0} = 0.1$, the black dot-dash line corresponds to $K_{A0} = 0.5$ and the cyan solid line corresponds to $K_{A0} = 0.9$. Shown by the magenta dotted lines are the modified compound approach calculations with $f_1(t) \neq 1.0$ and $K_{A0} = 0.75$ (as discussed previously). Also shown are $E > 70$ MeV proton observations from the Voyager 1 and 2 spacecraft.

Along the Voyager 1 and 2 trajectories, $K_{A0} = 0.1$ leads to intensities which are less sensitive to solar cycle related changes when compared to observations. Compared to the modified compound approach, scenarios $K_{A0} = 0.5$ and $K_{A0} = 0.9$ gives a flatter intensity profile for Voyager 1 but still results in a peaked intensity profile for Voyager 2. As expected, the computed modulation variation is smaller than observed between solar minimum and solar maximum. It follows from this figure (where $f_1(t) \neq 1.0$) that this function as is incorporated in the model gives the peaked intensity profile along both the Voyager 1 and 2 trajectories. It seems that in order to compute a flatter profile along Voyager 1 trajectory, a modification on how $f_1(t)$ is implemented in the model needs to be made.

6.4 Changes to the Modified Compound Approach

Figure 6.6 shows the latitude of Voyager 1 and 2 as a function of time. Also shown is the L_n and L_s values of the L model of the tilt angle in the northern and southern hemispheres, respectively. In 1985 Voyager 1 was at 22 AU and Voyager 2 at 15 AU, therefore assuming a wind speed of 450 km.s^{-1}, the tilt angle data at 22 AU should be adjusted by ~ 2.3 months along the Voyager 1 trajectory and by ~ 1.6 months along the Voyager 2 trajectory.

Comparing both the Voyagers' latitudinal position with the HCS latitudinal extent, indicates that while the HCS tilt angle was decreasing, Voyager 2 stayed in the equatorial region and always inside the HCS region while Voyager 1 went to higher latitudes, even above the HCS region between $\sim$ 1985 and $\sim$ 1988 as shown in Figure 6.6. This means that for a period of over ~ 3 years, Voyager 1 was outside the latitudinal extent of the HCS region. This period corresponds to the time when Voyager 2 measured the expected peaked-like intensity profile while Voyager 1 measured a flat-like intensity profile for this particular polarity cycle.

Figure 6.6 indicates that Voyager 1 may have experienced different conditions when outside the latitudinal extent of the HCS region compared to Voyager 2. This is now investigated in the model by modifying the implementation of the time-dependence of the drift coefficient to be different inside and outside the HCS regions. Figure 6.7 shows a schematic diagram of a 2-D projection of the HCS region. Shown in this figure for calculations to follow is that inside the HCS region the drift coefficient scales according to the time-dependent function $f_1(t)$

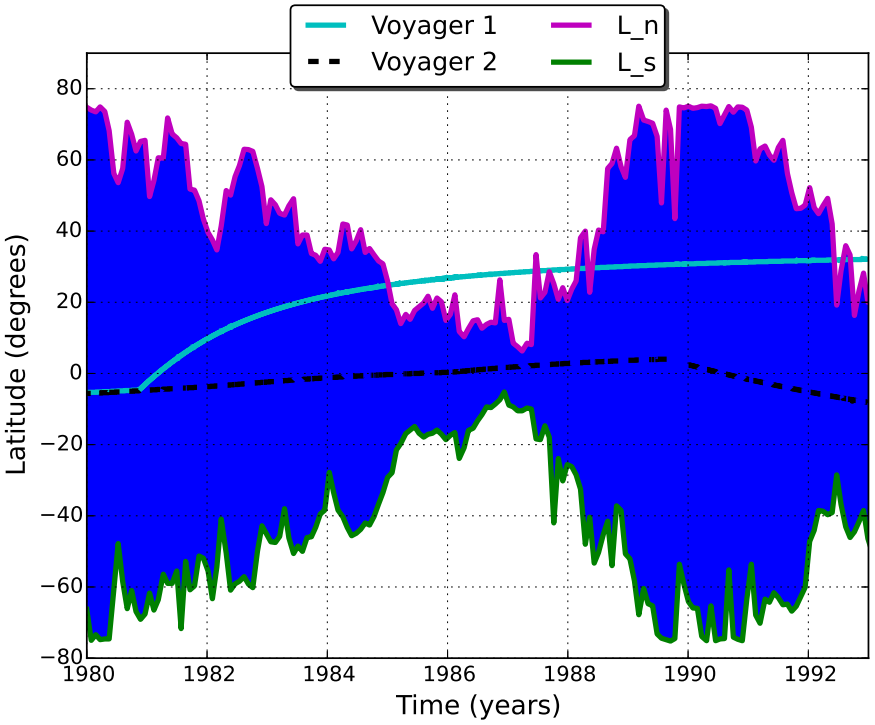

FIGURE 6.6: The latitude of Voyager 1 (solid cyan line) and Voyager 2 (dashed black line) as a function of time. Also shown are the values of the L model of the tilt in the northern (L_n) and southern (L_s) hemispheres as a function of time. The area shaded blue is the region inside the latitudinal extent of the HCS region.

given by Equation 4.16, but at latitudes above and below the HCS region the time-dependent scaling of the drift coefficient is switched off, i.e. $f_1(t) = 1.0$. However, comparison between Equations 3.31 and 3.32 imply that the time-dependence scaling of the drift coefficient K_A by the time-dependent function $f_1(t)$, given by Equation 4.16, is only applied to the gradient and curvature part, while the HCS part is unaffected.

This is explored further in Figure 6.8. This figure shows the computed 2.5 GV cosmic ray proton intensities along both Voyager 1 (top panel) and Voyager 2 (bottom panel) trajectories using the modified compound approach of Manuel et al. [2014]. Calculations in this figure are done with the time-dependent changes of the drift coefficient switched off ($f_1(t) = 1.0$) above a certain latitude $\acute{\theta}$, in this case $\acute{\theta} > 20°$ (shown by the green dashed line), $\acute{\theta} > 40°$ (shown by the black solid line) and $\acute{\theta} > 60°$ (shown by dash-dot red line) along the Voyager 1 trajectory and along the Voyager 2 trajectory $\acute{\theta} > 20°$ (shown by the blue dashed line), $\acute{\theta} > 40°$ (shown by the black solid line) and $\acute{\theta} > 60°$ (shown by dash-dot red line). Also shown as the cyan solid line are results with $f_1(t) = 1.0$ above the tilt of the current sheet, i.e. $f_1(t) = 1.0$ when $\acute{\theta} > \alpha$. The modified compound approach results are shown by the magenta solid line. Proton cosmic ray observations with $E > 70$ MeV are also shown for comparison.

Calculations along the Voyager 1 trajectory in Figure 6.8 with $f_1(t) = 1.0$ when $\acute{\theta} > 20°$ show that the modulation variation between solar minimum and solar maximum is smaller compared

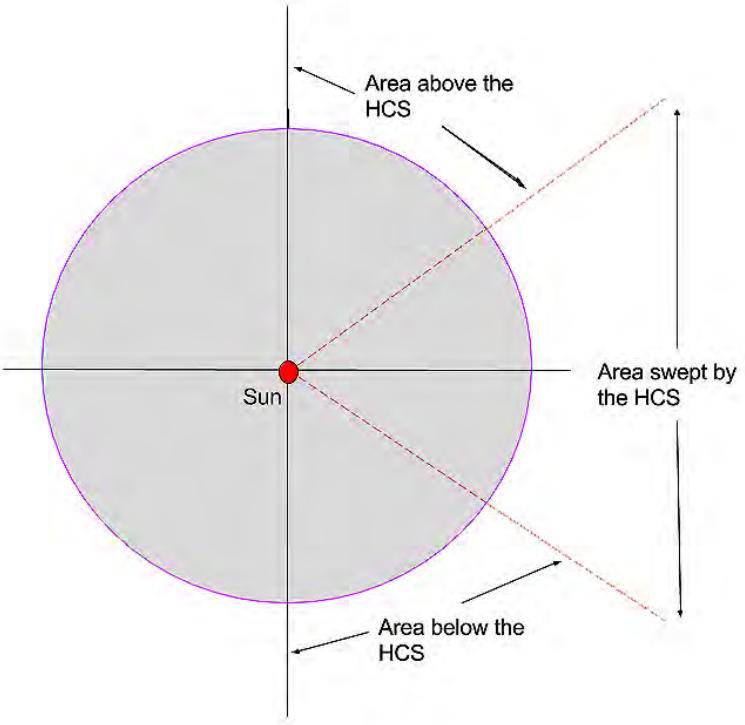

FIGURE 6.7: A 2-D schematic diagram showing the HCS region. Inside the area swept by the HCS the drift coefficient K_A scales as a function of time as given by Equation 4.16 and in the area above and below the HCS K_A does not scale as $f_1(t)$ given by Equation 4.16, i.e. $f_1(t) = 1.0$.

to the standard scenario. Encouraging is that the model shows a somewhat flatter intensity profile which is an improvement compared to the modified compound approach results. The $\acute{\theta} > 40°$ and $\acute{\theta} > 60°$ results are similar and show a peaked profile similar to the modified compound approach results.

The last scenario corresponds to intensities calculated by setting $f_1(t) = 1.0$ when $\acute{\theta} > \alpha$. As shown, the model produces improved compatibility to observations from $\sim$ 1981 - 1986 and again from $\sim$ 1989 - 1992 along the Voyager 1 and 2 trajectories for this scenario. Note the model still does not predict step increases and decreases observed as these structures are not included. In the bottom panel calculations are done along Voyager 2 trajectory. The results shows less sensitivity between different scenarios along Voyager 2 trajectory. Peaked profiles compatible to observations are computed for all scenarios. It seems that limiting the effect of $f_1(t)$ to latitudes less than the tilt angle leads to improved compatibility with Voyager 1 observations (when this spacecraft was above the HCS region) and also results in compatibility with Voyager 2 observations.

However, these results should be interpreted by noting that this proposed latitude dependence in the time-dependence of the drift coefficient may lead to additional terms in Equation 3.29

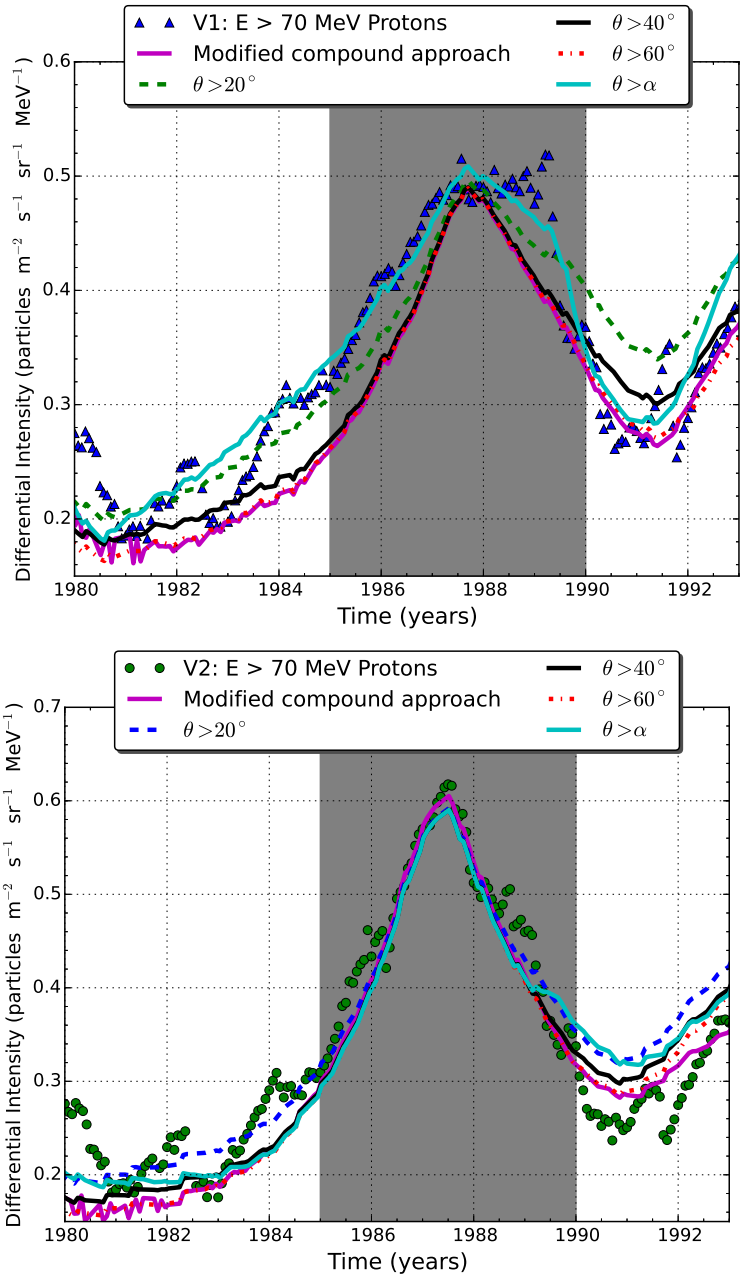

FIGURE 6.8: The top panel is the computed 2.5 GV cosmic ray proton intensities along the Voyager 1 trajectory and the bottom panel is along Voyager 2 trajectory, computed for a time-independent drift coefficient for the given $\acute{\theta}$ values and $\acute{\theta} > \alpha$ as indicated in the legend. Also shown are the $E > 70$ MeV proton observations from the Voyager 1 and 2. Data from $http://voyager.gsfc.nasa.gov$.

when the curl is taken to keep the drift velocities zero. This will only be of importance at the interface between the two regions. A full implementation of these terms in this 2D model (where drifts are simulated compared to a 3D model) is not presented here. The effect of a spatial dependence in the time-dependence of the drift coefficient is a topic of future study.

In Figure 6.9 model calculations shown follow on a similar logic as those shown in Figure 6.8, but now with the time-dependence in the diffusion coefficients limited at latitude above

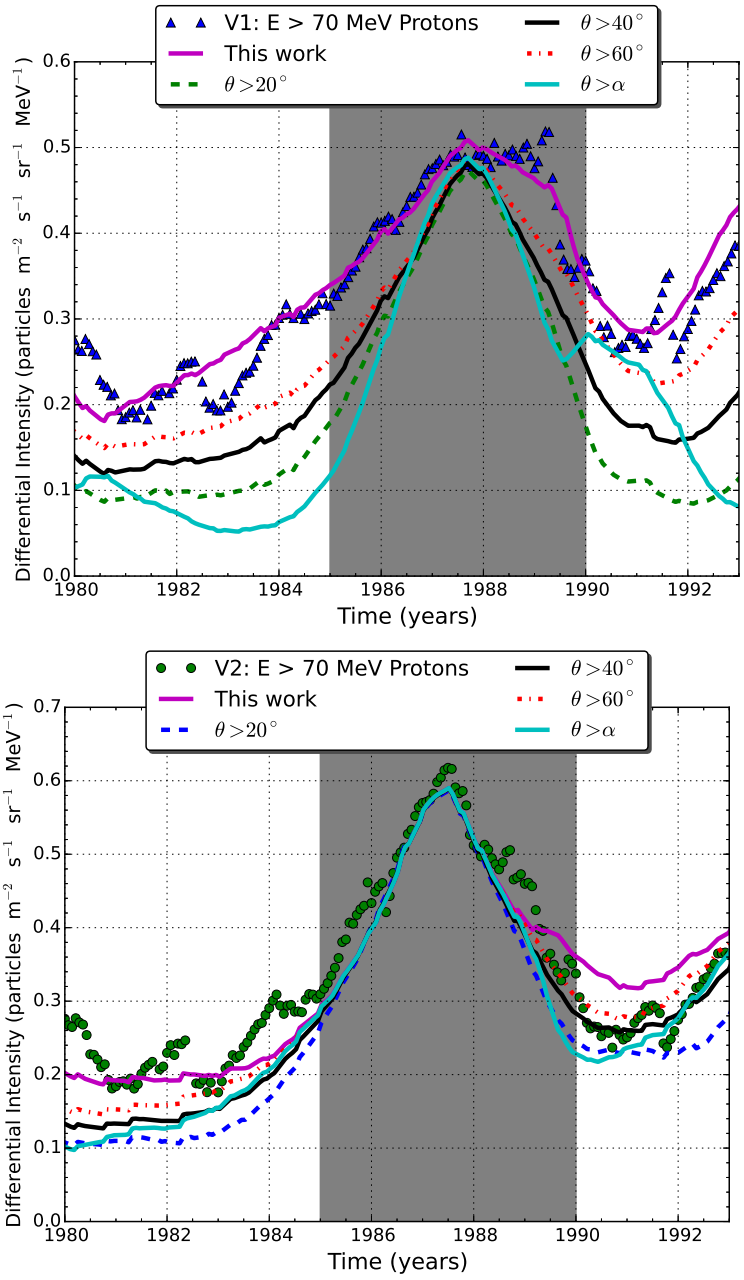

FIGURE 6.9: Similar to Figure 6.8 but computed for time-independent diffusion coefficients for the given $\acute{\theta}$ values and $\acute{\theta} > \alpha$ as indicated in the legend.

certain values, e.g. $\acute{\theta} > 20°$, $\acute{\theta} > 40°$ and $\acute{\theta} > 60°$ and $\acute{\theta} > \alpha$, i.e. $f_2(t) = f_3(t) = 1.0$ in these regions. Shown also are $E > 70$ MeV proton observations from Voyager 1 and 2 and the previous scenario where time-dependent effects by $f_1(t)$ are limited only where $\acute{\theta} < \alpha$ is denoted 'This work'.

Shown is that when a latitude dependence is assumed for the time-dependence in the diffusion coefficients, the modulation variation between solar minimum and solar maximum can be effected along the Voyager 1 trajectory. Along the Voyager 2 trajectory, the model is less sensitive to a latitude dependence of $f_2(t)$ and $f_3(t)$. It can be concluded that a spatially dependent time-dependence seems to be necessary to compute improved compatibility with

Voyager 1 observations. Also note that introducing the controlled time-dependence in the diffusion coefficients eliminated the plateau profile produced in 'This work' scenario.

6.5 Summary and Conclusions

This chapter focussed on modelling the 1985 - 1990 period of Voyager 1 and 2 observations. The discussion started first with a comparison between the traditional compound approach of Ferreira [2002] and the modified compound approach of Manuel et al. [2014] for different cases as was shown in Figures 6.1 and 6.2. Along Voyager 1 trajectory, shown in Figure 6.1, it follows that the traditional compound approach computed a somewhat flatter intensity profile while the modified compound approach computed a more pronounced peaked intensity profile. This was due to a particular dependence of the transport coefficients on the magnetic field for the traditional compound approach and the peaked intensity profile by the modified compound approach was due to the particular dependence of the drift coefficient on the tilt angle. Along Voyager 2 trajectory, Figure 6.2 showed that the traditional compound approach computed a somewhat flatter intensity profile while the modified compound approach a peaked intensity profile more compatible with observations. Figure 6.6 showed that for the period of interest Voyager 1 was above the HCS region and Voyager 2 inside the HCS region. It followed that the time-dependence for drift coefficient given in Equation 4.16 did not result in compatibility with observations along Voyager 1 trajectory for periods above the HCS region as it did along Voyager 2 trajectory inside the HCS region.

Quantitatively from Figures 6.1 and 6.2 it followed that the scaling of drift coefficient over a solar cycle had a larger effect on computed cosmic ray intensities than did scaling of diffusion coefficient for the period of interest. To further substantiate this and introduce modification to the compound approach of Manuel et al. [2014], a modification based on the schematic diagram of Figure 6.7 was constructed and results were shown in Figure 6.8. This figure showed the effects of a latitude-dependence in the time-dependent function $f_1(t)$ on the calculated cosmic ray intensities. It followed that calculations along Voyager 1 trajectory (which was above the HCS region for the period of interest) showed a flatter computed cosmic ray intensity profile with improved compatibility with observations, when compared to the modified compound approach. Calculations along Voyager 2 trajectory (which was inside the HCS region for the period of interest) under these conditions showed no significant deviation when such a modification was implemented. However, as discussed one should be careful when implementing a spatial dependence in the time-dependence of the drift coefficient in a 2D modulation model.

Chapter 7

Modelling the 1992 - 2001 period of cosmic ray intensities along Voyager spacecraft trajectories

7.1 Introduction

In the previous chapter a modification to the time-dependence in the drift coefficient of the modified compound approach of Manuel et al. [2014] was proposed to improve compatibility between Voyager 1 observations and the model for the 1985 - 1990 period. In this chapter the focus shifts to the 1992 - 2001 period along both the Voyager spacecraft trajectories. It is shown that this period has its own challenges when trying to establish compatibility between the model and observations. For this period, the model of Manuel et al. [2014] gives compatible intensities on a global scale for most of the period, except for period of increasing solar activity where the model computes a faster decrease in intensities with increasing solar activity than what is observed.

7.2 Overview of the 1992 - 2001 period

The modification proposed and implemented in the previous chapter for the period 1985 - 1990 showed better compatibility with Voyager 1 observations, thus an improvement of the approach by Manuel et al. [2014]. This chapter investigates the next solar cycle from 1992 - 2001 to improve compatibility between the model and Voyager observations. Figure 7.1 shows the latitude of Voyager 1 and 2 spacecraft from 1980 - 2010. Also shown are the values of the L model of the tilt angle with L_n tilt values in the northern hemisphere and L_s tilt values in the southern hemisphere at the position of the Earth.

It follows from Figure 7.1 that, around $\sim$ 1990, the latitude of the Voyager 1 spacecraft was $\sim 30^\circ$ in the northern hemisphere and changed gradually to $\sim 35^\circ$ by 2010, while the Voyager 2 spacecraft around $\sim$ 1990 was at a latitude of $\sim 2^\circ$ in the northern hemisphere and then at

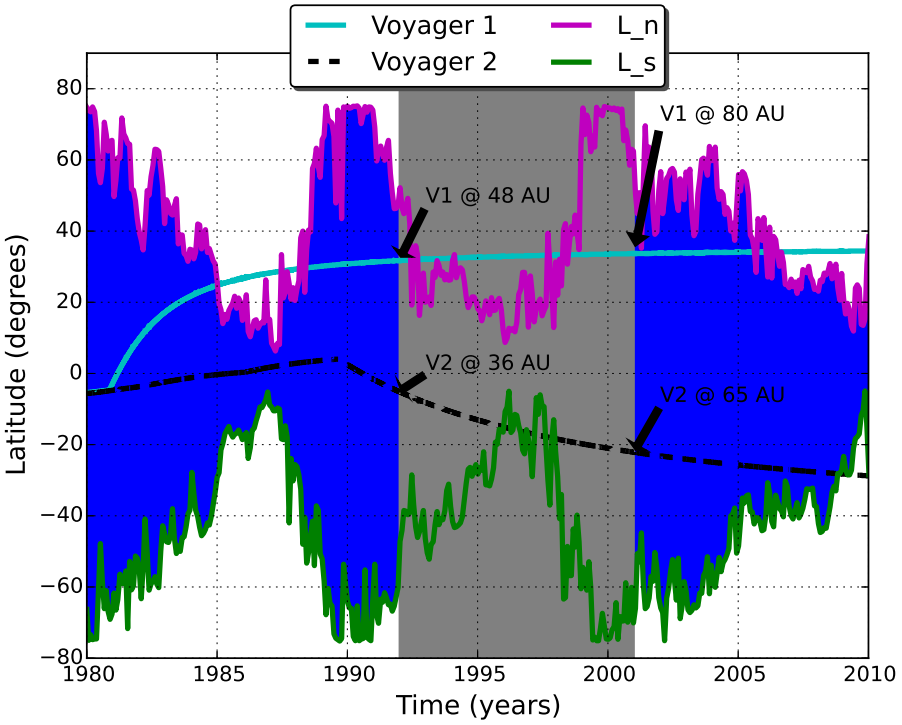

FIGURE 7.1: The latitude of Voyager 1 (solid cyan line) and Voyager 2 (dashed black line) as a function of time. Also shown are the values of the L model of the tilt angle in the northern (L_n) and southern (L_s) hemispheres as a function of time. The grey shaded area is the period under investigation and the blue shaded area is the region inside the latitudinal extent of the HCS region. Indicated also by the black arrows is the Voyager spacecraft radial distances.

a latitude of $\sim 27°$ in the southern hemisphere by 2010. It also shows that from $\sim$ 1992.5 - 1998 and from $\sim$ 2006.5 - 2010 the Voyager 1 trajectory was above the HCS region, while the Voyager 2 trajectory was from $\sim$ 1995.5 - 1997.5 and from $\sim$ 2008.5 - 2010 below the HCS region. These values are not adjusted for the propagation time to the two Voyager spacecraft positions. In 1992 Voyager 1 was at $\sim$ 48 AU and Voyager 2 at $\sim$ 36 AU, and in 2001 Voyager 1 was at $\sim$ 80 AU and Voyager 2 at $\sim$ 65 AU.

In the top panel of Figure 7.2, the $E > 70$ MeV proton observations are shown for Voyager 1 (blue triangles) and Voyager 2 (magenta squares) for the period 1990 - 2005. The focus now is on the period 1992 - 2001. The areas shaded in grey are during the period of increased solar activity, when merged diffusive propagation barriers become important to the modulation of cosmic rays. Because these structures are not incorporated in the model, these periods are not considered in this chapter. From the figure it follows that the measurements of Voyager 1 and 2 do not differ significantly for the period of interest in this chapter.

The middle panel of Figure 7.2 shows the observed 26-day averaged HMF magnitude (magenta solid line) at Earth compared to the HCS tilt angle (black solid line) for the period 1992 - 2001. In the bottom panel the magnitude of the time-dependent functions $f_1(t)$ for the drift coefficient (blue solid line), $f_2(t)$ for parallel diffusion coefficient (green solid line) and $f_3(t)$ for

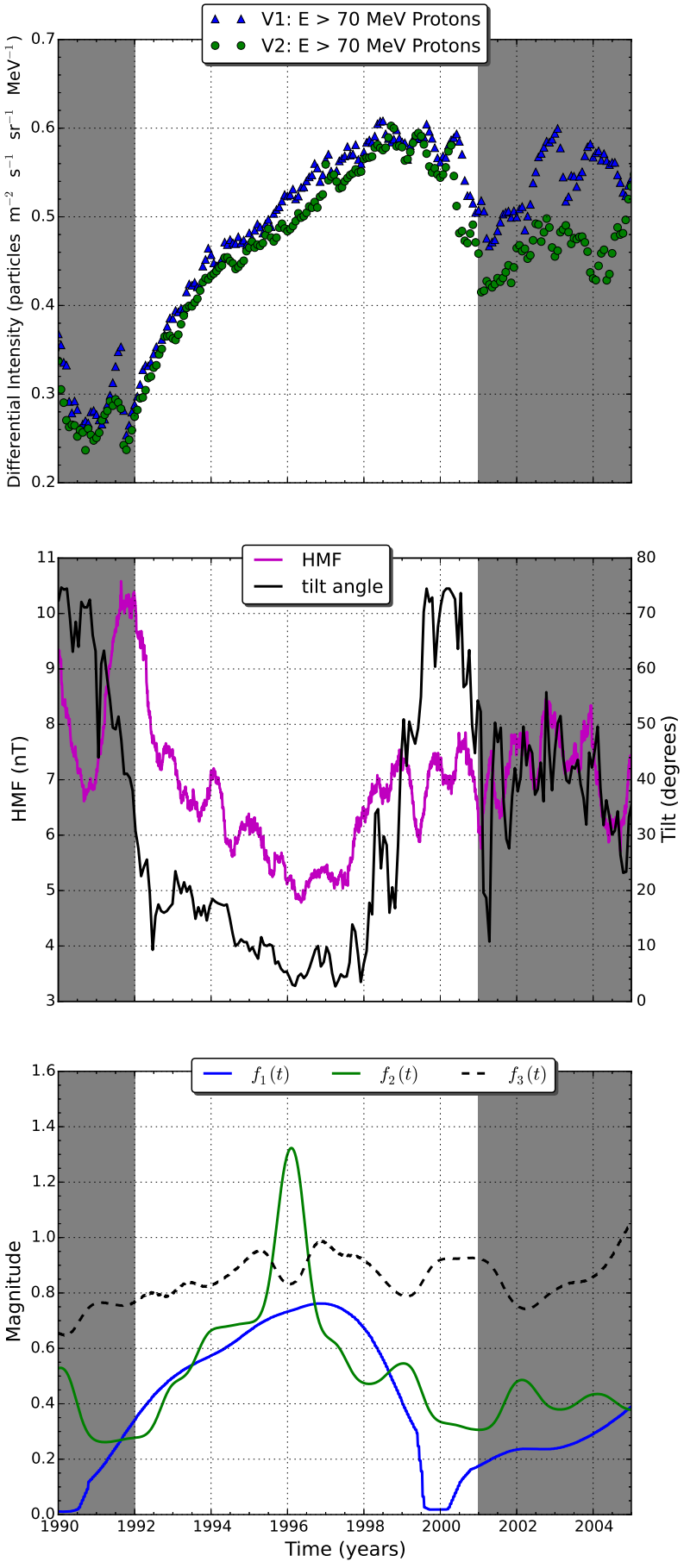

FIGURE 7.2: Top panel: $E > 70$ MeV Proton observations from the Voyager 1 and 2 spacecraft for the period 1990 - 2005. Middle panel: Comparison of the HMF and the tilt angle values. Bottom panel: Comparison of the time-dependent functions $f_1(t), f_2(t)$ and $f_3(t)$ given by Equations 4.16, 4.9 and 4.15 respectively. Data from *http* : *//voyager.gsfc.nasa.gov*.

perpendicular diffusion coefficients (black dashed line) are also shown and compared to each other for the period 1992 - 2001.

Comparing the middle and the bottom panel of Figure 7.2 it follows that around $\sim$ 1997 as the tilt angle started increasing the time-dependent function $f_1(t)$ started decreasing because of the inverse relationship of this function with the tilt angle as given in Equation 4.16. As the tilt angle increased rapidly from $\sim$ 1998 - 1999.5, the HMF stayed roughly constant with variations around a mean value of $\sim$ 7.5 nT. The other time-dependent functions $f_2(t)$ and $f_3(t)$ (Equations 4.9 and 4.15) does not have a straight forward dependence on the magnetic field. It follows that the proton intensity decreased systematically after 2000 while the tilt angle was already at what can be called solar maximum.

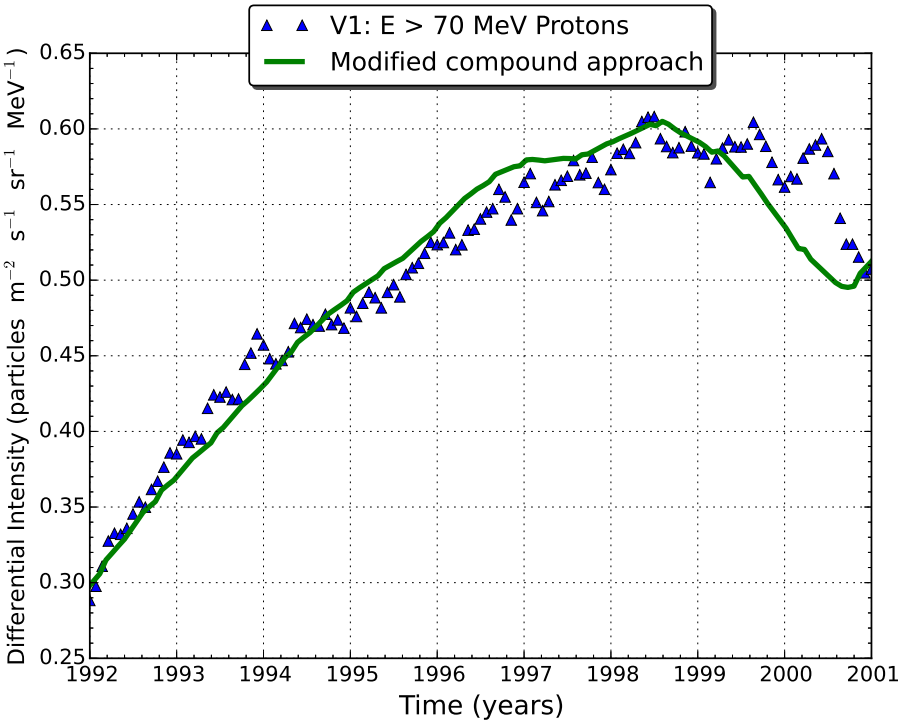

FIGURE 7.3: Computed 2.5 GV proton intensities along the Voyager 1 trajectory for the period 1992 - 2001 using the modified compound approach of Manuel et al. [2014]. Also shown are the $E > 70$ MeV proton observations from Voyager 1. Data from $http://voyager.gsfc.nasa.gov$.

Figure 7.3 shows computed cosmic ray intensity using the modified compound approach of Manuel et al. [2014] indicated by the solid green line for the period 1992 - 2001. Simulations are along the Voyager 1 trajectory. Shown for comparison are $E > 70$ MeV proton observations from the Voyager 1. It follows that the model by Manuel et al. [2014] gives intensities decreasing faster than the Voyager 1 observations from $\sim$ 1998.5 towards the solar maximum in 2001. In fact, although the observed protons fluctuate, their intensity seemed to remain on average at a maximum value for almost two years.

This incompatibility seemed to be caused by the model being too sensitive to changes in the tilt angle of the HCS during this A $>$ 0 polarity cycle, demonstrated by comparing Figures 7.2

and 7.3. From Figure 7.2 it follows that while the tilt angle increased from $\sim$ 1998 and the time-dependent function $f_1(t)$ as in Equation 4.16 decreased, the model by Manuel et al. [2014] responds almost immediately to the time-dependent changes in the tilt angle. This aspect is investigated next.

7.3 Modelling the 1992 - 2001 period

To improve compatibility with observations a parameter study is done in this section to determine if selected modulation parameters would lead to improved compatibility between the model and Voyager observations.

First, it is worth noting that the numerical scheme used for the modelling is based on an assumed grid with new input updated for every iteration. In this manner all time-dependent changes are transported outward from the inner boundary at the solar wind speed.

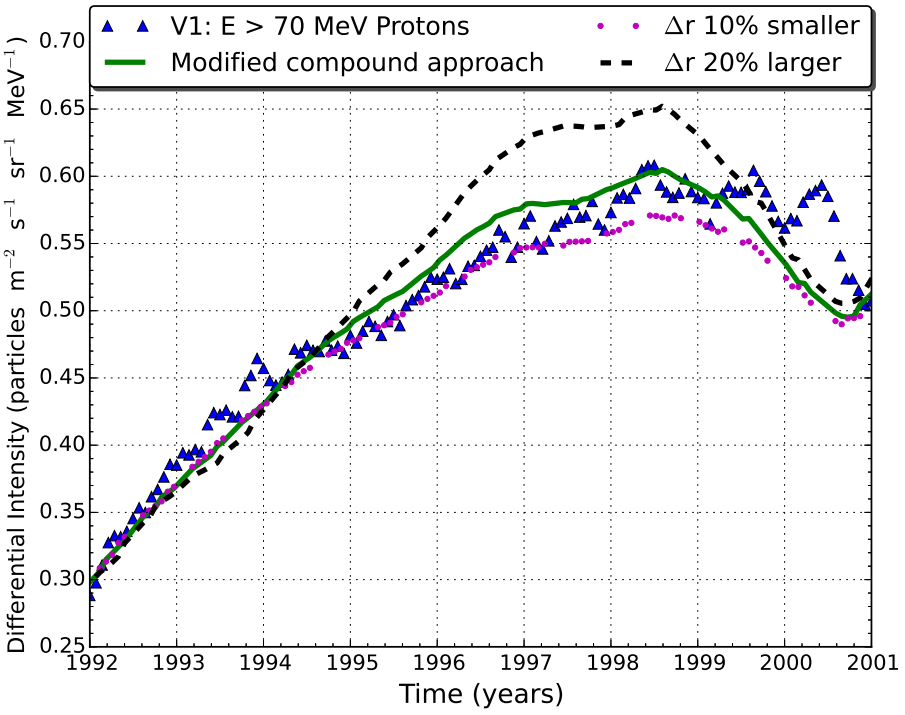

FIGURE 7.4: Computed 2.5 GV proton intensities along the Voyager 1 trajectory for the period 1992 - 2001 assuming different radial grid sizes (denoted by Δr) as indicated. Also shown are the $E > 70$ MeV proton observations from Voyager 1. Data from *http* : *//voyager.gsfc.nasa.gov*.

Figure 7.4 shows the computed 2.5 GV proton intensity along the Voyager 1 trajectory, using the modified compound approach of Manuel et al. [2014]. In this figure different radial grid lengths are assumed. For the magenta dotted line the radial grid length (Δr) is decreased by 10% while for the dashed black line the grid is increased by 20%. Note that apart from Δr

changing, the grid also changes the boundary position. E.g. a 10% decrease in Δr results in a modulation boundary 10% less.

Following from Figure 7.4 is that decreasing Δr by 10% the model gives similar results as the modified compound approach up to 1994.5. For the period $\sim$ 1994.5 - 1999 the model gives intensities below the modified compound approach. For this period, the scenario agrees better with Voyager 1 observations than the modified compound approach, but the model still gives intensities below both the observations of the Voyager 1 spacecraft and the modified compound approach. From $\sim$ 2000 onwards, this scenario results in less compatibility when compared to observations. For the second scenario where Δr is increased by 20%, the model gives intensities below the modified compound approach up to 1995. From 1995 - 2001 this scenario results in intensities above the modified compound approach and observations. For this scenario the modulation amplitude between solar minimum and maximum is larger due to the increase in modulation volume when the radial grid is increased.

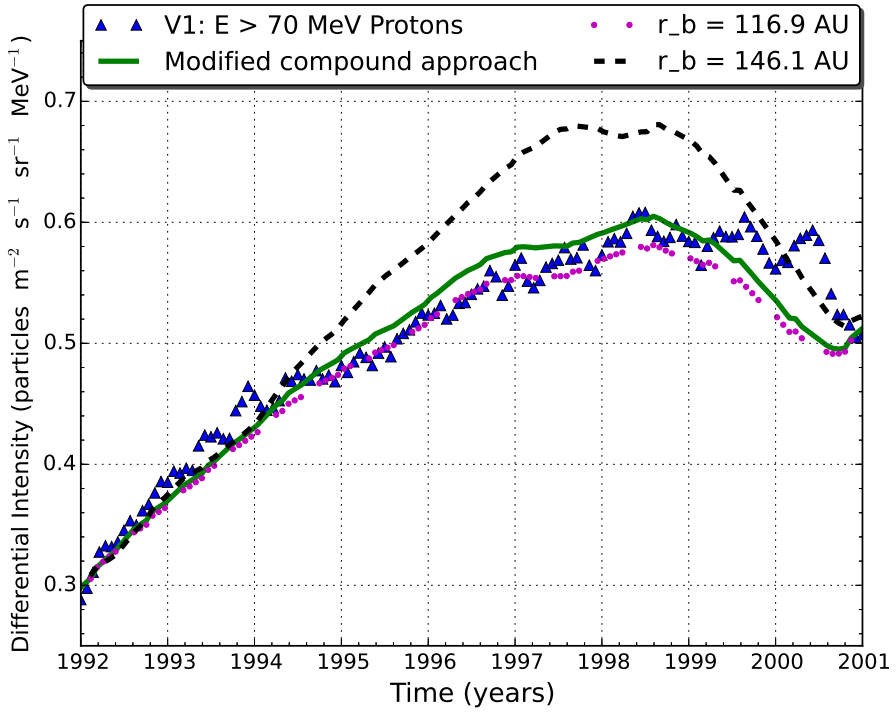

FIGURE 7.5: Computed 2.5 GV proton intensities along the Voyager 1 trajectory for the period 1992 - 2001 assuming different heliopause positions (denoted by r_b) as indicated. Also shown are the $E > 70$ MeV proton observations from Voyager 1. Data from *http* : *//voyager.gsfc.nasa.gov*.

Figure 7.5 shows similar computations as in Figure 7.4 but here calculations are done for different modulation boundary positions by changing the total number of grid points N in the radial direction. The dotted magenta line is with $N = 100$ which gives an outer boundary of 116.9 AU, the black dashed line with $N = 125$ gives an outer boundary of 146.1 AU. The

modified compound approach with $N = 105$ gives an outer boundary of 122.7 AU. Note also that Δr is kept constant at a value of $\sim$ 1.2 AU.

The results in Figure 7.5 show that, when the modulation boundary is chosen to be at a distance of 146.1 AU, from $\sim$ 1992 - 1994.2 this scenario corresponds with the modified compound approach. But for the period $\sim$ 1994.2 - 1999.5 the computed intensities are above both the observations and the modified compound approach. The other scenario with the outer boundary at 116.9 AU shown by magneta dotted line also corresponds to the modified compound approach for the period $\sim$ 1992 - 1994.2, but for the period $\sim$ 1994.2 - 1999.2, this scenario agrees with observations and thereafter the computed intensities are below the observed and even below the modified compound approach. As discussed above, increasing modulation volume leads to an increase in the computed modulation variation between solar minimum and solar maximum. As is evident, changing the outer modulation boundary does not result in improved compatibility after $\sim$ 2000.

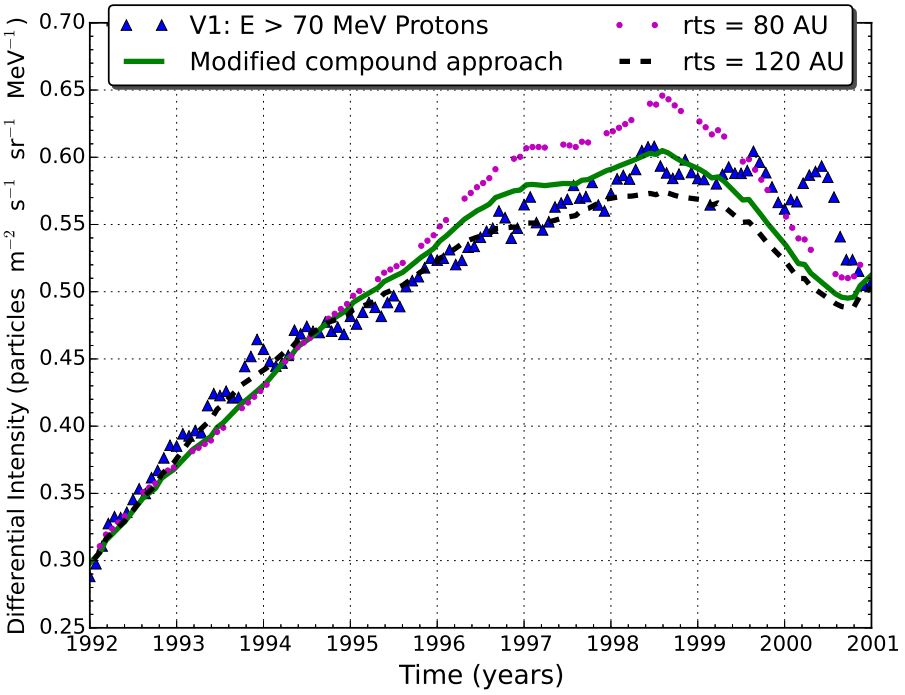

FIGURE 7.6: Computed 2.5 GV proton intensities along Voyager 1 trajectory for the period 1992 - 2001 assuming different termination shock positions (denoted by *rts*) as indicated. Also shown are the $E > 70$ MeV proton observations from Voyager 1. Data from *http* : *//voyager.gsfc.nasa.gov*.

The model assumes a simple static termination shock, which when changed time-dependently can have an influence on computations around periods when Voyager spacecraft crossed the termination shock. See Chapter 4 for a discussion on the time-dependent termination shock radius. Figure 7.6 shows similar calculations as in the previous figure, but are done for different termination shock positions as denoted by the dotted magenta line (shock position at 80 AU)

and the dashed black line (shock position at 120 AU). The $E > 70$ MeV proton observations from Voyager 1 spacecraft are shown as blue triangles and the modified compound approach (shock position at 90 AU) shown by a green solid line.

From Figure 7.6 it follows that moving the termination shock inwards from 90 AU to 80 AU results in computed intensities above the modified compound approach after the period 1995. The second scenario with the termination shock position moved outwards to 120 AU shows that, for the period $\sim$ 1992 - 1995, the computed intensities are above the modified compound approach, but from $\sim$ 1995 - 2001 intensities are below the modified compound approach. It follows that, changing the position of the termination shock also does not improve compatibility between the computed and observed intensities after $\sim$ 2000.

7.4 The Averaged Tilt Angle

It was mentioned in Chapter 2 that the heliosphere is a dynamic structure due to a solar activity cycle and a solar magnetic cycle. This means that over a solar cycle the heliosphere does not remain in a steady state and over a period of a year the turbulent solar wind reaches the outer limits of the heliosphere and therefore during this time, for example, the tilt angle at Earth can be significantly different from the tilt angle in the outer heliosphere [le Roux, 1990, Williams, 1990].

Recently, Moloto [2015] used the averaged tilt angle in the steady-state modulation model in order to account for the time-dependent changes of cosmic rays in the heliosphere. The concept behind this approach is that the intensities measured at a certain time are associated with the average of at least the previous year's tilt angle. Figure 7.7 shows the calculated HCS tilt angle values denoted by the solid blue line. The averaged tilt was computed by applying a moving average for 12 and 24 months, respectively, which smooths tilt angles accordingly. Comparing these averaged tilt angle values to original data shows that they are time shifted with respect to the original data. From the work of Moloto [2015] it follows that computing a 12 month effective tilt angle is roughly similar to taking a 6 month forward time shift of the original data.

Vos [2012] and later Vos [2016] used a similar concept of applying simple moving averages to the tilt angle and the HMF values measured at Earth in order to account for time-dependent changes in the steady-state modulation model. The averaging window used by Vos [2016] is based on the propagation times of the tilt angle and the frozen-in HMF to reach the outer modulation boundary. For the tilt angle an average of 16 months based on the averaged solar wind speed during solar minimum due to HCS being mostly confined in the ecliptic region was calculated, but for the HMF an average of 10 months based on the weighted average of both the fast and slow solar wind streams was calculated. Figure 7.8 shows in the top panel the

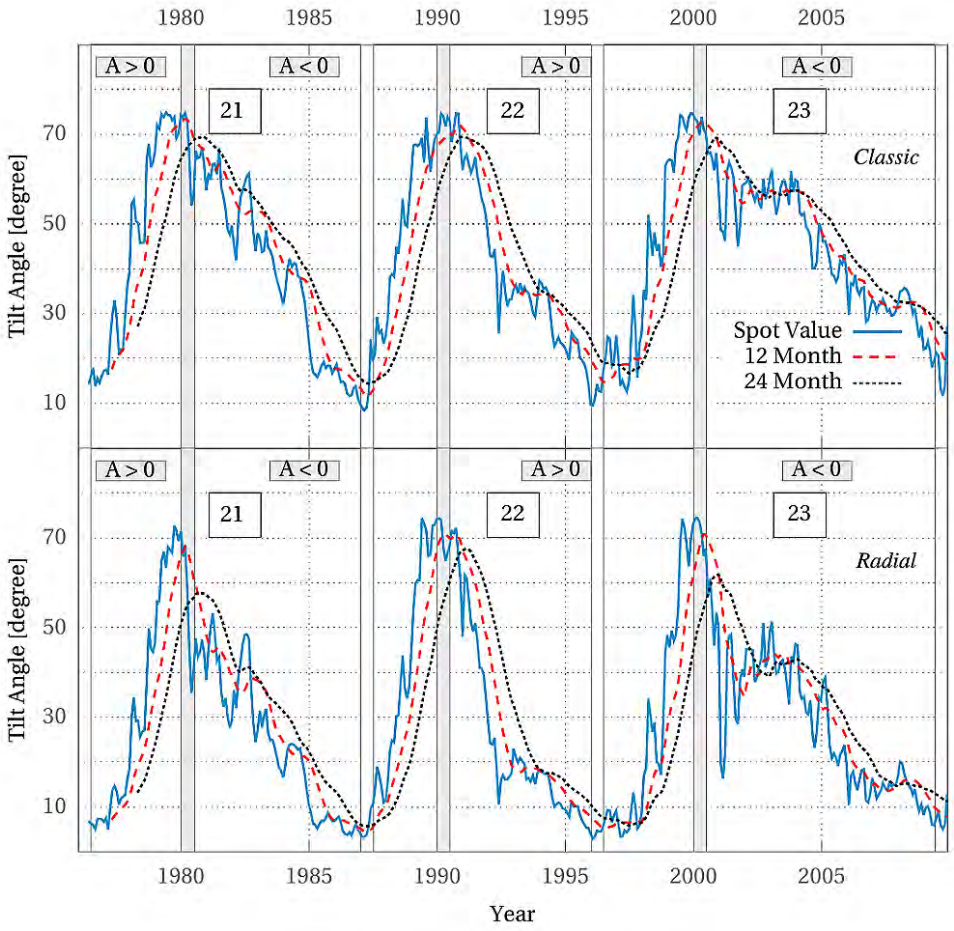

FIGURE 7.7: The averaged tilt angle values for both the classic and radial tilt angle models. From Moloto [2015].

HCS tilt angle values and their corresponding simple moving averages for comparison. In the bottom panel the HMF values at Earth are shown and also their corresponding simple moving averages for comparison.

Based on analysis and discussion of Figures 7.2 and 7.3, similar concept of averaged tilt angle is applied in this work in order to compute better compatibility between the model and the measurements for the period in question. Figure 7.9 shows the calculation of 2.5 GV proton intensities along the Voyager 1 trajectory, incorporating a 6 months (shown by cyan dashed line) and a 3 months (shown by black dotted line) forward shift of the tilt angle values, for the period 1992 - 2001, using the modified compound approach of Manuel et al. [2014]. Proton intensity with $E > 70$ MeV from the Voyager 1 are again shown by blue triangles for comparison.

Note that between $\sim$ 1992.5 - 1998 Voyager 1 is above HCS according to Figure 7.1. The comparison between the modified compound approach shown and the two scenarios computed (both the 3 and 6 months shift) shows how this forward shift improved the compatibility of results from 1998, but this shift does not result in compatibility for the period $\sim$ 1992 - 1994.5.

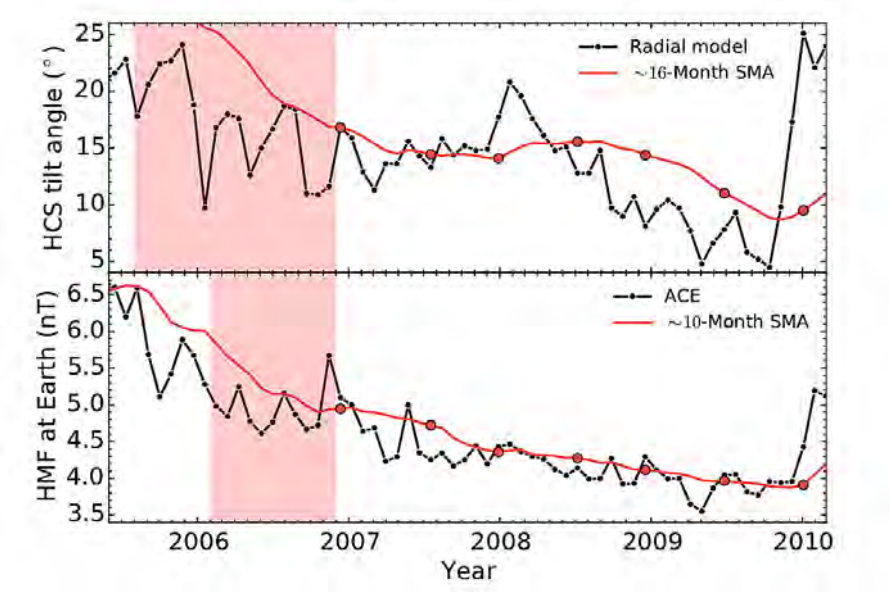

FIGURE 7.8: Top panel: The 16-month simple moving averages of the tilt angle compared to the tilt angle at Earth from the radial tilt angle model. Bottom panel: The 10-month simple moving averages of the HMF compared to the HMF measurement at Earth by ACE spacecraft. From Vos [2016].

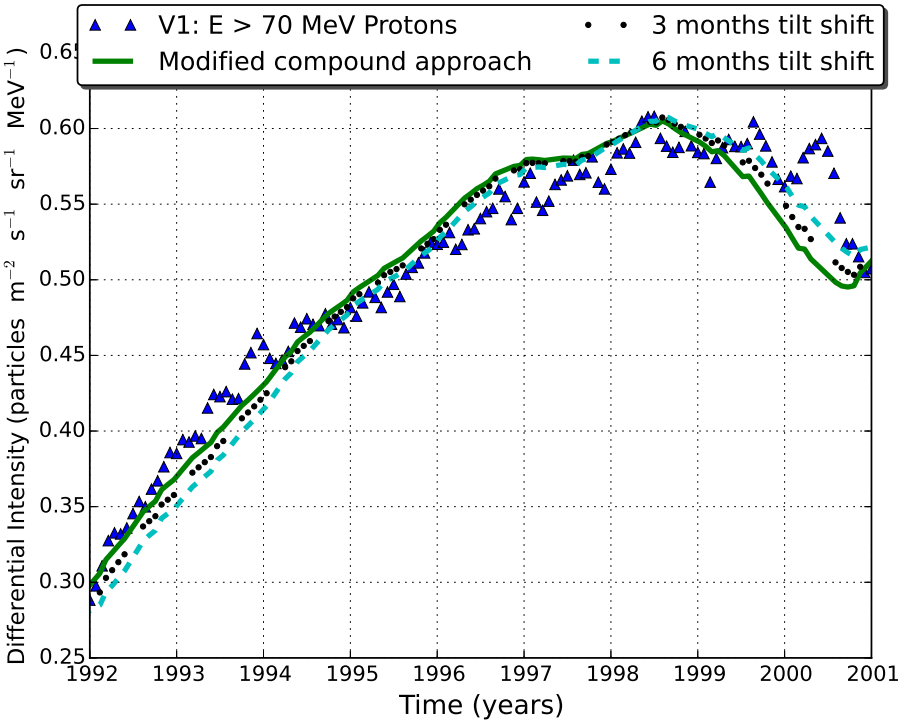

FIGURE 7.9: Computed of 2.5 GV proton intensities along the Voyager 1 trajectory for the period 1992 - 2001, using the modified compound approach of Manuel et al. [2014] and incorporating in the model the 3 and 6 months forward shifted tilt angle values. Also shown are the $E > 70$ MeV proton observations from Voyager 1. Data from *http* : *//voyager.gsfc.nasa.gov*.

This behaviour might be due to the effect of the way tilt angle is calculated as spelled out by Ferreira [2002] and Ferreira and Potgieter [2003], but also due to how the drift coefficient

scale time-dependently for periods above HCS. Ferreira [2002] found that different models for the tilt angle should be used for either increasing or decreasing solar activity.

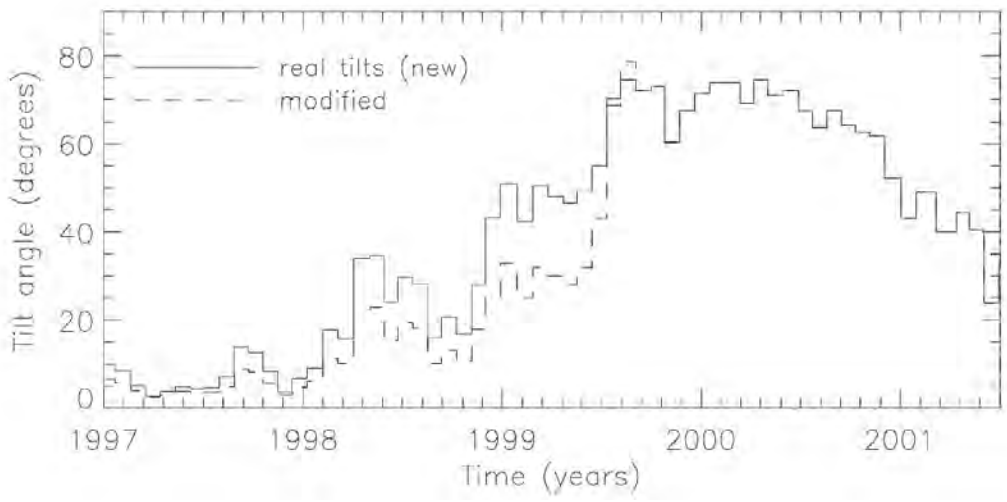

FIGURE 7.10: The modified tilt angle α_m compared to radial tilt model values. From Ferreira [2002].

Figure 7.10 shows the modified tilt angle values used by Ferreira [2002] to fit the model to Ulysses observations after 1998. Note that these are modified to have a smaller rate of change compared to the radial tilt model values. As assumed by Ferreira and Potgieter [2004], the tilt model with the smallest rate of change is to be used for either increasing or decreasing solar activity. As shown by Ferreira [2002] and in this work it seems that for periods of increasing solar activity, a tilt angle with a smaller rate of change seems necessary to compute modelling results compatible to observations.

7.5 Summary and Conclusions

In this chapter the focus was on modelling the 1992 - 2001 period of Voyager 1 and 2 observations. The modified compound approach of Manuel et al. [2014] was applied to the period of interest in this chapter and the results in Figure 7.3 show that the model by Manuel et al. [2014] resulted in intensities decreasing faster than observations towards the solar minimum after $\sim$ 1998.5. Following the comparison of the tilt angle with the HMF and the $E > 70$ MeV proton observations from the Voyager 1 and 2 spacecraft, shown in Figure 7.2, the incompatibility between the model and the observations shown in Figure 7.3 was directly linked to the observed tilt angle via the time-dependent function $f_1(t)$. The tilt angle already started to increase after $\sim$ 1998 while observations stayed constant up to $\sim$ 2000.

In order to improve compatibility between the model and Voyager observations, modification of the tilt angle was proposed. Other authors, e.g. Ferreira [2002], Moloto [2015], Vos [2012] and Vos [2016], also used similar approach to modify the tilt angle in order to account for the

time dependence. The calculated tilt angle values for the period of interest in this chapter were modified by applying a simple running average which resulted in the forward time shift of the computed cosmic ray intensities as shown in Figure 7.9. From the two forward time shifts, it can be concluded, following the tilt angle measurements shown in Figure 7.7, that the slope of the tilt angle decrease (e.g. 1992 - 1995) is not the same as the slope for tilt angle increase (e.g. 1995 - 2000) and therefore, as a result, the window over which the running average is calculated for periods of decreasing solar activity needs be different from that of increasing solar activity. Ferreira [2002] also suggested different models for the tilt angle to be used for either decreasing or increasing solar activity and later Ferreira and Potgieter [2004] assumed the tilt model with the smallest rate of change in the model for either decreasing or increasing solar activity.

Chapter 8

Summary and Conclusions

This work started by introducing the reader to the heliosphere, which is the region influenced by the Sun, as the modulation volume, in which cosmic rays are modulated. From the Sun originates the solar wind which pushes back the interstellar medium to create the heliosphere, where cosmic rays upon encountering, experience changes in their intensities as a function of time, energy and position. Embedded in the solar wind is the magnetic field of the Sun known as the HMF, which is assumed to have a basic structure, called Parker spiral. Towards the poles of the Sun the HMF is modified using the so-called Jokipii-Kòta modification. These HMF field lines have a typical dipole structure, whereby in one heliospheric hemisphere they are pointed towards the Sun and away in the other hemisphere. In the equatorial regions, these oppositely directed HMF lines are separated by a thin neutral region known as the HCS.

An important parameter describing the HCS is the tilt angle α, which is the angle between the rotation axis and the magnetic axis of the Sun, as discussed in Chapter 2. As the Sun rotates about its axis and α varying with solar activity, the current sheet oscillates and forms a series of peaks and valleys spiralling outward. The waviness of the HCS is dependent on the solar activity with α varying from $\sim 5^\circ$ at solar minimum to $\sim 75^\circ$ at solar maximum. Observations by neutron monitors on Earth exhibit a clear $\sim$ 11 year cosmic ray modulation cycle which is anti-correlated with solar activity cycle and $\sim$ 22 year modulation cycle related to magnetic cycle caused by polarity changes of the solar dipole every $\sim$ 11 years at solar maximum. This work focused on time-dependent modulation of cosmic rays using a 2D time-dependent model based on solving Parker's transport equation and comparing model results to different spacecraft observations for interpretation. The model requires input parameters which are the solar wind speed, tilt angle, heliospheric structure and transport processes. The distribution of the cosmic rays in the heliosphere is the result of the four different major transport processes, i.e., drift caused by the gradient and curvature of the HMF and by any abrupt changes in the direction of the magnetic field in the HCS, diffusion caused by fluctuations in the HMF which result in particles undergoing diffusive propagation, convection by the solar wind propagating outwards from the Sun and the adiabatic energy changes caused by the divergence of the solar

wind. These four major modulation processes are contained in the Parker [1965] transport equation and were discussed in Chapter 3.

To calculate cosmic ray intensities, a well-established 2D time-dependent cosmic ray modulation model including the modified compound approach of Manuel et al. [2014] was used. In particular $E > 70$ MeV proton cosmic ray intensities measured along the Voyager 1 and 2 trajectories were used to compare results with. The results show that the model is compatible with observations on a global scale, however for certain periods, e.g. the period 1985 - 1990 which corresponds to a solar minimum, the model along the Voyager 1 trajectory is not compatible with observations. For this period the model gives a peak-like intensity profile while observations showed a plateau-like intensity profile along the Voyager 1 trajectory. However, along the Voyager 2 trajectory, observations and model results are in good agreement with both showing a peak-like intensity profile. For this period of interest Voyager 1 went up to high latitudes in the northern hemisphere while Voyager 2 stayed close to the equatorial region in the northern hemisphere.

Various modulation parameters used in the model as input parameters were investigated in Chapter 5 to establish if they could possibly lead to different modulation conditions between Voyager 1 and 2, resulting in the incompatibility between Voyager 1 observations and model calculations for the period 1985 - 1990. It was shown that there are some small scale differences of a few months between these parameters in the two hemispheres sampled by the Voyager 1 and 2 spacecraft. It is concluded that these differences are not enough to account for the difference between Voyager 1 and 2 measurements for the period of interest. Two other cosmic ray energy channels, i.e. 30 - 69 MeV and 133 - 242 MeV, were also investigated to determine whether the plateau-like intensity profile along the Voyager 1 trajectory is evident only in the integrated $E > 70$ MeV channel. It is found that the plateau-like intensity feature of Voyager 1 is also present at lower energies.

It was shown in Chapter 6 that the traditional compound approach of Ferreira [2002] gives a somewhat flatter intensity profile along the Voyager 1 trajectory. This is caused by the particular time-dependence of the diffusion coefficients as related to the HMF magnitude and tilt angle dependence given by Equations 4.1 and 4.2. This is not the case with the modified compound approach. For the period of interest (1985 - 1990), Voyager 1 went to higher latitudes and above the HCS region between $\sim$ 1985 and 1988 , while Voyager 2 stayed in the equatorial region and always inside the HCS region. It is concluded that, during this period, the measured flat intensity profile by Voyager 1 could be the result of the cosmic rays not being strongly influenced by time dependent changes in the HCS region and drift coefficient, as opposed to measurements of Voyager 2 inside the HCS region. A proposed latitude dependence of the time-dependent functions $f_1(t)$ (which scales drift coefficient over a solar cycle), $f_2(t)$ (which scales the parallel diffusion coefficient over a solar cycle) and $f_3(t)$ (which scales perpendicular diffusion coefficient over a solar cycle) were studied. From this

study a refinement to $f_1(t)$ is proposed. It was shown that, by limiting the time-dependence of the drift coefficient to certain latitudes, i.e to regions inside the HCS region (e.g. $\acute{\theta} < \alpha$) only, this results in improved compatibility between Voyager 1 observations and the model. It followed that calculations along the Voyager 1 trajectory (which is above the HCS region for the period of interest) at some latitude $\acute{\theta}$ above the equatorial plane show a somewhat flatter calculated cosmic ray intensity profile more compatible with observations than the modified compound approach, but calculations along the Voyager 2 trajectory (which is inside the HCS region for the period of interest) under these conditions show no significant deviation. As a result this leads to a conclusion that a latitude dependence in the time-dependence of the drift coefficient is necessary in order to compute improved compatibility between Voyager 1 observations and model results. However, one should be careful in implementing such an additional spatial dependence to assure that the drift velocities remain divergence free. Within the limitations of the 2D model such an additional latitudinal dependence leads to additional terms for the drift coefficient at the interface between these two regions. However, since for 2D the HCS is averaged over ϕ, such an additional divergence term may be present at all latitudes enclosed by the HCS.

The second period of interest, i.e. 1992 - 2001, was investigated in Chapter 7 and presented challenges. It was found that the tilt angle increased much sooner than the corresponding decrease in the cosmic ray observations, even taking some propagation time into the outer heliosphere into consideration. The model shows an immediate decrease in the computed cosmic ray intensities not compatible with observations which depicts a delayed reaction to increasing solar activity for this period. It is suggested to use an averaged tilt angle which has a forward time shift effect on the computed cosmic ray intensities in order to compute cosmic ray modulation compatible with observations.

In conclusion, this work investigated certain periods where the approach of Manuel et al. [2014] resulted in incompatibility with cosmic ray intensity observations along the Voyager spacecraft trajectories. A more detailed model, e.g. a full 3-D numerical modulation model may be necessary. Also, the inclusion of GMIRs in the model for solar maximum periods may be necessary to compute step increases and decreases in cosmic ray intensities.

Bibliography

Aschwanden, M., *Physics of the Solar Corona: An Introduction with problems and solutions.* Springer-Praxis Books, second edition, 2005.

Babock, H. W., The topology of the sun's magnetic field and the 22-year cycle, *Astrophys. J.*, *133*, 572–587, 1961.

Balogh, A., and G. Erdos, The heliospheric magnetic field, *Space Sci Rev*, *176*, 177–215, 2013.

Balogh, A., R. G. Marsden, and E. J. Smith, The heliosphere and the Ulysses mission, in *The heliosphere near solar minimum: The Ulysses perspective*, edited by J. Mason, 1–41, Praxis Publishing Ltd, 2001.

Balogh, A., L. J. Lanzerotti, and S. T. Suess, *The heliosphere though the solar activity cycle.* Praxis, 2008.

Behannon, K. W., M. H. Acuna, L. F. Burlaga, R. P. Lepping, N. F. Ness, and F. M. Neubauer, Magnetic field experiment for Voyager 1 and 2, *Space Sci Rev.*, *21*, 235–257, 1977.

Bellan, P. M., *Fundamentals of Plasma Physics.* Cambridge University Press, 2006.

Bieber, J. W., W. H. Matthaeus, C. W. Smith, W. Wanner, M. B. Kallenrode, and G. Wibberenz, Proton and electron mean free paths: The Palmer consensus revisited, *Astrophys. J.*, *420*, 294–306, 1994.

Bieber, J. W., and W. H. Matthaeus, Cosmic ray pitch angle scattering in dynamical magnetic turbulence, *Int. Cosmic Ray Conf.*, *3*, 248–251, 1991.

Bieber, J. W., and W. H. Matthaeus, Perpendicular diffusion and drift at intermediate cosmic ray energies, *Astrophys. J.*, *485*, 655–659, 1997.

Biermann, L., Kometenschweife und solare korpuskularstrahlung, *Zeitschrift fur Astrophysik*, *29*, 274–286, 1951.

Biermann, L., Solar corpuscular radiation and the interplanetary gas, *Correspondence*, *77*, 109–110, 1957.

Borovikov, S. N., N. V. Pogorelov, L. F. Burlaga, and D. Richardson, Plasma near heliosheath: Observations and modeling, *Astrophys. J.*, *728*, 1–5, 2011.

Bray, R. J., and R. E. Loughhead, *Sunspots*, edited by S. B. Lovell, and Z. Kopal, volume 7. Wiley, 1965.

Bridge, H. S., J. W. Belcher, R. J. Butler, A. J. Lazarus, A. M. Mavretic, J. D. Sullivan, G. L. Siscoe, and V. M. Vasyliunas, The plasma experiment of the 1977 Voyager mission, *Space Sci Rev.*, *21*, 259–287, 1977.

Burger, R. A., M. S. Potgieter, and B. Heber, Rigidity dependence of cosmic ray proton latitudinal gradients measured by the Ulysses spacecraft: Implications for the diffusion tensor, *J. Geophys. Res.*, *105*, 27 447–27 455, 2000.

Burger, R. A., T. P. J. Kruger, M. Hitge, and N. E. Engelbrecht, A Fisk-Parker hybrid heliospheric magnetic field with a solar cycle dependence, *Astrophys. J.*, *674*, 511–519, 2008.

Burger, R. A., and M. Hattingh, Steady-state drift-dominated modulation models for galactic cosmic rays, *Astrophys. and Space Sc.*, *230*, 375–382, 1995.

Burger, R. A., and M. Hattingh, Effect of Fisk-type heliospheric magnetic fields on the latitudinal transport of cosmic rays, *Int. Cosmic Ray Conf.*, *9*, 3698–3701, 2001.

Burger, R. A., and M. Hitge, The effect of a Fisk-type heliospheric magnetic field on cosmic rays modulation, *Astrophys. J. Lett.*, *617*, L73–L76, 2004.

Burger, R. A., and M. S. Potgieter, The calculation of neutral sheet drift in two-dimensional cosmic ray modulation models, *Astrophys. J.*, *339*, 501–511, 1989.

Burger, R. A., and D. J. Visser, Reduction of drifts effects due to solar wind turbulence, *Astrophys. J.*, *725*, 1366–1372, 2010.

Burlaga, L. F., MHD processes in the outer heliosphere, *Space Sci Rev*, *39*, 255–316, 1984.

Burlaga, L. F., and K. W. Behannon, Magnetic clouds: Voyager observations between 2 and 4 AU, *Sol. Phys.*, *81*, 181–192, 1982.

Burlaga, L. F., F. B. McDonald, M. L. Goldstein, and A. J. Lazarus, Cosmic ray modulation and turbulent interaction regions near 11 AU, *J. Geophys. Res.*, *90*, 12027–12039, 1985.

Burlaga, L. F., F. B. McDonald, and N. F. Ness, Cosmic ray modulation and the distant heliospheric magnetic field: Voyager 1 and 2 observations from 1986 to 1989, *J. Geophys. Res.*, *98*, 1–11, 1993.

Burlaga, L. F., N. F. Ness, and M. H. Acuna, Magnetic fields in the heliosheath and distant heliosphere: Voyager 1 and 2 observations during 2005 and 2006, *Astrophys. J*, *668*, 1246–1258, 2007.

Burlaga, L. F., and N. F. Ness, Voyager observations of the magnetic field in the distant heliosphere, *Space Sci Rev*, *83*, 105–121, 1998.

Büsching, I., C. Venter, and O. C. deJager, Contributions from nearby pulsars to the local cosmic ray electron spectrum, *Adv. Space Res.*, *42*, 497–503, 2008*a*.

Büsching, I., O. C. deJager, M. S. Potgieter, and C. Venter, A cosmic ray positron anisotropy due to two middle-aged, nearby pulsars?, *Astrophys. J. Lett.*, *678*, L39–L42, 2008*b*.

Cane, H. V., G. Wibberenz, I. G. Richardson, and T. T. VonRosenvinge, Cosmic ray modulation and the solar magnetic field, *Geophys. Res. Lett.*, *26*, 565–568, 1999.

Chenette, D. L., T. F. Conlon, and J. A. Simpson, Burst of relativistic electrons from Jupiter observed in interplanetary space with the time variation of the planetary rotation period, *J. Geophys. Res.*, *79*, 3551–3558, 1974.

Chiuderi, C., and M. Velli, *Basics of Plasma Astrophysics*. Springer, 2014.

Dressing, N., C. M. S. Cohen, R. Gómez-Herrero, B. Heber, A. Klassen, R. A. Leske, G. M. Mason, R. A. Mewaldt, and T. T. vonRosenvinge, Approaching solar maximum 24 with STEREO - multipoint observations of solar energetic particle events, *Braz. J. of Phys.*, *44*, 504–511, 2014.

Dunzlaff, P., R. D. Strauss, and M. S. Potgieter, Solving parker's transport equation with stochastic differential equations on gpus, *Computer Phys. Comm.*, *192*, 156–165, 2015.

Engelbrecht, N. E., 2008. On the heliospheric diffusion tensor and its effects on 26-day recurrent cosmic ray variations. Master's thesis, North-West University, South Africa.

Engelbrecht, N. E., and R. A. Burger, An ab initio model for cosmic ray modulation, *Astrophys. J.*, *772*, 46–57, 2013.

Erdos, G., and A. Balogh, North-south asymmetry of the location of the heliospheric current sheet revisited, *J. Geophys. Res.*, *115*, A01105, 2010.

Fahr, H. J., and K. Scherer, Energetic neutral atom fluxes from the heliosheath varying with the activity phase of the solar cycle, *ASTRA*, *1*, 3–15, 2004.

Ferreira, S. E. S., The heliospheric transport of galactic cosmic rays and jovian electrons, Ph.D. thesis, Potchefstroom University for CHE, South Africa, 2002.

Ferreira, S. E. S., M. S. Potgieter, and R. A. Burger, Comparison of a two- and thre-dimensional drift model, *Int. Cosmic Ray Conf.*, *7*, G77–G80, 1999.

Ferreira, S. E. S., M. S. Potgieter, R. A. Burger, and B. Heber, Modulation effects of anisotropic perpendicular diffusion on cosmic ray electron intensities in the heliosphere, *J. Geophys. Res.*, *105*, 18 305–18 314, 2000.

Ferreira, S. E. S., M. S. Potgieter, and R. A. Burger, Modulation of Jovian and galactic electrons in the heliosphere 1. Latitudinal transport of a few MeV electrons, *J. Geophys. Res.*, *106*, 24 979–24 987, 2001.

Ferreira, S. E. S., M. S. Potgieter, and K. Scherer, Modulation of cosmic-ray electrons in a nonspherical and irregular heliosphere, *Astrophys. J.*, *607*, 1014–1023, 2004.

Ferreira, S. E. S., M. S. Potgieter, and K. Scherer, Transport and acceleration of anomalous cosmic rays in the inner heliosheath, *J. Geophys. Res.*, *112*, 1–11, 2007.

Ferreira, S. E. S., and M. S. Potgieter, Modulation over a 22-year cosmic ray cycle: On the tilt angles of the heliospheric current sheet, *Adv. Space Res.*, *32*, 657–662, 2003.

Ferreira, S. E. S., and M. S. Potgieter, Long-term cosmic-ray modulation in the heliosphere, *Astrophys. J.*, *603*, 744–752, 2004.

Ferreira, S. E. S., and K. Scherer, Modulation of cosmic ray electrons in the outer heliosphere, *Astrophys. J.*, *616*, 1215–1223, 2004.

Ferreira, S. E. S., and K. Scherer, Time evolution of galactic and anomalous cosmic ray spectra in a dynamic heliosphere, *Astrophys. J.*, *642*, 1256–1266, 2006.

Fisk, L. A., Motion of the footpoints of heliospheric magnetic field lines at the Sun: Implications for recurrent energetic particle events at high heliographic latitudes, *J. Geophys. Res.*, *101*, 15547–15553, 1996.

Fisk, L. A., On the global structure of the heliospheric magnetic field, *J. Geophys. Res.*, *106*, 15849–15857, 2001.

Fisk, L. A., B. Kozlovsky, and R. Ramaty, An interpretation of the observed oxygen and nitrogen enhancements in low-energy cosmic rays, *Astrophys. J.*, *190*, L35–L37, 1974.

Fisk, L. A., and G. Gloekler, On whether or not Voyager 1 has crossed the heliopause, *Astrophys. J.*, *789*, 41, 2014.

Fitzpatrick, R., *Plasma Physics: An Introduction*. CRC Press, 2014.

Florinski, V., G. P. Zank, and N. V. Pogorelov, Galactic cosmic ray transport in the global heliosphere, *J. Geophys. Res.*, *108*, 1–16, 2003.

Florinski, V., S. E. S. Ferreira, and N. V. Pogorelov, Galactic cosmic rays in the outer heliosphere: Theory and models, *Space Sci Rev*, *176*, 147–163, 2013.

Frisch, P. C., and D. J. McComas, The interstellar boundary explorer (IBEX): Tracing the interaction between the heliosphere and surrounding interstellar material with energetic neutral atoms, *Space Sci. Rev.*, *176*, 101–113, 2013.

Fujii, Z., and F. B. McDonald, Radial density gradients of galactic cosmic rays from 1973 to 1995, *Int. Cosmic Ray Conf.*, *4*, D772–D775, 1995.

Giacalone, J., J. R. Jokipii, and J. Kóta, Particle drifts in a fluctuating magnetic field, *Int. Cosmic Ray Conf.*, *7*, 37–40, 1999.

Giacalone, J., and J. R. Jokipii, The transport of cosmic rays across a turbulent magnetic field, *Astrophys. J*, *520*, 204–214, 1999.

Gibson, S. E., Global solar wind structure from solar minimum to solar maximum: Sources and evolution, *Space Sci Rev*, *97*, 69–79, 2001.

Gloeckler, G., L. A. Fisk, J. Geiss, M. E. Hill, D. C. Hamilton, R. B. Decker, and S. M. Krimigis, Composition of interstellar neutrals and the origin of anomalous cosmic rays, *Space Sci Rev*, *143*, 163–175, 2009.

Gloekler, G., and L. A. Fisk, More evidence that Voyager 1 is still in the heliosphere, *Astrophys. J. Lett.*, *806*, L27, 2015.

Gurnett, D. A., W. S. Kurth, L. F. Burlaga, and N. F. Ness, In situ observations of interstellar plasma with Voyager 1, *Science*, *341*, 1489–1492, 2013.

Hattingh, M., The modulation of galactic cosmic rays in a three-dimensional heliosphere, Ph.D. thesis, Potchefstroom University for CHE, South Africa, 1998.

Hattingh, M., and R. A. Burger, A new simulated wavy neutral sheet drift model, *Adv. Space Res.*, *16*, 213–216, 1995b.

Hattingh, M., R. A. Burger, M. S. Potgieter, and L. J. Haasbroek, Cosmic ray latitudinal effects predicted by a three-dimensional drift model, *Adv. Space Res.*, *19*, 893–896, 1997.

Heber, B., G. Sarri, G. Wibberens, C. Paizis, P. Ferrando, A. Raviart, A. Posner, R. muller-Mellin, and H. Kunow, The Ulysses fast latitude scans: COSPIN/KET results, *Annales Geophysicae*, *21*, 1275–1288, 2003.

Heber, B., A. Kopp, J. Gieseler, R. Muller-Mellin, H. Fichtner, K. Scherer, M. S. Potgieter, and S. E. S. Ferreira, Modulation of galactic cosmic ray protons and electrons during an unusual solar minimum, *Astrophys. J.*, *699*, 1956–1963, 2009.

Heber, B., and R. G. Marsden, Cosmic ray modulation over the poles at solar maximum: Observations, *Space Sci Rev*, *97*, 309–319, 2001.

Heber, B., and M. S. Potgieter, Galactic and anomalous cosmic rays through the solar cycle: New insights from Ulysses, in *The heliosphere through the solar activity cycle*, 195–249, Springer Berlin Heidelberg, 2008.

Heerikhuisen, J., and N. V. Pogorelov, An estimate of the nearby interstellar magnetic field using neutral atoms, *Astrophys. J.*, *738*, 1–9, 2011.

Hoeksema, J. T. 1992. Large-scale structure of the heliospheric magnetic field: 1976 - 1991. in *Solar Wind Seven Colloquim*, 191–196, .

Hundhausen, A. J., *Coronal Expansion and Solar Wind*. Springer-Verlag Berlin Heidelberg, 1972.

Izmodenov, V. V., and V. B. Baranov, Modern multi-component models of the heliospheric interface, *ISSI Scientific Reports Series*, *5*, 67–136, 2006.

Jokipii, J. R., Cosmic ray propagation. I. Charged particles in a random magnetic field, *Astrophys. J.*, *146*, 480–487, 1966.

Jokipii, J. R., The heliospheric termination shock, *Space Sci. Rev.*, *176*, 115–124, 2013.

Jokipii, J. R., E. H. Levy, and W. B. Hubbard, Effects of particle drift on cosmic ray transport. I. General properties, application to solar modulation, *Astrophys. J.*, *213*, 861–868, 1977.

Jokipii, J. R., C. P. Sonett, and M. S. Giampa, *Cosmic Winds and The Heliosphere*. The University of Arizona Press, 1997.

Jokipii, J. R., and J. Kóta, The polar heliospheric magnetic field, *Geophys. Res. Lett.*, *16*, 1–4, 1989.

Jokipii, J. R., and B. T. Thomas, Effects of drift on the transport of cosmic rays IV. Modulation by a wavy interplanetary current sheet, *Astrophys. J.*, *243*, 1115–1122, 1981.

Kivelson, M. G., and C. T. Russel, *Introduction to Space Physics*. Cambridge University Press, 1995.

Kohlhase, C. E., and P. A. Penzo, Voyager mission description, *Space Sci Rev.*, *21*, 77–101, 1977.

Kóta, J., and J. R. Jokipii, Effects of drifts on the transport of cosmic rays. VI. A three dimensional model including diffusion, *Astrophys. J.*, *265*, 573–581, 1983.

Kóta, J., and J. R. Jokipii, 3-D distribution of cosmic rays in the outer heliosphere, *Int. Cosmic Ray Conf.*, *4*, 680–683, 1995.

Krieger, A. S., A. F. Timothy, and E. C. Roelof, A coronal hole and its identification as the source of a high velocity solar wind stream, *Sol. Phys.*, *29*, 505–525, 1973.

Krimigis, S. M., T. P. Armstrong, W. I. Axford, C. O. Bostrom, C. Y. Fan, G. Gloeckler, and L. J. Lanzerotti, The low energy charged particle (LECP) experiment on the Voyager spacecraft, *Space Sci Rev.*, *21*, 329–354, 1977.

Langner, U. W., Effects of termination shock acceleration on cosmic rays in the heliosphere, Ph.D. thesis, Potchefstroom University for CHE, South Africa, 2004.

Langner, U. W., M. S. Potgieter, H. Fichtner, and T. Borrmann, Effects of different solar wind speed profiles in the heliosheath on the modulation of cosmic ray protons, *Astrophys. J.*, *640*, 1119–1134, 2006.

le Roux, J. A., The solar modulation of galactic cosmic rays as described by a time-dependent drift model, Ph.D. thesis, Potchefstroom University for CHE, South Africa, 1990.

le Roux, J. A., Time-dependent cosmic-ray modulation and global merged interaction regions, *Adv. Space Res.*, *23*, 491–499, 1999.

le Roux, J. A., and H. Fichtner, Global merged interaction regions, the heliospheric termination shock, and time-dependent cosmic ray modulation, *J. Geophys. Res.*, *104*, 1, 1999.

le Roux, J. A., and M. S. Potgieter, Episodic cosmic ray modulation in the heliosphere, *Adv. Space Res.*, *9*, 225–228, 1989.

le Roux, J. A., and M. S. Potgieter, A time-dependent drift model for the long-term modulation of cosmic rays with special reference to asymmetries with respect to the solar minimum of 1987, *Astrophys. J.*, *361*, 275–282, 1990.

le Roux, J. A., and M. S. Potgieter, The simulated features of heliospheric cosmic-ray modulation with a time-dependent drift model. IV. The role of heliospheric neutral sheet deformation, *Astrophys. J.*, *397*, 686–693, 1992.

le Roux, J. A., and M. S. Potgieter, A simulation of complete 11 and 22 year modulation cycles for cosmic rays in the heliosphere using a drift model with global merged interaction regions, *Astrophys. J.*, *442*, 847, 1995.

Lee, M. A., H. J. Fahr, H. Kucharek, E. Moebius, C. Prested, N. A. Schwadron, and P. Wu, Physical processes in the outer heliosphere, *Space Sci. Rev.*, *146*, 275–294, 2009.

Leighton, R. B., A magneto-kinematic model of the solar cycle, *Astrophys. J.*, *156*, 1–26, 1969.

Lockwood, J. A., and W. R. Webber, On the interplanetary cosmic ray latitudinal gradient, *J. Geophys. Res.*, *77*, 8221–8230, 1992.

Magidimisha, E., 2011. A study of the time-dependent modulation of cosmic rays in the inner heliosphere. Master's thesis, North-West University, South Africa.

Manuel, R., Time-dependent modulation of cosmic rays in the outer heliosphere, Ph.D. thesis, North-West University, South Africa, 2012.

Manuel, R., S. E. S. Ferreira, and M. S. Potgieter, Cosmic ray modulation along Voyager 1 and 2 trajectories, *Int. Cosmic Ray Conf.*, *11*, 18–21, 2011*a*.

Manuel, R., S. E. S. Ferreira, M. S. Potgieter, R. D. Strauss, and N. E. Engelbrecht, Time-dependent cosmic ray modulation, *Adv. Space Res.*, *47*, 1529–1537, 2011*b*.

Manuel, R., S. E. S. Ferreira, and M. S. Potgieter, Time-dependent modulation of cosmic rays in the heliosphere, *Solar Phys*, *289*, 2207–2231, 2014.

Marsch, E., H. J. Fahr, and K. Scherer, *The outer heliosphere: The next frontiers*. Elsevier, 2001.

Matthaeus, W. H., G. Qin, J. W. Bieber, and G. P. Zank, Nonlinear collisionless perpendicular diffusion of charged particles, *Astrophys. J.*, *590*, L53–L56, 2003.

Mavromichalaki, H., B. Petropoulos, C. Plainaki, O. Dionatos, and I. Zouganelis, Coronal index as a solar activity index applied to space weather, *Adv. Space Res.*, *35*, 410–415, 2005.

McComas, D. J., D. Alexashov, M. Bzowski, H. Fahr, J. Heerikhuisen, V. Izmodenov, M. A. Lee, E. Mobius, N. V. Pogorelov, N. A. Schwadron, and G. P. Zank, The heliosphere's interstellar interaction: No bow shock, *Science*, *336*, 1291–1293, 2012.

McDonald, F. B., and L. F. Burlaga, Global merged interaction regions in the outer heliosphere, in *Cosmic Winds and The Heliosphere*, edited by J. R. Jokipii, C. P. Sonett,, and M. S. Giampapa, 389, The University of Arizona Press, 1997.

Minnie, J., J. W. Bieber, and W. H. Matthaeus, Suppression of particle drifts by turbulence, *Astrophys. J.*, *670*, 1149–1158, 2007.

Minnie, J., W. H. Matthaeus, J. W. Bieber, D. Ruffolo, and R. A. Burger, When do particles follow field lines, *J. Geophys. Res.*, *114*, 1–7, 2009.

Moeketsi, D. M., 2004. Modelling of galactic and Jovian electrons in the heliosphere. Master's thesis, North-West University, South Africa.

Moeketsi, D. M., M. S. Potgieter, S. E. S. Ferreira, B. Heber, H. Fichtner, and V. K. Henize, The heliospheric modulation of 3 - 10 MeV electrons: Modeling of changes in the solar wind speed in relation to perpendicular polar diffusion, *Adv. Space Res.*, *35*, 597–604, 2005.

Moloto, K. D., 2015. The effect of the heliospheric current sheet on cosmic ray modulation. Master's thesis, North-West University, South Africa.

Moraal, H., Proton modulation near solar minimum periods in consecutive solar cycles, *Int. Cosmic Ray Conf.*, *6*, 140–143, 1990.

Muller, H. R., P. C. Frisch, B. D. Fields, and G. P. Zank, The heliosphere in time, *Space Sci Rev*, *143*, 415–425, 2009.

Ndiitwani, D. C., S. E. S. Ferreira, M. S. Potgieter, and B. Heber, Modelling cosmic ray intensities along the Ulysses trajectory, *Ann. Geophys*, *23*, 1061–1070, 2005.

Ness, N. F., Heliospheric magnetic field and termination shock crossing: Voyager 1, *ISSI Scientific Reports Series*, *5*, 183–202, 2006.

Ngobeni, M. D., Modeling of galactic cosmic rays in the heliosphere, Ph.D. thesis, North-West University, South Africa, 2015.

Ngobeni, M. D., and M. S. Potgieter, Modelling the effects of scattering parameters on particle-drift in the solar modulation of galactic cosmic rays, *Adv. Space Res.*, *56*, 1525–1537, 2015.

Opher, M., E. C. Stone, P. C. Liewer, and T. Gombosi, Global asymmetry of the heliosphere, *AIP Conf. Proc.*, *858*, 1–7, 2006.

Palmer, I. D., Transport coefficients of low-energy cosmic rays in the interplanetary space, *Reviews of Geophys. and Space Phys.*, *20*, 335–351, 1982.

Parker, E. N., Dynamics of the interplanetary gas and magnetic fields, *Astrophys. J.*, *128*, 664–676, 1958.

Parker, E. N., The hydrodynamic theory of solar corpuscular radiation and stellar winds, *Astrophys. J.*, *132*, 821–866, 1960.

Parker, E. N., The passage of energetic charged particles through interplanetary space, *Planet. Space Sci.*, *13*, 9–49, 1965.

Pauls, H. L., and G. P. Zank, Modelling the heliosphere, *Space Sci Rev*, *78*, 95–106, 1996.

Perko, J. S., and L. A. Fisk, Solar modulation of galactic cosmic rays V. Time-dependent modulation, *J. Geophys. Res.*, *88*, 9033–9036, 1983.

Pogorelov, N. V., G. P. Zank, and T. Ogino, MHD modeling of the outer heliosphere: Achievements and challenges, *Adv. Space Res.*, *41*, 306–317, 2008.

Pogorelov, N. V., J. Heerikhuisen, G. P. Zank, J. J. Mitchell, and I. H. Cairns, Heliospheric asymmetries due to the action of the interstellar magnetic field, *Adv. Space Res.*, *44*, 1337–1344, 2009.

Pogorelov, N. V., S. T. Suess, S. N. Borovikov, R. W. Ebert, D. J. McComas, and G. P. Zank, Three-dimensional features of the outer heliosphere due to coupling between the interstellar and interplanetary magnetic fields. IV. Solar cycle model based on Ulysses observations, *Astrophys. J.*, *772*, 1–17, 2013.

Pogorelov, N. V., S. N. Borovikov, J. Heerikhuisen, T. K. Kim, and G. P. Zank, Time-dependent processes in the sheath between the heliospheric termination shock and the heliopause, *ASP Conference Series*, *488*, 167–176, 2014.

Potgieter, M. S., Heliospheric modulation of galactic electrons: Consequences of new calculations for the mean free path of electrons between 1 MeV and ∼10 GeV, *J. Geophys. Res.*, *101*, 24.411–24.422, 1996.

Potgieter, M. S., Cosmic rays in the inner heliosphere: Insights from observations, theory and models, *Space Sci Rev*, *176*, 165–176, 2013*a*.

Potgieter, M. S., Solar modulation of cosmic rays, *Living Rev. Solar Phys.*, *10*, 5–66, 2013*b*.

Potgieter, M. S., Very local interstellar spectra for galactic electrons, protons and helium, *Braz. J. Phys.*, *44*, 581–588, 2014.

Potgieter, M. S., L. J. Haasbroek, P. Ferrando, and B. Heber, The modelling of the latitude depende of cosmic ray protons and electrons in the inner heliosphere, *Adv. Space Res.*, *19*, 917–920, 1997.

Potgieter, M. S., E. E. Vos, M. Boezio, N. DeSimone, V. DiFelice, and V. Formanto, Modulation of galactic protons in the heliosphere during the unsusal solar minimum of 2006 to 2009, *Solar Physics*, *289*, 391–406, 2014.

Potgieter, M. S., and S. E. S. Ferreira, The importance of perpendicular diffusion in the heliospheric modulation of cosmic ray electrons, *Adv. Space Res.*, *23*, 463–466, 1999.

Potgieter, M. S., and L. J. Haasbroek, The simulation of base-line cosmic ray modulation for the Ulysses trajectory, *Int. Cosmic Ray Conf.*, *3*, 457–460, 1993.

Potgieter, M. S., and J. A. leRoux, The simulated features of heliospheric cosmic ray modulation with a time-dependent drift model. I. General effects of the changing neutral sheet over the period 1985 - 1990, *Astrophys. J.*, *386*, 336–346, 1992.

Potgieter, M. S., and H. Moraal, A drift model for the modulation of galactic cosmic rays, *Astrophys. J.*, *294*, 425–440, 1985.

Potgieter, M. S., and H. Moraal, Acceleration of cosmic rays in the solar wind termination shock. I - A steady state technique in a spherically symmetric model, *Astrophys. J.*, *330*, 445–455, 1988.

Potgieter, M. S., and R. R. Nndanganeni, The solar modulation of electrons in the heliosphere, *Astrophys Space Sci.*, *345*, 33–40, 2013.

Prinsloo, P. L., 2016. Acceleration of cosmic rays in the outer heliosphere. Master's thesis, North-West University, South Africa.

Qin, G., W. H. Matthaeus, and J. W. Bieber, Subdiffusive transport of charged particles perpendicular to the large scale magnetic field, *J. Geophys. Res.*, *29*, 1–4, 2002.

Raath, J. L., 2015. A comparative study of cosmic ray modulation models. Master's thesis, North-West University, South Africa.

Raath, J. L., R. D. Strauss, and M. S. Potgieter, New insights from modeling the neutral heliospheric current sheet, *Astrophys Space Sci.*, *360*, 1–13, 2015.

Richardson, J. D., Variability of plasma in the heliosheath, *Astrophys. J.*, *740*, 1–5, 2011.

Richardson, J. D., and L. F. Burlaga, The solar wind in the outer heliosphere and heliosheath, *Space Sci. Rev.*, *176*, 217–235, 2013.

Richardson, J. D., J. C. Kasper, C. Wang, J. W. Belcher, and A. J. Lazarus, Cool heliosheath plasma and deceleration of the upstream solar wind at the termination shock, *Nature*, *454*, 63–66, 2008.

Richardson, J. D., and E. C. Stone, The solar wind in the outer heliosphere, *Space Sci Rev*, *143*, 7–20, 2009.

Riley, P., J. A. Linker, and Z. Mikic, Modeling the heliospheric current sheet: Solar cycle variations, *J. Geophys. Res.*, *107*, 1–6, 2002.

le Roux, J. A., M. S. Potgieter, and V. S. Ptuskin, A transport model for the diffusive shock acceleration and modulation of anomalous cosmic rays in the heliosphere, *J. Geophys. Res.*, *101*, 4791–4803, 1996.

Rybansky, M., V. Rusin, and M. Minarovjech, Coronal index of solar activity, *Space Sci Rev*, *95*, 227–234, 2001.

Scarf, F. L., and D. A. Gurnett, A plasma wave investigation for the Voyager mission, *Space Sci Rev.*, *21*, 289–308, 1977.

Schatten, K. H., J. M. Wilcox, and N. F. Ness, A model of interplanetary and coronal magnetic fields, *Sol. Phys.*, *6*, 442–455, 1969.

Scherer, K., H. Fichtner, R. D. Strauss, S. E. S. Ferreira, M. S. Potgieter, and H. J. Fahr, On cosmic ray modulation beyond the heliopause: Where is the modulation boundary?, *Astrophys. J.*, *735*, 1–5, 2011.

Scherer, K., and H. J. Fahr, Breathing of heliospheric structures triggered by the solar-cycle activity, *Annales Geophysicae*, *21*, 1303–1313, 2003*a*.

Scherer, K., and H. J. Fahr, Solar cycle induced variations of the outer heliospheric structures, *Geophys. Res. Lett.*, *30*, 2003*b*.

Schroder, F. G., *Instruments and methods for the radio detection of high energy cosmic rays*. Springer Theses, 2012.

Shalchi, A., *Nonlinear cosmic ray diffusion theories*. Springer-Verlag Berlin Heidelberg, 2009.

Shalchi, A., J. W. Bieber, and W. H. Mathaeus, Analytical forms of the perpendicular diffusion coefficients in magnetostatic turbulence, *Astrophys. J.*, *604*, 675–686, 2004.

Shibata, K., and T. Magara, Solar flares: Magnetohydrodynamic processes, *Living Rev. Solar Phys*, *8*, 5–8, 2011.

Simpson, J. A., D. Hamilton, G. Lentz, R. B. McKibben, A. Mogro-Campero, M. Perkins, K. R. Pyle, A. J. Tuzzolino, and J. J. O'Gallagher, Protons and electrons in Jupiter's magnetic field: Results from the University of Chicago Experiment on Pioneer 10, *Science*, *183*, 306–309, 1974.

Smith, C. W., and J. W. Bieber, Solar cycle variation of the interplanetary magnetic field spiral, *Astrophys. J.*, *370*, 435–441, 1991.

Smith, E. J., The heliospheric current sheet, *J. Geophys. Res.*, *106*, 15,819–15,831, 2001.

Smith, E. J., A. Balogh, G. Erdos, and R. J. Forsyth, Results of the Ulysses fast latitude scan: Magnetic field observations, *Geophys. Res. Lett.*, *22*, 3325–3328, 1995.

Smith, E. J., J. R. Jokipii, J. Kóta, R. P. Lepping, and A. Szabo, Evidence of a north-south asymmetry in the heliosphere associated with a southward displacement of the heliospheric current sheet, *Astrophys. J.*, *533*, 1084–1089, 2000.

Snyman, J. L., 2007. Modelling of the heliosphere and cosmic ray transport. Master's thesis, North-West University, South Africa.

Sternal, O., R. A. Burger, P. Dunzlaff, S. E. S. Ferreira, H. Fichtner, B. Heber, A. Kopp, K. Scherer, and M. S. Potgieter, Time-dependent propagation of 7 MeV electron in a Fisk-Parker Hybrid HMF, *31st Int. Cosmic Ray Conf.*, *31*, 1–4, 2009.

Stix, M., *The Sun: An Introduction*. Springer, second edition, 2004.

Stone, E. C., R. E. Vogt, F. B. McDonald, B. J. Teegarden, J. H. Trainor, J. R. Jokipii, and W. R. Webber, Cosmic ray investigation for the Voyager missions: Energetic particle studies in the outer heliosphere - and beyond, *Space Sci Rev.*, *21*, 355–376, 1977.

Stone, E. C., A. C. Cummings, F. B. McDonald, B. C. Heikkila, N. Lal, and W. R. Webber, Voyager 1 explores the termination shock region and the heliosheath beyond, *Science*, *309*, 2017–2020, 2005.

Stone, E. C., A. C. Cummings, F. B. McDonald, B. C. Heikkila, N. Lal, and W. R. Webber, An asymmetric solar wind termination shock, *Nature*, *454*, 71–74, 2008.

Stone, E. C., A. C. Cummings, F. B. McDonald, B. C. Heikkila, N. Lal, and W. R. Webber, Voyager 1 observes low-energy galactic cosmic rays in a region depleted of heliospheric ions, *Science*, *341*, 150–153, 2013.

Strauss, R. D., M. S. Potgieter, S. E. S. Ferreira, and M. E. Hill, Modelling anomalous cosmic ray oxygen in the heliosheath, *Astron. Astrophys.*, *522*, 1–8, 2010.

Strauss, R. D., M. S. Potgieter, I. Büsching, and A. Kopp, Modelling heliospheric current sheet drift in stochastic cosmic ray transport models, *Astrophys Space Sci.*, *339*, 223–236, 2012.

Strauss, R. D., M. S. Potgieter, and S. E. S. Ferreira, Modelling and observing jovian electron propagation times in the inner heliosphere, *Adv. Space Res.*, *51*, 339–349, 2013.

Strauss, R. D., and M. S. Potgieter, Where does the heliospheric modulation of galactic cosmic rays start?, *Adv. Space Res.*, *53*, 1015–1023, 2014.

Tautz, R. C., and A. Shalchi, Drift coefficient of charged particles in turbulent magnetic fields, *Astrophys. J.*, *125*, 744–751, 2012.

Teufel, A., and R. Schlickeiser, Analytical calculation of the parallel mean free path of heliospheric cosmic rays. I. Dynamical magnetic slab turbulence and random sweeping slab turbulence, *Astrophys. J.*, *393*, 703–715, 2002.

Teufel, A., and R. Schlickeiser, Analytical calculation of the parallel mean free path of heliospheric cosmic rays. II. Dynamical magnetic slab turbulence and random sweeping slab turbulence with finite wave power at small wavenumbers, *Astrophys. J.*, *397*, 15–25, 2003.

Usoskin, I. G., A history of solar activity over millenia, *Living Rev. Solar Phys*, *5*, 1–88, 2008.

Vos, E. E., 2012. Cosmic ray modulation processes in the heliosphere. Master's thesis, North-West University, South Africa.

Vos, E. E., Modelling charge-sign dependent modulation of cosmic rays in the heliosphere, Ph.D. thesis, North-West University, South Africa, 2016.

Wang, Y. M., and N. R. Sheeley, Solar implications of Ulysses interplanetary field measurements, *Astrophys. J.*, *447*, L143–L146, 1995.

Webber, W. R., and D. S. Intriligator, Voyager 1 and 2 in a shrunken and squashed heliosphere, *J. Geophys. Res.*, *116*, 1–8, 2011.

Webber, W. R., and F. B. McDonald, Recent Voyager 1 data indicate that on 25 August 2012 at a distance of 121.7 AU from the Sun, sudden and unprecedented intensity changes were observed in anomalous and galactic cosmic rays, *Geophys. Res. Lett.*, *40*, 1665–1668, 2013.

Weiss, N. O., and S. M. Tobias, Physical causes of solar activity, *Space Sci Rev*, *94*, 99–112, 2000.

Weymann, R., Coronal evaporation as a possible mechanism for mass loss in red giants, *Astrophys. J.*, *132*, 380, 1960.

Wibberenz, G., I. G. Richardson, and H. V. Cane, A simple concept for modelling cosmic ray modulation in the inner heliosphere during solar cycles 20-23, *J. Geophys. Res.*, *107*, 1–15, 2002.

Wibig, T., and A. W. Wolfendale, The spectrum of galactic cosmic rays of the highest energies, *Int. Cosmic Ray Conf.*, *21*, 1–4, 2009.

Williams, T., 1990. The influence of the wavy heliospheric neutral current sheet on the modulation of cosmic rays (in Afrikaans). Master's thesis, Potchefstroom University for CHE, South Africa.

Zank, G. P., H. L. Pauls, L. L. Williams, and D. T. Hall, Interaction of the solar wind with the local interstellar medium: A multifluid approach., *J. Geophys. Res.*, *101*, 21 639–21 655, 1996.

Zank, G. P., J. Heerikhuisen, B. E. Wood, N. V. Pogorelov, E. Zirnstein, and D. J. McComas, Heliospheric structure: The bow wave and the hydrogen wall, *Astrophys. J.*, *763*, 1–13, 2013.